Ministério da
Ciência, Tecnologia
e Inovação

GOVERNO FEDERAL
BRASIL
PAÍS RICO É PAÍS SEM POBREZA

sid.inpe.br/mtc-m19/2011/09.22.18.02.43-TDI

EDGE STRUCTURES AND TURBULENCE IN SPACE PLASMAS

Pablo Rubén Muñoz Gutberlet

Doctorate Thesis at Post Graduation Course applied in Space Geophysics, advised by Drs. Abraham Chian Long-Chian, Erico Luiz Rempel, and Joaquim José Barroso de Castro, approved in September 29, 2011.

URL of the original document:
<http://urlib.net/8JMKD3MGP7W/3AFL8A3>

INPE
São José dos Campos
2011

PUBLISHED BY:

Instituto Nacional de Pesquisas Espaciais - INPE
Gabinete do Diretor (GB)
Serviço de Informação e Documentação (SID)
Caixa Postal 515 - CEP 12.245-970
São José dos Campos - SP - Brasil
Tel.:(012) 3208-6923/6921
Fax: (012) 3208-6919
E-mail: pubtc@sid.inpe.br

BOARD OF PUBLISHING AND PRESERVATION OF INPE INTELLECTUAL PRODUCTION (RE/DIR-204):
Chairperson:
Dr. Gerald Jean Francis Banon - Coordenação Observação da Terra (OBT)
Members:
Dr^{a} Inez Staciarini Batista - Coordenação Ciências Espaciais e Atmosféricas (CEA)
Dr^{a} Maria do Carmo de Andrade Nono - Conselho de Pós-Graduação
Dr^{a} Regina Célia dos Santos Alvalá - Centro de Ciência do Sistema Terrestre (CST)
Marciana Leite Ribeiro - Serviço de Informação e Documentação (SID)
Dr. Ralf Gielow - Centro de Previsão de Tempo e Estudos Climáticos (CPT)
Dr. Wilson Yamaguti - Coordenação Engenharia e Tecnologia Espacial (ETE)
Dr. Horácio Hideki Yanasse - Centro de Tecnologias Especiais (CTE)
DIGITAL LIBRARY:
Dr. Gerald Jean Francis Banon - Coordenação de Observação da Terra (OBT)
Marciana Leite Ribeiro - Serviço de Informação e Documentação (SID)
Deicy Farabello - Centro de Previsão de Tempo e Estudos Climáticos (CPT)
DOCUMENT REVIEW:
Marciana Leite Ribeiro - Serviço de Informação e Documentação (SID)
Yolanda Ribeiro da Silva Souza - Serviço de Informação e Documentação (SID)
ELECTRONIC EDITING:
Vivéca Sant´Ana Lemos - Serviço de Informação e Documentação (SID)

sid.inpe.br/mtc-m19/2011/09.22.18.02.43-TDI

EDGE STRUCTURES AND TURBULENCE IN SPACE PLASMAS

Pablo Rubén Muñoz Gutberlet

Doctorate Thesis at Post Graduation Course applied in Space Geophysics, advised by Drs. Abraham Chian Long-Chian, Erico Luiz Rempel, and Joaquim José Barroso de Castro, approved in September 29, 2011.

URL of the original document:
<http://urlib.net/8JMKD3MGP7W/3AFL8A3>

INPE
São José dos Campos
2011

Cataloging in Publication Data

M926e

Muñoz Gutberlet, Pablo Rubén.

Edge structures and turbulence in space plasmas / Pablo Rubén Muñoz Gutberlet. – São José dos Campos : INPE, 2011.

xxiv + 108 p. ; (sid.inpe.br/mtc-m19/2011/09.22.18.02.43-TDI)

Doctorate Thesis (Doctorate Thesis in Space Geophysics) – Instituto Nacional de Pesquisas Espaciais, São José dos Campos, 2011.

Advisers : Drs. Abraham Chian Long-Chian, Érico Luiz Rempel, and Joaquim José Barroso de Castro.

1. Turbulence. 2. Coherent structures. 3. Nonlinear dynamical systems. 4. Edge of chaos. I.Título.

CDU 52-466

Copyright © 2011 do MCT/INPE. Nenhuma parte desta publicação pode ser reproduzida, armazenada em um sistema de recuperação, ou transmitida sob qualquer forma ou por qualquer meio, eletrônico, mecânico, fotográfico, reprográfico, de microfilmagem ou outros, sem a permissão escrita do INPE, com exceção de qualquer material fornecido especificamente com o propósito de ser entrado e executado num sistema computacional, para o uso exclusivo do leitor da obra.

Copyright © 2011 by MCT/INPE. No part of this publication may be reproduced, stored in a retrieval system, or transmitted in any form or by any means, electronic, mechanical, photocopying, recording, microfilming, or otherwise, without written permission from INPE, with the exception of any material supplied specifically for the purpose of being entered and executed on a computer system, for exclusive use of the reader of the work.

Aprovado (a) pela Banca Examinadora em cumprimento ao requisito exigido para obtenção do Título de Doutor(a) em

Geofísica Espacial

Dr. Odim Mendes Júnior

Odim Mendes Júnior

Presidente / INPE / SJCampos - SP

Dr. Polinaya Muralikrishna

Vice-Presidente / INPE / São José dos Campos - SP

Dr. Abraham Chian Long-Chian

Abraham Chian

Orientador(a) / Observ. Paris / Meudon - FR

Dr. Joaquim José Barroso de Castro

J.J. Barroso

Orientador(a) / INPE / SJCampos - SP

Dr. Erico Luiz Rempel

Orientador(a) / ITA / SJCampos - SP

Dr. Giovani Lopes Vasconcelos

Giovani Vasconcelos

Convidado(a) / UFPe / Pernambuco - PE

Dr. Antonio Endler

Antonio Endler

Convidado(a) / UFRGS / Porto Alegre - RS

Este trabalho foi aprovado por:

☐ maioria simples

☒ unanimidade

Aluno (a): Pablo Rubén Muñoz Gutberlet

São José dos Campos, 29 de setembro de 2011

To my wife Daniela and my daughter Amparo

ACKNOWLEDGEMENTS

In first place, I would like to thank my wife Daniela, for her inconditional support and love all these years, and my daughter Amparo, who gave me the strength to climb the last steps to complete this work.

I would like to thank my family in Chile: my mother Berta and my brother Carlitos, I always think of you. Also, to my father-in-law Jaime and my-mother-in-law Malú, for supporting my work.

I am very grateful to my advisors Dr. Abraham Chian, Dr. Erico Rempel and Dr. Joaquim Barroso, for their valuable advice, patience and friendship.

To Coordenação de Aperfeiçoamento de Pessoal de Nível Superior (CAPES) for their financial support.

To Dr. Alejandro Valdivia and Dr. Victor Muñoz, who made it possible for me to come to Brazil.

To Dr. Rodrigo Miranda and Dr. Benjamin Toledo for their invaluable help, stimulating scientific conversations and friendship.

To all people at the Space Geophysics Division (DGE) at INPE and in general to all brazilian people that made me feel this country as my home.

To my friends Loreto, Daniela, Roberta, Julio, Flora, Ari, Fernanda, Marcelo, Evelyn and Douglas. Thanks for your friendship. To Gabriel Moiano, who gave us support my wife and me in the most varied difficulties. To Marcio Valeriano, and the inspiring jam sessions. Also to Marcio's wife Silvana and the “galera”.

ABSTRACT

We investigate a number of nonlinear physical problems relevant for the space environment, using both observational data and a dynamical systems approach. First, the relation between current sheets, turbulence and magnetic reconnections at the leading edge of an interplanetary coronal mass ejection (ICME) detected by four Cluster spacecraft on 21 January 2005 is studied. We report the observational evidence of two magnetically reconnected current sheets in the vicinity of a front magnetic cloud boundary layer, in connection with the enhancement of intermittent turbulence. In addition, we carry out theoretical studies of edge of chaos and coherent structures in fluids and plasmas, including solar dynamo, Pierce diode (double layers), and drift waves in plasmas (long waves in shallow waters). All theoretical models studied in this thesis share a common feature, namely, for a given physical parameter, all initial conditions converge asymptotically to an attractor, with some of them showing a chaotic transient behavior before converging to an attractor. These chaotic transients are due to the presence of an ubiquitous unstable, non-attracting, coherent structure known as chaotic saddle. Based on the concept of lifetime function, we distinguish the region of phase space having shorter transient lifetimes whose trajectories converge quickly to the attractor, from the region with longer lifetimes whose trajectories traverse first in the vicinity of a chaotic saddle before converging to an attractor. The boundary that separates the two regions is called the edge of chaos, which corresponds to the stable manifold of an unstable saddle coherent structure (the edge state) determined by the bisection method. We show the importance of the edge states in laminar–turbulent transitions in fluids and plasmas and conclude that the edge of chaos is an universal phenomenon in nonlinear systems with chaotic transients, and may be crucial to understand the phenomenon of turbulence in nature.

ESTRUTURAS DE FRONTEIRA E TURBULÊNCIA EM PLASMAS ESPACIAIS

RESUMO

Neste trabalho foi investigada uma série de problemas físicos não–lineares relevantes para o ambiente espacial, baseando–se tanto em dados observacionais quanto numa abordagem de sistemas dinâmicos. Primeiro, foi estudada a relação entre as lâminas de corrente, a turbulência e a reconexão magnética na borda frontal de uma ejeção de massa coronal interplanetária detectada pelos quatro satélites Cluster, no dia 21 de Janeiro de 2005. Foi reportada a evidência observacional de duas lâminas de corrente reconectadas na vizinhança da camada limite frontal de uma nuvem magnética, as quais tem relação direta com o aumento da turbulência intermitente. Além disso, foram feitos estudos teóricos da fronteira de caos e as estruturas coerentes em fluídos e plasmas, incluindo o dínamo solar, o díodo de Pierce e um modelo de ondas de deriva não–linear em plasmas (ondas longas em águas razas). Todos os modelos estudados neste trabalho compartilham uma mesma característica: para um certo parâmetro físico dado, todas as condições iniciais convergem assintóticamente para um atrator, com algumas delas apresentando transientes caóticos antes de convergir para o atrator. Estes transientes caóticos devem–se à presença de uma estrutura coerente não–atrativa, chamada de sela caótica. Baseando–se no conceito da função de tempo de vida, é possível distinguir as regiões do espaço de fase com menores tempos de vida, cujas trajetórias convergem rapidamente para o atrator, daquelas com maiores tempos de vida, cujas trajetórias percorrem a vizinhança da sela caótica antes de converger para o atrator. A fronteira que separa as duas regiões é chamada de fronteira de caos, a qual corresponde à variedade estável de uma estrutura coerente de sela, o estado de fronteira, determinado pelo método de bisecção. Foi demonstrada a importância do estado de fronteira nas transições de fluxo laminar para turbulência em fluídos e plasmas. Concluiu–se que a fronteira de caos é um fenômeno universal em sistemas não–lineares que apresentam transientes caóticos, e pode ser crucial para compreender a turbulência na natureza.

LIST OF FIGURES

Pág.

1.1 Power spectrum density of turbulence with the characteristic power law within the inertial subrange, between the energy injection scale k_{in} and the energy dissipation scale k_{d}. 2

2.1 Schematic diagram of an ICME ejected from the Sun. 6
2.2 Overview of the ICME event of 21 January 2005 as measured by Cluster–1. From top to bottom: modulus of magnetic field $|\mathbf{B}|$ (nT); the three components of the vector magnetic field B_x, B_y and B_z in the GSE coordinates; angle Φ_B (degrees) of the magnetic field relative to the x-axis in the ecliptic plane; angle Θ_B of the magnetic field out of the ecliptic; the speed of the ions $|\mathbf{V}|$ (km/s); ion number density N_i (cm^{-3}); ion temperature T_i (°K), and ion plasma beta β. The arrival shock (SA) and the leading boundary of the ejecta (SB) are marked by dashed lines. . . . 7
2.3 Li (2008) method to locate current sheets within a magnetic field time series. 9
2.4 Upper panel: $F(\theta, \tau)$ as function of θ. For large–scales ($\tau = 30, 60, 120, 240$ sec) $F(\theta, \tau)$ are nicely ordered with respect to θ. In addition, when $60° < \theta < 120°$ the curves are approximately parallel to each other. Lower panel: $F(\theta, \tau)$ as function of τ for different values of θ. A linear behavior is clearly seen for different critical angles, in agreement with equation (2.3). 10
2.5 Current sheets of size $\tau = 120$ seconds detected by the single-spacecraft method applied over the time series of $\mathbf{B}$ (black line), using four critical angles θ. The position of the currents sheets are marked by red dots. The number of CS detected decrease as θ is increased, as expected from $F(\theta, \tau)$ in the upper panel of Fig. 2.4. Three CS, including both at the leading edge of the ejecta are detected in all cases. 11
2.6 Current sheets detected with the single–spacecraft method, fixing the critical angle $\theta = 60°$ using four time scales τ. The number of points considered as being part of a current sheet (red dots) increases as τ is increased, as expected from $F(\theta, \tau)$ in the lower panel of Fig. 2.4. 12

2.7 (a) Modulus of the magnetic field $|\mathbf{B}|$ in the time interval containing the two current sheets SB1 and SB2 associated with the leading edge (SB) of the ICME ejecta. (b) Power spectral density, PSD (nT^2 Hz^{-1}), of $|\mathbf{B}|$ for the time interval of (a); straight lines indicate the inertial and dissipative subranges. The spectral indices are calculated by a linear regression of the log–log PSD data. 13

2.8 Scale dependence for three different timescales (τ=2 s, 20 s and 200 s) of Fig. 2.7(b). (a) The normalized magnetic–field two–point differences ΔB. (b) The probability density function PDF of ΔB, superposed by a Gaussian PDF (orange line). 14

2.9 Upper panel: structure functions vs. timescale τ for $p = 1$ (black), $p = 2$ (red), $p = 3$ (green), $p = 4$ (blue), $p = 5$ (yellow) and $p = 6$ (brown). Lower panel: structure functions after applying the Extended Self–Similarity technique. Horizontal arrow represents the previous inertial subrange. 16

2.10 Scaling exponent ζ of the pth–order structure function for observed values (red diamonds), superposed by the K41 self–similar scaling (black dashed line), and the multifractal prediction of the She–Leveque MHD model (blue curve). 17

2.11 Idealized two–dimensional reconnection exhaust region bounded by a bifurcated current sheet. The field line kinks associated with magnetic reconnection propagate as Alfvén waves along the field lines accelarating plasma away from the reconnection site (adapted from Gosling et al. (2005)). 18

2.12 Detection of magnetic reconnections at the leading edge of ICME associated with the current sheets SB1 and SB2 (magenta). $|\mathbf{B}|$ (nT) is the modulus of magnetic field (enlargement of Fig. 2.7(a); $|\mathbf{V}|$ (km s^{-1}) is the modulus of the observed plasma velocity (black) and the plasma velocity (orange) predicted by the magnetic reconnection theory of Sonnerup et al. (1981); $|\mathbf{J}|$ (nA m^{-2}) is the modulus of current density computed by the multi-spacecraft curlometer technique of Dunlop et al. (2002). 20

2.13 B_L (red), B_M (green) and B_N (blue) are the components of $\mathbf{B}$ measured by Cluster–1 in the LMN coordinates; V_L (red), V_M (green) and V_N (blue) are the components of $\mathbf{V}$. This figure shows observational evidence of bifurcated current sheets SB1 and SB2, with a plateau at B_L in the middle of each bifurcated current sheet, and counter–propagating Alfvén waves at two edges of SB1 and SB2. 21

2.14 Direct evidence of a bifurcated current sheet SB1 measured by Cluster-3. (a) Two–step temporal variation of B_L with a plateau in the middle of the current sheet. (b) J_M calculated from B_L showing double peaks at both edges of the current sheet. 22

3.1 Typical solution of the mean–field dynamo model of Eqs. (3.14)–(3.16) for $D = 205$, $\nu = 0.5$ and $\sigma = 0$. Upper panel: Temporal evolution of the averaged poloidal magnetic energy. Lower panel: Saptio–temporal pattern of the poloidal magnetic field. The vertical axis represents the latitude, with $\theta = \pi/2$ being the equator. 31

3.2 Bifurcation diagram of Eqs. (3.14)–(3.16) using as control parameter the dynamo number D. PB denotes the pitchfork bifurcation where a periodic attractor (black) loses its stability and two new periodic attractors (blue and red) arises. These two attractors become chaotic through a cascade of period doubling bifurcations. MC denotes the merging crisis, when the attractors merge one to each other to form a single chaotic attractor. PW indicates a periodic windows embedded in the chaotic region. 33

3.3 (a) Periodic window of the bifurcation diagram, where both the attractor (black) and the surrounding chaotic saddle (green) are plotted. (b) The two largest Lyapunov exponents of the attractor (black and red). (c) Enlargement of one of the thirteen branches of (a). 34

3.4 The characterization of IC due to a chaotic attractor–chaotic saddle collision at the end of the periodic window. (a) The BCA (black), the SCS (green), one Poincaré point of the period–13 mediating UPO (cross) and its stable manifold (dashed line). (b) Stable (light blue) and unstable (brown) manifolds of the SCS. 35

3.5 (a) A Poincaré map time series of the banded chaotic attractor (BCA) at $D = 205.8525 > D_{\mathrm{IC}}$, before the interior crisis. (b) The time series of crisis-induced intermittency corresponding to the post-crisis chaotic attractor. (c) Time series of the random attractor for a small noise amplitude $\sigma = 10^{-3.5}$. The trajectory traverses the vicinity of BCA. (d) For a larger value of the noise amplitude, $\sigma = 10^{-3}$, the time series of the random chaotic attractor shows evidence of noise–induced intermittency. 36

3.6 Two dimensional Poincaré maps corresponding to the cases of Fig. 3.5. The random chaotic attractors (black) in (c) and (d) have similar features as the deterministic chaotic attractors of (a) and (b), respectively. Figures (a) and (c) show the SCS in the deterministic and stochastic cases, respectively (green). 37

3.7 Schematical representation of transition to chaos and noise–induced intermittency in a stochastical dynamical system. 39

3.8 (a) First two Lyapunov exponents of the random chaotic attractor as a function of the noise amplitude, near the transition to a more chaotic state $D = 205.8525$. (b) The scaling of the first Lyapunov exponent of the random chaotic attractor for $\sigma \gtrsim \sigma_{\mathrm{c}}$. 40

4.1 Schemtaic diagram of the Pierce diode. 44

4.2 Numerical solutions of the Pierce diode linear dispersion relation Eq. (4.5). Black lines represent nonoscillatory solutions, and red and blue lines represent oscillatory solutions. Upper panel: linear frequencies. Lower panel: growth rates. 46

4.3 (a) Bifurcation diagram: a p–3 periodic window in the Pierce diode. Within the window the attractor (blue dots) coexists with the surrounding chaotic saddle (red dots) and a p–3 UPO (black lines). SNB (IC) denotes saddle–node bifurcation (interior crisis). (b) First (black) and second (red) Lyapunov exponents. 48

4.4 (a) Density plot of the lifetime, given in units of Poincaré map iterations, in a two–dimensional phase–space projection at $\alpha = 2.85529\pi$. Blue areas indicate initial conditions that converge quickly to the attractor. Initial conditions leading to longer lifetimes are represented by red tones. The edge of chaos is given by the boundary between the blue and red areas. (b) Schematic representation of the edge of chaos (SM) indicated by a solid line and its associated saddle object (the edge state). Any initial condition lying on the edge of chaos will converge to the edge state. . . . 49

4.5 Poincaré time series of two trajectories on the laminar side (blue circles) and chaotic side (red triangles) of the edge of chaos before converging to the p–3 periodic attractor for $\alpha = 2.85564\pi$. Poincaré points are plotted for each three iterations, $m = 1, 4, 7, \dots$ 51

4.6 Three–dimensional projection of the grid of initial conditions generated from four points A, B, C and D, containing part of the banded chaotic attractor BCA (blue) and the chaotic saddle SCS (red). 52

4.7 Two–dimensional Poincaré plots at the onset of ((a) and (b)) and after ((c) and (d)) the interior crisis. (a) Three structures involved at the onset of crisis: the banded chaotic attractor (BCA, blue), the surrounding chaotic saddle (SCS, red) and the p-3 edge state (black crosses). (b) An enlargement of the dashed rectangle region indicated in (a). The p-3 mediating UPO (the edge state) and its stable manifold (the edge of chaos, dashed line) collide with BCA and SCS . The stable (grey) and unstable (green) manifolds of SCS are also shown. (c) Post–crisis banded chaotic saddle (BCS, blue), SCS, and a p–14 coupling UPO (green crosses) with its branches in the gaps of both banded and surrounding regions. (d) An enlargement of (c). The edge state (black cross) and the edge of chaos (dashed lines) are also shown. 53

4.8 Poincaré time series showing crisis–induced intermittency. 54

5.1 Stability analysis of fixed points $\mathbf{p}_-$ (left panel) and $\mathbf{p}_+$ (right panel). For $C < 0$, the eigenvalues of $\mathbf{p}_-$ are imaginary, and the eigenvalues of $\mathbf{p}_+$ are real, one positive and one negative. $\mathbf{p}_-$ is a center and $\mathbf{p}_+$ is a saddle. When $C = 0$ both fixed points cease to exist. 62

5.2 Contours of $H(u, v)$. Each curve defines a constant energy solution of the system of equations (5.17)–(5.18). Red lines denote the stable and unstable manifolds of $\mathbf{p}_+$. 62

5.3 Solutions of Eq. (5.1) for: (a) $\epsilon = 0$ and $\nu = 0$, and (b) $\epsilon = 0.01$ and $\nu = 0.1$. 63

5.4 Bifurcation diagram of all solutions of Eq. (5.1) in the interval $\epsilon \in [0, 0.25]$. Arrows indicate bifurcations and transitions suffered by different solutions as the parameter is varied. 64

5.5 Two–dimensional projection of the Poincaré map of quasioperiodic attractor A_2 at $\epsilon = 0.131$. 65

5.6 Basins of attraction for attractors A_0 (blue) and A_2 (red), for $\epsilon = 0.095, 0.111, 0.125$ and 0.13. Black cross denotes the edge state ES in each case. 67
5.7 Dynamical mechanism that creates fractal basin boundaries and a chaotic saddle within. (a) Smooth basin boundary for $\epsilon < \epsilon^*$. (b) Homoclinic tangencies for $\epsilon = \epsilon^*$. (c) Homoclinic crossings for $\epsilon > \epsilon^*$. The stable manifold, and consequently the basin boundary, becomes fractal. Adapted from Lai and Tél (2011). 69
5.8 (a) Enlargement of bifurcation diagram for attractor A_2 (red dots) and the edge state ES (dashed black line). (b) Fractal dimension of the basin boundary as a function of ϵ. For $\epsilon \gtrsim 0.11$ (indicated by the arrow) the boundary dimension begins to increase from the unity, meaning that basin boundary becomes fractal. 70
5.9 Temporal convergence of the six positive Lyapunov exponents of the STCS chaotic saddle, for $\epsilon = 0.13$. 71
5.10 Amplitude spectra of A_0 (blue line), A_2 (red line), ES (dashed black line) and the STCS (light blue line). 71
5.11 Contourplot of the spatiotemporal evolution for the four coexisting structures at $\epsilon = 0.13$. While A_0, A_2 and ES are spatially regular, the STCS has a disordered spatiotemporal pattern. 72
5.12 Time–averaged spectral entropy of STCS as a function of ϵ. 73
5.13 (a) Number of positive Lyapunov exponents of STSC as a function of ϵ. (b) Maximum Lyapunov exponent of STSC as a function of ϵ. 74
5.14 A two–dimensional sample of phase space, showing the transient lifetime. 76
5.15 Energy time series for two initial conditions found with the bisection method for $\epsilon = 0.199$. The initial distance is 10^{-12}. The laminar trajectory (red) converges quickly to the attractor A_1, and the turbulent trajectory (light blue) goes through the STCS regime before converging to A_1. 77
5.16 Temporal convergence of the first four Lyapunov exponents of the edge state ES at $\epsilon = 0.199$. The edge state is a saddle fixed point, with one unstable direction and thirty–nine stable directions. 78

5.17 Time series of energy $E(t)$, spectral entropy $S_A(t)$, the distance to the edge state $\Delta(t)$ and mutual collective correlation function $C_{\Delta\phi}(t)$ for an initial condition in the vicinity of STCS, showing a long chaotic transient before converging to attractor A_1. Lower and higher levels of synchronization with the edge state ES coincide with higher and lower levels of spatial disorder. 81

5.18 Synchronization between ES and STCS. A solution during the transient turbulent regime synchronize with the edge state (vertical dashed blue lines) prior to the bursty release of energy (vertical arrows). 82

5.19 Enlargement of the bifuraction diagram for the attractor A_1 (red), the temporally chaotic saddle TCS (grey) and the edge state ES (dashed black). Interior crisis IC and boundary crisis are indicated. Attractor A_1 is considered to be a single structure divided in the parameter space by the chaotic saddle TCS. Due to the specific Poincaré cut, it is posible to appreciate the collision between A_1 and ES that triggers the interior crisis and the transition to spatiotemporal chaos. 83

5.20 Saddle steady wave found by He and Chian (2003) (thick red line) and edge state ES (dashed black line) plotted in the real space. Both structures are the same. 84

5.21 Collisions between the attractor A_1 and ES that trigger interior and boundary crises. (a) Temporally chaotic attractor A_1 (red) and edge state ES (black cross) colliding with each other, just before the interior crisis IC preceding the transition from temporal chaos to spatiotemporal chaos. (b) Attractor A_1 and ES colliding with each other before the boundary crisis BC. 85

5.22 Temporal evolution of energy $E(t)$, the distance to the edge state $\Delta(t)$ and the mutual colllective correlation function $C_{\Delta\phi}(t)$ showing the laminar–turbulence transition after the interior crisis IC. Vertical dashed blue lines denote the time interval when the collision between the solution and the edge state ES occurs. Red arrows indicate the energy level of ES. 86

LIST OF ABBREVIATIONS

BC – Boundary Crisis
BCA – Banded Chaotic Attractor
BCS – Banded Chaotic Saddle
ES – Edge State
GSE – Geocentric Solar Ecliptic
HB – Hopf Bifurcation
IC – Interior Crisis
ICME – Interplanetary Coronal Mass Ejection
MC – Meging Crisis
MCBL – Magnetic Cloud Boundary Layer
NCDE – Non–Compressive Density Enhancement
PB – Pitchfork Bifurcation
PDF – Probability Distribution Function
PSD – Power Spectral Density
RLWE – Regularized Long Wave Equation
SCS – Surrounding Chaotic Saddle
SNB – Saddle–node Bifurcation
STCA – Spatiotemporally Chaotic Attractor
STCS – Spatiotemporally Chaotic Saddle
SW – Steady Wave
TB – Tangent Bifurcation
TCS – Temporally Chaotic Saddle
UPO – Unstable Periodic Orbit

CONTENTS

Pág.

1 INTRODUCTION 1

2 COHERENT STRUCTURES AND MAGNETIC RECONNECTION AT THE TURBULENT LEADING EDGE OF AN INTERPLANETARY CORONAL MASS EJECTION 5

2.1 The ICME of 21 January 2005 5

2.2 Detection of current sheets 8

2.3 Turbulence and intermittency at the leading edge of the ICME 12

2.4 Magnetic reconnection 18

3 INTERMITTENCY IN A MEAN–FIELD DYNAMO MODEL . 25

3.1 Dynamical systems 25

3.1.1 Lyapunov spectrum 26

3.1.2 Numerical detection of chaotic saddles 27

3.1.2.1 The sprinkler method 28

3.1.2.2 The stagger–and–step method 28

3.2 Mean–field $\alpha\Omega$ dynamo 29

3.3 Bifurcation diagram 32

3.3.1 Periodic window 33

3.4 Interior crisis 35

3.5 Noise–induced intermittency 38

4 EDGE STATE AND CRISIS IN THE PIERCE DIODE 43

4.1 Edge of chaos 43

4.2 Pierce diode 44

4.3 Bifurcation diagram 47

4.4 Lifetime function and bisection method 49

4.5 Interior crisis 52

4.6 Intermittency 54

5 EDGE OF CHAOS AND SPATIOTEMPORALLY CHAOTIC SADDLES AT THE LAMINAR–TURBULENCE TRANSITION 57

5.1 Regularized Long–Wave Equation 57
5.2 Amplitude–phase representation and Poincaré section 58
5.3 Hamiltonian formulation 60
5.4 Attractors and bifurcations 63
5.5 Genesis of the edge state and the STCS 66
5.6 Edge of chaos at the onset of laminar–turbulence transition 75
5.6.1 Edge of chaos before IC: $\epsilon = 0.199$ 75
5.6.2 Synchronization of A_1 and STCS with the edge state ES 78
5.6.3 Interior and boundary crises 83

6 CONCLUSION 89

REFERENCES 93

APENDIX A - DERIVATION OF THE LINEAR DISPERSION RELATION FOR THE PIERCE DIODE 105

1 INTRODUCTION

Turbulence is an ubiquitous phenomenon in space and astrophysical plasmas. It can be observed in many different systems, such as the solar wind, the solar convective zone and in the interestellar medium, among others (BRANDENBURG; NORDLUND, 2011). Turbulent flows are strongly irregular and chaotic, both in space and time. Evidence of the spatiotemporal disorder in turbulence is the power spectrum of the velocity field, with an infinite number of active modes k. The inertial subrange is defined by the wavenumber interval greater than the scale of energy injection k_{in} and smaller than the dissipative scale k_{d}, as shown in Figure 1.1. Assuming that turbulence in the inertial subrange is isotropic, i.e., there are not preferential directions, and homogeneous, meaning that energy transfer rate among scales ϵ is constant and uniform, Kolmogorov (1941) developed a theory which predicts a spectral index equal to -5/3 for the power spectrum,

$$E(k) \propto k^{-5/3}. \tag{1.1}$$

This spectral index has also been observed for the magnetic fluctuations in the solar wind (BISKAMP, 2003).

Kolmogorov's assumptions of isotropy and homogeneity imply that turbulence is self–similar or monofractal. There exists observational evidence indicating the multifractal character of fluctuations of the fluid velocity in neutral fluids (FRISCH, 1995) and fluctuations of the magnetic field in the solar wind (FRISCH, 1995; BISKAMP, 2003), related to inhomogeneities present in the turbulence. In other words, the energy transfer rate depends on the scales, which is caused by the presence of coherent structures in multiple scales. Large–amplitude coherent structures are responsible for non–Gaussian probability distribution functions (PDFs) of velocity fluctuations, with this phenomena being more pronounced at smaller scales. Multifractality in turbulence is also known as intermittency.

Identification of coherent structures is a key to probing the nature of intermittent turbulence in space plasmas such as the solar wind (BRUNO; CARBONE, 2005; BOROVSKY, 2010). Current sheets are magnetic coherent structures in a localized region of electric current confined to a nearly two–dimensional surface, ubiquitous in a magnetized astrophysical plasma (VELTRI, 1999), which have been seen in numerical simulations (ZHOU et al., 2004), solar wind (GOSLING et al., 2005; GOSLING et al., 2007;

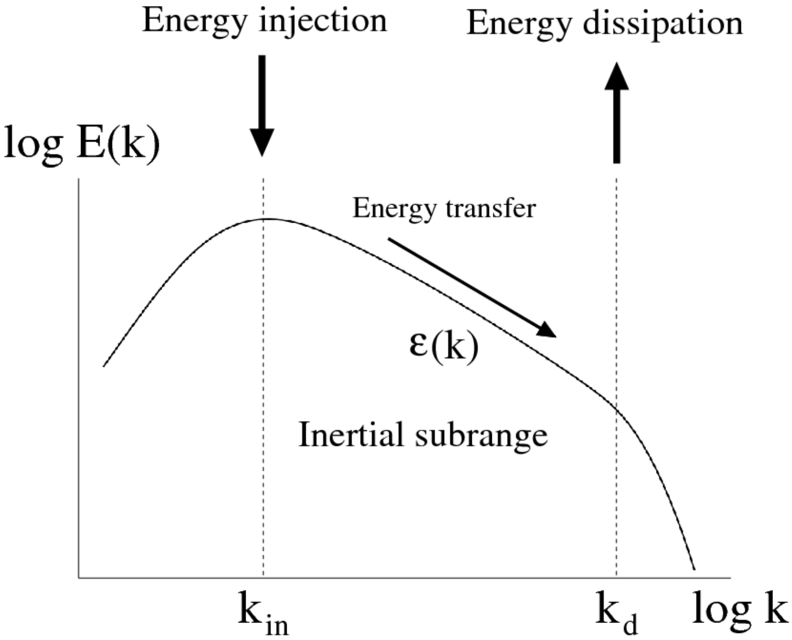

Figure 1.1 - Power spectrum density of turbulence with the characteristic power law within the inertial subrange, between the energy injection scale k_{in} and the energy dissipation scale k_{d}.

PHAN et al., 2006; LI, 2008; CHIAN; MUÑOZ, 2011) and solar flares (LIU et al., 2010). Magnetic reconnection in a current sheet is a fundamental mechanism that converts magnetic energy into plasma kinetic energy in astrophysical systems (NISHIDA, 2007; PRIEST, 2007). Interplanetary shocks and magnetic cloud boundary layers (MCBL) are formed by the interaction of an interplanetary coronal mass ejection (ICME) emanating from a solar active region with the ambient solar wind (WEI et al., 2003a; WEI et al., 2003b; BOUGERET; PICK, 2007; CARGILL; HARRA, 2007), which leads to a local enhancement of intermittency in the interplanetary turbulence, characterized by the kurtosis–skewness interdependence, via cross–scale coupling between large–scale structures such as shock boundaries and small–scale fluctuations (VÖRÖS et al., 2006).

Transition to turbulence is a very important open question in fluid dynamics (ECKHARDT, 2008). Since the famous work of Lorenz (1963), the dynamical systems approach has been extensively used to model turbulent flows. In the last years, many efforts have been made using the dynamical systems approach, in order to figure out the underlying mechanisms in this transition. Two remarkable results emerge from this approach: (i) the importance of chaotic transients, and (ii) the critical role of a coherent structure called the edge state.

Experimental evidence and numerical simulations have shown the existence of chaotic transients in shear flows (SCHMIEGEL; ECKHARDT, 1997; AVILA et al., 2010). Chaotic transients in nonlinear dynamical systems are due to non–attracting chaotic sets known as chaotic saddles. In the last years the chaotic saddles have attracted wide attention due to their role in the transition to turbulence in neutral fluids (WILLIS; KERSWELL, 2007; HOF et al., 2008). Despite these results, almost no studies relating turbulent transients and transition to turbulence in plasmas have been performed. Recently Rempel et al. (2010) studied transition to turbulence in magetized acretion disks showing that the lifetime of turbulence transients obeys a supertransient law (TÉL; LAI, 2008).

The edge state is a coherent structure which lies at the boundary between the laminar and turbulent states. Skufca et al. (2006) studied the edge of chaos in a low–dimensional model for the plane Couette flow, showing that the edge state is a hyperbolic structure that is attracting over the edge of chaos, and for a range of control parameters this structure becomes chaotic. The same ideas were applied in Schneider et al. (2007) for a pipe flow using direct numerical simulations. For this case the edge state was found to be formed by two symmetrical vortices. The edge state between two asymptotic solutions was found in Cassak et al. (2007) for a two–dimensional MHD numerical model of magnetic reconnection.

The aim of this thesis is to study the relationship between coherent structures and fundamental processes in nonlinear spatially–extended systems, such as intermittency, energy transfer and dissipation, and transition to turbulence, using both observational data of turbulence in the solar wind and a set of theoretical models of chaotic and spatiotemporally chaotic systems.

This thesis is organized as follows. In Chapter 2 the relation between current sheets, intermittent turbulence and magnetic reconnection in the leading edge of an ICME is investigated. In Chapter 3 we introduce basic concepts on dynamical systems. We first apply them to study crisis and noise–induced intermittency in a nonlinear low–dimensional model for the mean–field solar dynamo. In Chapter 4 crises and chaotic saddles are invesigated in the Pierce diode, a one–dimensional spatially–extended plasma model described by fluid equations, introducing the concept of edge state. In Chapter 5 we use a model of nonlinear drift waves in plasmas (or long waves in shallow waters) to study the problem of laminar–turbulence transition. The origin of the edge state and a spatiotemporally chaotic saddle, and the role played by them in the laminar–turbulence transition are investigated. The conclusions are presented in Chapter 6.

2 COHERENT STRUCTURES AND MAGNETIC RECONNECTION AT THE TURBULENT LEADING EDGE OF AN INTERPLANETARY CORONAL MASS EJECTION

Coronal mass ejections are a major form of solar activity. They involve the expulsion of large amounts of plasma and magnetic flux at high speeds from the solar corona into the solar wind, are believed to be responsible for the acceleration of coronal ions to high energies, and their manifestation in the solar wind, the interplanetary coronal mass ejection (ICME), is responsible for many major disturbances to the Earth's space environment (CARGILL; HARRA, 2007). A schematic diagram of an ICME is shown in Figure 2.1. A magnetic shock is formed ahead the ejected mass by its interaction with the ambient solar wind. Between the shock and the plasma a turbulent region, called sheath, is formed. The magnetic cloud, behind the ejecta, is the large scale magnetic structure carrying magnetic flux from the corona.

In this Chapter we study the relation between current sheets, turbulence and magnetic reconnections at the leading edge of an ICME intercepted by the four *Cluster* spacecraft in the solar wind on 2005 January 21 (FOULLON et al., 2007; DU et al., 2008; MIRANDA et al., 2010; MUÑOZ et al., 2010). A few papers that deal with magnetic turbulence in ICME only tackle the region inside a magnetic cloud (LEAMON et al., 1998; LIU et al., 2006). We report for the first time the observational evidence of a Kolmogorov magnetic turbulence in the vicinity of two magnetically reconnected current sheets at the front MCBL that exhibits the She–Leveque multifractal scaling and signatures of bifurcated current sheets. Recent investigations of interplanetary and geomagnetic data show that the leading edge of an ICME triggers the initial phase of geomagnetic storms (DU et al., 2008; ZUO et al., 2010). Hence, an improved knowledge of the physical processes that occur at/near the front MCBL is important for understanding the dynamics of star–planet relation.

2.1 The ICME of 21 January 2005

Figure 2.2 provides an overview of the magnetic field and plasma parameters measured by Cluster–1 from 16:42:00 UT to 20:24:00 UT of 21 January 2005, which shows the modulus of magnetic field $|\mathbf{B}|$ (nT); the three components of the vector magnetic field B_x, B_y and B_z in the GSE coordinates; the angles Φ_B and θ_B (degrees) of the magnetic field relative to the Sun–Earth x–axis in the ecliptic plane and out of the plane, respectively, in the polar GSE coordinates (CHIAN; MIRANDA, 2009).

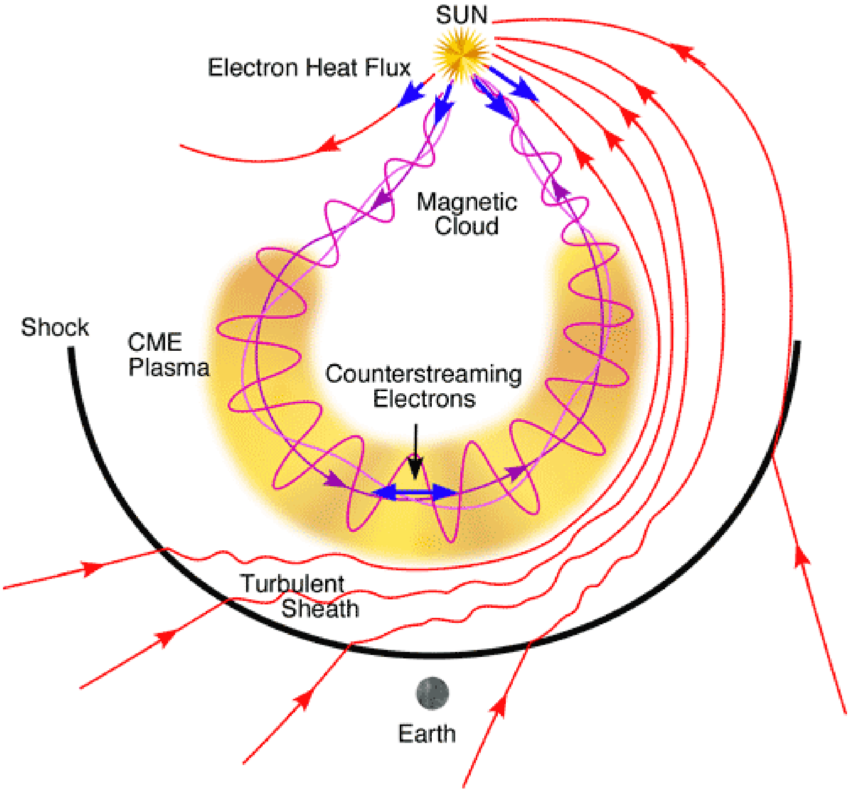

Figure 2.1 - Schematic diagram of an ICME ejected from the Sun.
SOURCE: Lang (2009)

Figure 2.2 also shows the speed of the ions $|\mathbf{V}|$ (km/s); the ion number density N_i (cm^{-3}); the ion temperature T_i (°K), and the ion plasma beta β. Two discontinuities are identified in the time series, marked by vertical dashed lines in Figure 2.2. First, the shock arrival (SA) at 17:10:20 UT, where the modulus of the magnetic field undergoes a sudden increase from ∼5 nT to ∼30 nT, accompanied by jumps in $|\mathbf{V}|$, N_i, T_i and β. Then, a non–compressive density enhancement (NCDE) occurs at 18:44:05 UT related to the leading boundary of the ejecta, denoted by SB, characterized by an increase of the plasma density from ∼13 cm^{-3} to ∼40 cm^{-3}. The SB is associated with a decrease of T_i and an increase of the plasma beta (MUÑOZ et al., 2010). Foullon et al. (2007) found that the ejecta front forms behind a magnetic discontinuity. As shown in Figure 2.2, magnetic field points mainly towards the Sun and southward ($B_x > 0$ and $B_z < 0$), before and after the passage of the ejecta front layer, but in the opposite way within the layer. The boundaries of this front layer are called SB1 and SB2. The three regions of the ICME observed by Cluster

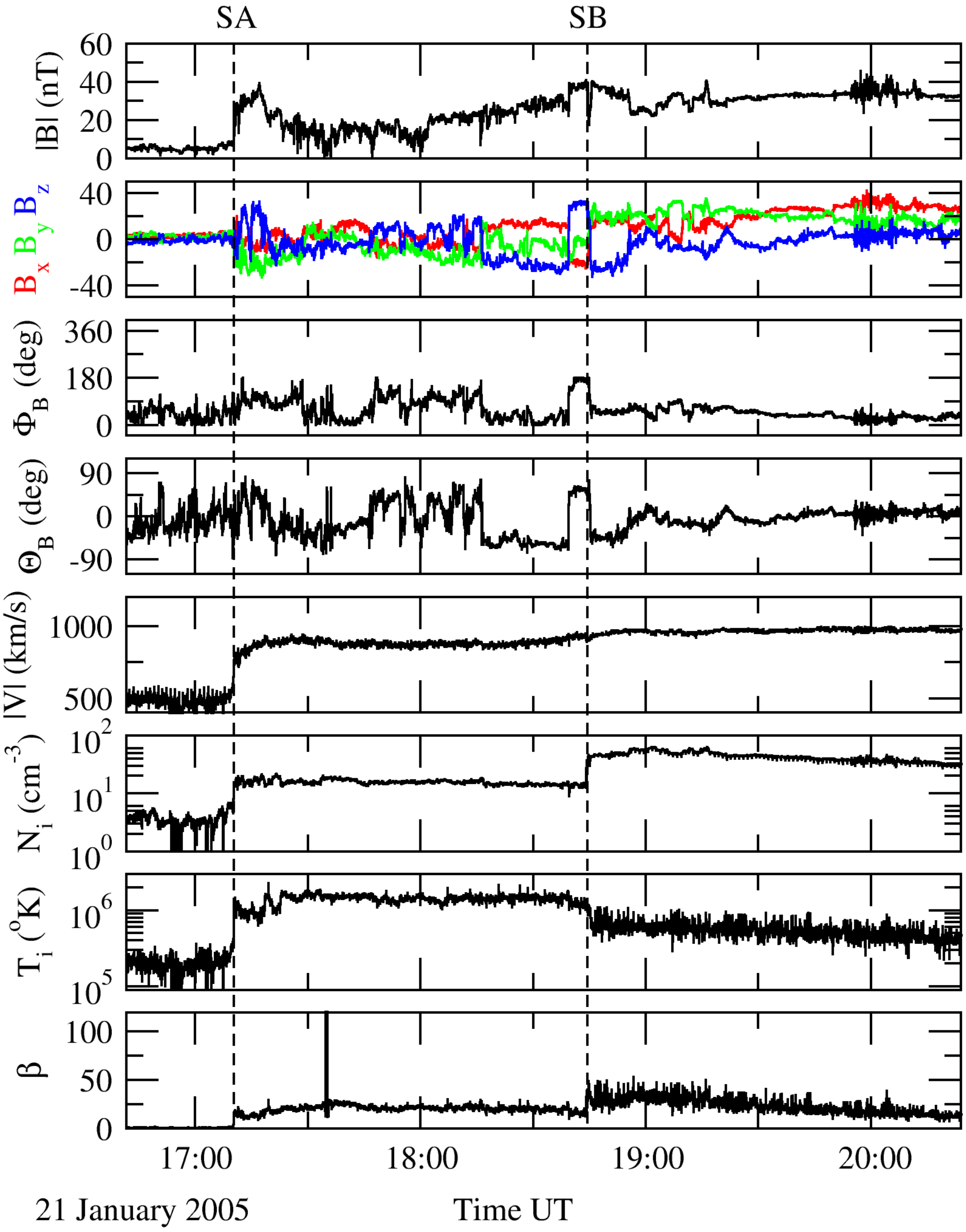

Figure 2.2 - Overview of the ICME event of 21 January 2005 as measured by Cluster–1. From top to bottom: modulus of magnetic field $|\mathbf{B}|$ (nT); the three components of the vector magnetic field B_x, B_y and B_z in the GSE coordinates; angle Φ_B (degrees) of the magnetic field relative to the x-axis in the ecliptic plane; angle Θ_B of the magnetic field out of the ecliptic; the speed of the ions $|\mathbf{V}|$ (km/s); ion number density N_i (cm^{-3}); ion temperature T_i (°K), and ion plasma beta β. The arrival shock (SA) and the leading boundary of the ejecta (SB) are marked by dashed lines.

are the upstream region, before SA, characterized by quiet solar wind conditions, the sheath, between SA and SB, characterized by large magnetic fluctuations and a faster plasma speed, and the NCDE region, denser and colder.

2.2 Detection of current sheets

Identification of coherent structures is a key to probing the nature of intermittent turbulence in astrophysical plasmas such as the solar wind (BRUNO; CARBONE, 2005; BOROVSKY, 2010). Current sheets are magnetic coherent structures in a localized region of electric current confined to a nearly two–dimensional surface, ubiquitous in a magnetized astrophysical plasma (VELTRI, 1999), which have been seen in numerical simulations (ZHOU et al., 2004), solar wind (GOSLING et al., 2005; GOSLING et al., 2007; PHAN et al., 2006; LI, 2008) and solar flares (LIU et al., 2010).

A characteristic feature of current sheets is the significant change in magnetic field rotation from one side to the other of the structure.This fact was used by Li (2008) to develop a systematic method to search for current sheets using single-spacecraft magnetic field data. Consider a time series of magnetic field data $B(t)$. The problity density of finding an angle between $B(t)$ and $B(t + \tau)$ within the interval θ and $\theta+\Delta\theta$ can be computed directly from magnetic field measurements as

$$f(\theta, \tau)\Delta\theta = \frac{N^{\tau}(\theta < \theta' < \theta + \Delta\theta)}{N^{\tau}(0 < \theta' < \pi)}, \tag{2.1}$$

where $N^{\tau}(\theta < \theta' < \theta + \Delta\theta)$ is the number of measurement pairs where the angle between $B(t)$ and $B(t + \tau)$ is within the range θ and $\theta + \Delta\theta$. The integrated distribution function is defined as

$$F(\theta, \tau) = \int_{\theta}^{\pi} d\theta' \, f(\theta', \tau), \tag{2.2}$$

representing the frequency of having the measured angle larger than θ. If there are current sheets associated with the magentic field time series, the quantity $F(\theta, \tau)$ shall scale linearly with the time separation τ when θ is larger than some critical angle θ_0, i.e.,

$$F(\theta, N\tau) \sim NF(\theta, \tau) \qquad \text{when} \qquad \theta > \theta_0. \tag{2.3}$$

The localization of the current sheets is determined by the local statistical properties of the function $F(\theta, \tau)$, as shown in Fig. 2.3. If the majority ($> 60\%$) of the angles

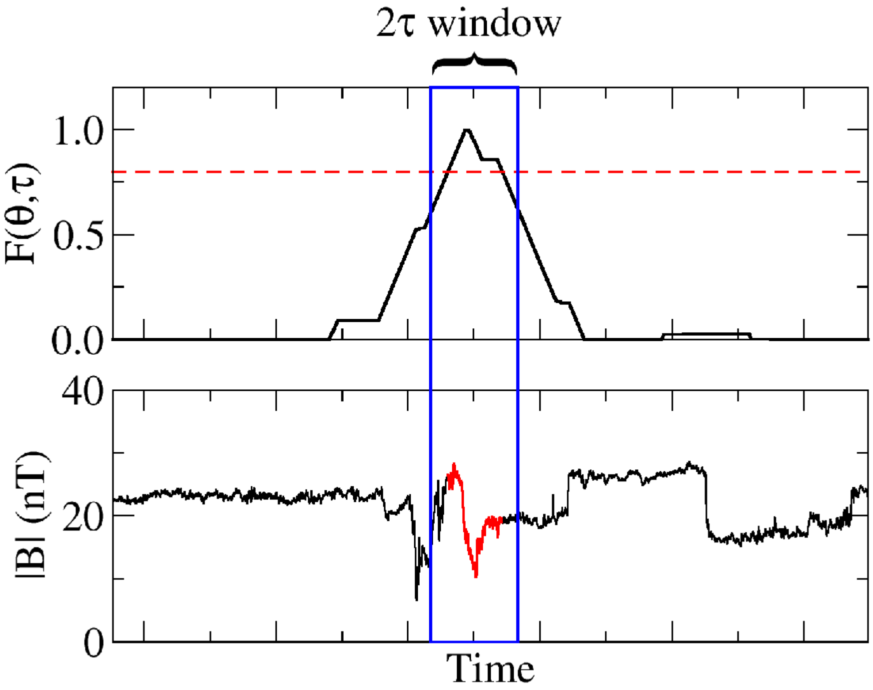

Figure 2.3 - Li (2008) method to locate current sheets within a magnetic field time series.

between $B(t)$ and $B(t+\tau)$ in a window of size 2τ centered at time T are greater than θ, then a current sheet is located at T. In Fig. 2.3 this threshold is denoted by the dashed red line in the upper panel. A current sheet, denoted by red dots, is detected within the sliding window (blue box). The parameter τ define the typical size (scale) of the current sheets found with this procedure.

We apply the above single–spacecraft method to systematically search for current sheets in the ICME event of 21 January 2005, based on the Cluster magnetic field data. To show the existence of current sheets in the time series of the magnetic field, the function $F(\theta,\tau)$ has to be well ordered as a function of θ in the range of scales of the current sheets. The upper panel of Figure 2.4 shows the function $F(\theta,\tau)$ as a function of θ for four different time scales τ. For large–scales ($\tau = 30, 60, 120, 240$ seconds) the curves are nicely ordered with respect to θ. The lower panel of Figure 2.4 shows an almost linear dependence of $F(\theta,\tau)$ with τ for different critical angles ($\theta = 60°, 80°, 100°, 120°$). This linear behavior of $F(\theta,\tau)$ as a function of τ is expected if there are current sheets within the time series, according to equation (2.3).

Figure 2.5 shows the position of current sheets (red dots) found by the method

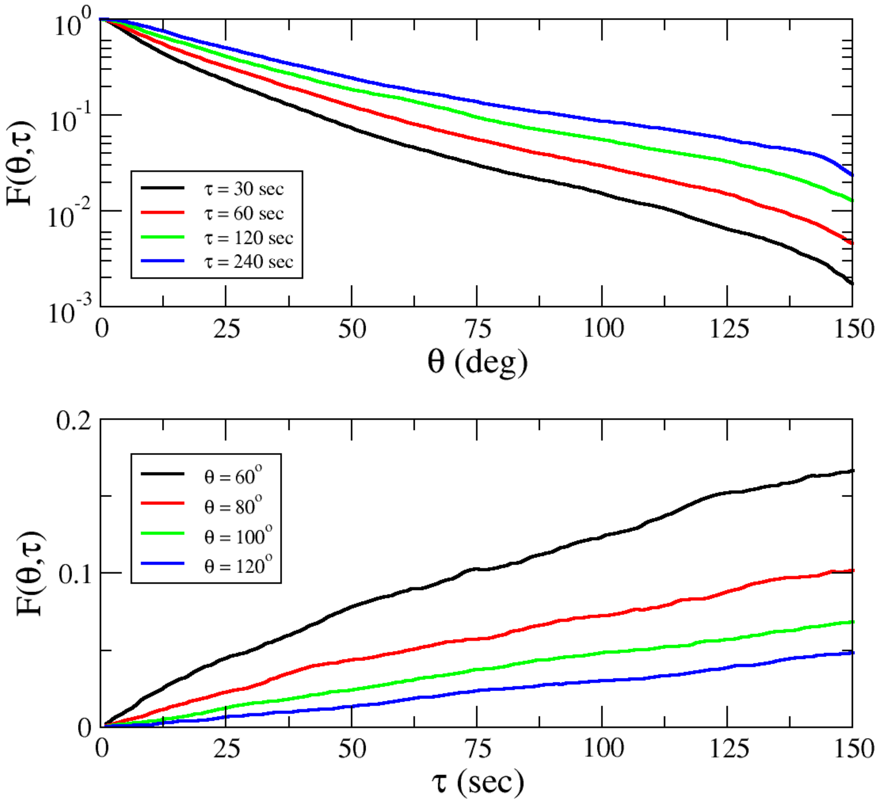

Figure 2.4 - Upper panel: $F(\theta, \tau)$ as function of θ. For large–scales ($\tau = 30, 60, 120, 240$ sec) $F(\theta, \tau)$ are nicely ordered with respect to θ. In addition, when $60° < \theta < 120°$ the curves are approximately parallel to each other. Lower panel: $F(\theta, \tau)$ as function of τ for different values of θ. A linear behavior is clearly seen for different critical angles, in agreement with equation (2.3).

fixing the time scale $\tau = 120$ seconds for the same critical angles as in the upper panel of Figure 2.4. When the critical angle value increases, the number of current sheets detected decreases, in agreement with the behaviour of $F(\theta, \tau)$ in the upper panel of Figure 2.4. For all values of θ, both sides of the front layer that forms the leading edge of the ejecta, SB1 and SB2, are detected as current sheets. These are well localized structures, since the large variation in the magnetic field angles Φ_B and Θ_B (Figure 2.2) is captured by the statistical properties of the sliding window of size 2τ when it passes through the discontinuities.

The shock arrival SA is also classified as a current sheet, but for $\theta = 120°$ it is no longer detected. Figure 2.6 shows the current sheets detected with the single–spacecraft method, fixing the critical angle $\theta = 60°$ and varying the time scale τ,

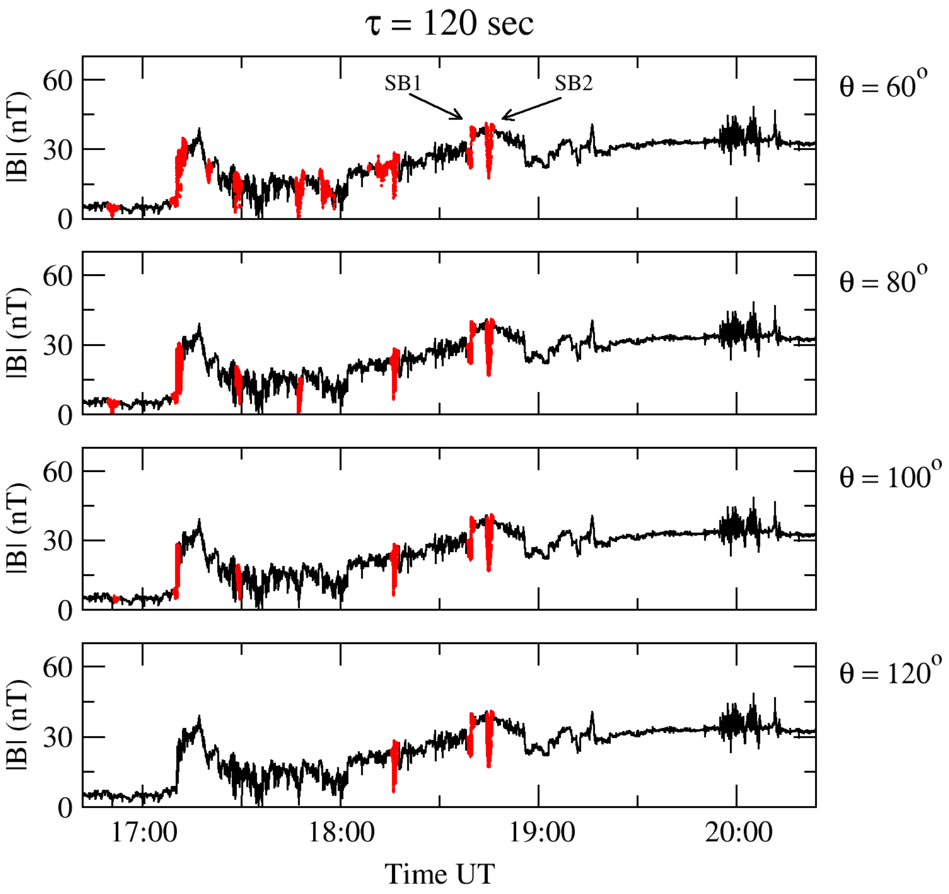

Figure 2.5 - Current sheets of size $\tau = 120$ seconds detected by the single-spacecraft method applied over the time series of $\mathbf{B}$ (black line), using four critical angles θ. The position of the currents sheets are marked by red dots. The number of CS detected decrease as θ is increased, as expected from $F(\theta, \tau)$ in the upper panel of Fig. 2.4. Three CS, including both at the leading edge of the ejecta are detected in all cases.

using the same values as the lower panel of Figure 2.4. The number of current sheets detected increases as τ is increased, as is expected from Figure 2.4. A relevant point is that for the first three time scales the current sheets detected are almost the same, just varying in size (number of red dots). Both sides of the leading edge SB1 and SB2 are detected again in all cases, even for the smallest τ. For $\tau = 240$ seconds SB1 and SB2 appear merged, because the window of size 2τ is larger than the separation between SB1 and SB2. Indeed, this merging can occur for any pair of current sheets with a temporal size comparable with their time separation. The shock arrival SA is detected as a current sheet for the last three values of τ. This non–persistence

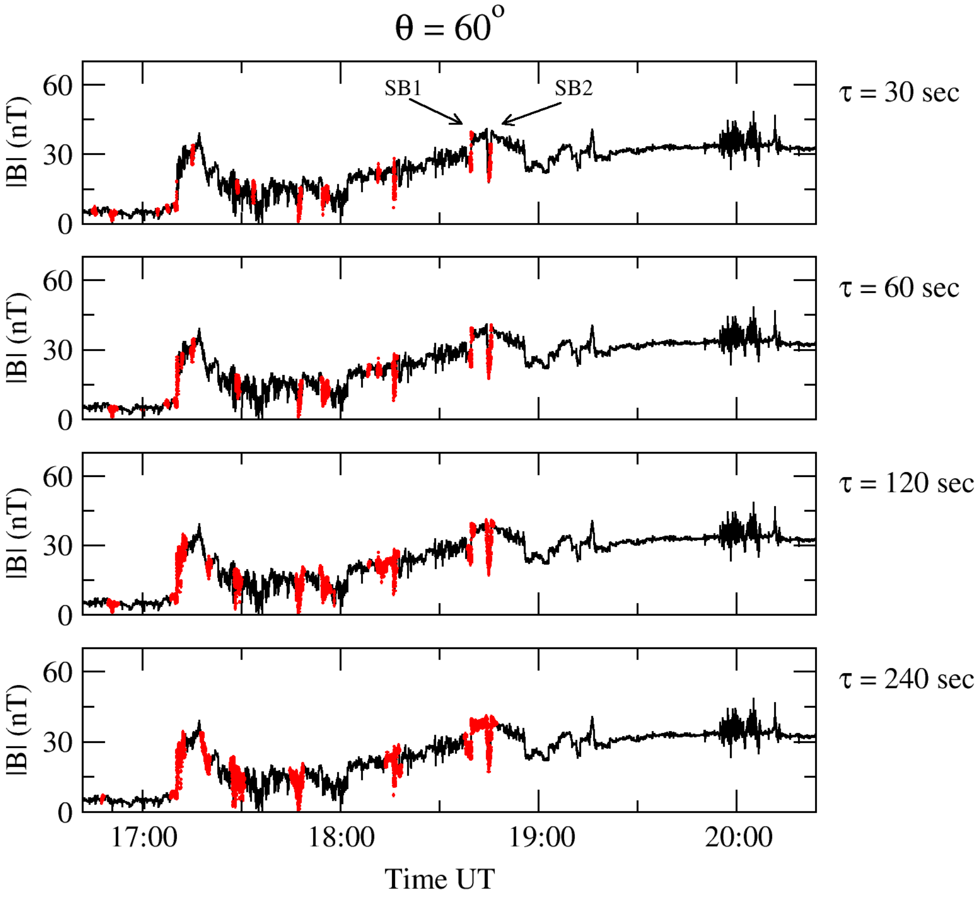

Figure 2.6 - Current sheets detected with the single–spacecraft method, fixing the critical angle $\theta = 60°$ using four time scales τ. The number of points considered as being part of a current sheet (red dots) increases as τ is increased, as expected from $F(\theta, \tau)$ in the lower panel of Fig. 2.4.

behaviour can be explained by examining the magnetic angles Φ_B and Θ_B around the SA, in Fig. 2.2. The direction of the magnetic field does not present a coherent variation around the transition, producing the ambiguous results in Figs. 2.5 and 2.6. A remarkable fact from Figs. 2.5 and 2.6 is that the majority of current sheets detected are in the sheath region, between SA and SB.

2.3 Turbulence and intermittency at the leading edge of the ICME

In this Section we discuss the relation between coeherent structures, such as the current sheets found in Section 2.2, and the turbulent intermittency at the leading edge of the ICME, studying departure from Gaussianity and multifractality of the

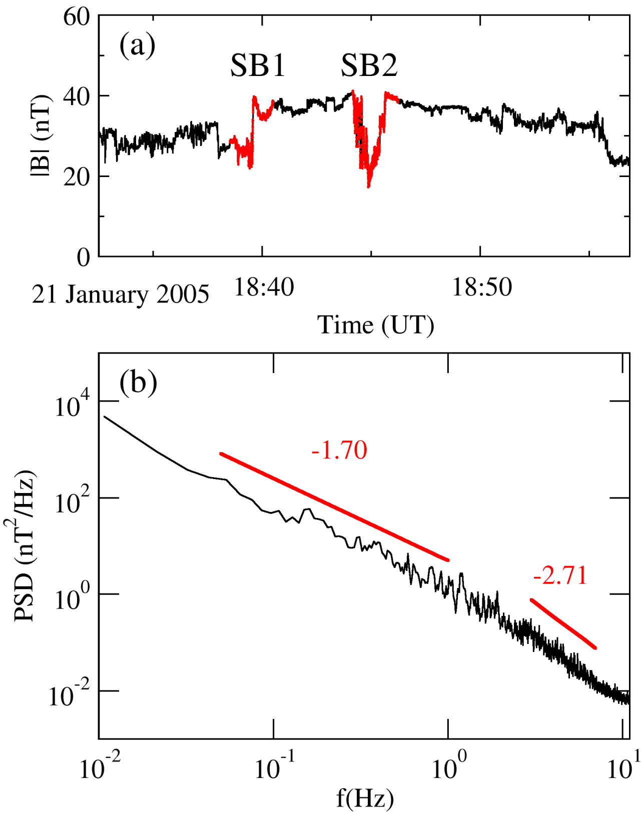

Figure 2.7 - (a) Modulus of the magnetic field $|\mathbf{B}|$ in the time interval containing the two current sheets SB1 and SB2 associated with the leading edge (SB) of the ICME ejecta. (b) Power spectral density, PSD ($\mathrm{nT}^2\ \mathrm{Hz}^{-1}$), of $|\mathbf{B}|$ for the time interval of (a); straight lines indicate the inertial and dissipative subranges. The spectral indices are calculated by a linear regression of the log–log PSD data.
SOURCE: Chian and Muñoz (2011)

magnetic fluctuations.

Figure 2.7(a) shows the modulus of the magnetic field $|\mathbf{B}|$ in the vicinity of the magnetic cloud boundary layer (MCBL). This boundary layer is formed by two current sheets SB1 and SB2, detected by the single–spacecraft method on Section 2.2 and denoted by red dots in Fig. 2.7(a). The power spectral density (PSD) of magnetic fluctuations of Fig. 2.7(a) is computed using the Welch method (WELCH, 1967), by dividing the time series into a set of overlapping subintervals and computing the PSD of each subinterval by the fast Fourier transform. The average of the set of power spectra gives the PSD of Fig. 2.7(b). The spectral index for the inertial

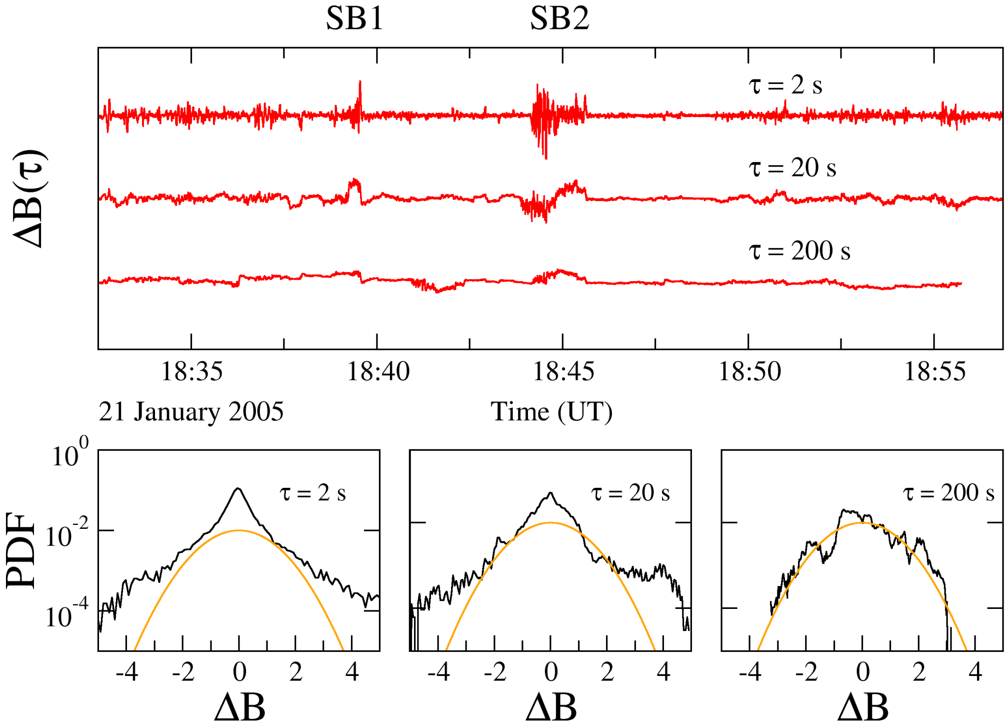

Figure 2.8 - Scale dependence for three different timescales (τ=2 s, 20 s and 200 s) of Fig. 2.7(b). (a) The normalized magnetic–field two–point differences ΔB. (b) The probability density function PDF of ΔB, superposed by a Gaussian PDF (orange line).
SOURCE: Chian and Muñoz (2011)

subrange -1.70 ± 0.05 is calculated by a linear regression of the log–log PSD data in the frequency range 0.05–1 Hz, which is determined by the compensated PSD technique of Biskamp et al. (1999). The same procedure is applied to obtain the spectral index for the dissipative subrange -2.71 ± 0.05 in the frequency range 3–7 Hz. The correlation coefficients r^2 of the linear regression are 0.93 and 0.86, respectively, for the inertial and dissipative subranges. Fig. 2.7(b) provides the first observational evidence of a Kolmogorov power spectra $-5/3$ in the inertial subrange of the magnetic turbulence in the vicinity of a front MCBL.

The scale dependence for three different timescales (τ=2 s, 20 s, 200 s) of the normalized two–point difference of the modulus of magnetic field and the probability density function (PDF) are shown in the upper panel of Fig. 2.8, where $\Delta B = (\delta B - \langle \delta B \rangle)/\sigma_B$, $\delta B(\tau) = |\mathbf{B}(t+\tau)| - |\mathbf{B}(t)|$ denotes the two-point difference of $|\mathbf{B}|$ for a given timescale τ, the angle brackets denote the mean value of δB, and σ_B denotes the standard deviation of δB. The upper panel of Fig. 2.8 shows that the magnetic field fluctuations at the leading edge of the ICME, in the vicinity of the two current sheets SB1 and SB2, become more intermittent as the scale becomes smaller. The three timescales in the upper panel of Fig. 2.8 correspond to 1,858 km, 18,580 km, and 185,800 km, respectively, if we assume the Taylor's hypothesis and use the mean ion bulk speed of $\langle|\mathbf{V}_{\rm SW}|\rangle$=929 km s^{-1} measured in this time interval. The lower panel of Fig. 2.8 shows that the PDF of ΔB at the leading edge of ICME is close to a Gaussian distribution at large timescales, but deviates significantly from a Gaussian distribution as the timescale decreases. At small scales, the shape of the PDF becomes non–Gaussian and leptokurtic, displaying sharp peaks at $\Delta B \sim 0$ and fat tails at large ΔB, due to an excess of small– and large–amplitude fluctuations in the SB1 and SB2 regions seen in the upper panel of Fig. 2.8.

We characterize first the multifractal nature of the turbulent boundary layers at the leading edge of ICME by computing the scaling exponents of structure functions of magnetic fluctuations,

$$S_p(\tau) = \langle|\delta B(\tau)|^p\rangle \sim \tau^{\alpha(p)}, \tag{2.4}$$

where the angle brackets denote ensemble averaging over time, and p denotes the order of structure functions within the inertial subrange, and comparing them against the Kolmogorov's K41 universality theory which is based on the simplified assumptions of homogeneity, isotropy, incompressibility, and stationarity (POLITANO; POUQUET, 1995). Upper panel of Fig. 2.9 shows the structure functions as a function of the timescale τ for $p = 1, \ldots, 6$. The scale is logarithmic for both axes. The inertial subrange, denoted by the horizontal arrow, is the interval where the curves have an approximately linear behavior for all p. We then apply the extended self–similatiry (ESS) technique of Benzi et al. (1993) to improve the calculation of the scaling exponent, $S_p(\tau) \sim [S_3(\tau)]^{\zeta(p)}$, where $\zeta(p) \sim \alpha(p)/\alpha(3)$ is found from the extended range, as shown in the lower panel of Fig. 2.9. The horizontal arrow denotes the original inertial subrange. The scaling exponent for each integer order p of the structure function can be obtained by estimating the slope of a linear fitting of the curves within the inertial subrange.

Figure 2.10 shows the scaling exponent $\zeta(p)$ as a function of p for the time series of Fig. 2.7(a). The black dashed line denotes the K41 self–similar scaling, $\zeta(p) = p/3$. The statistical scaling properties of the observed magnetic fluctuations (indicated by

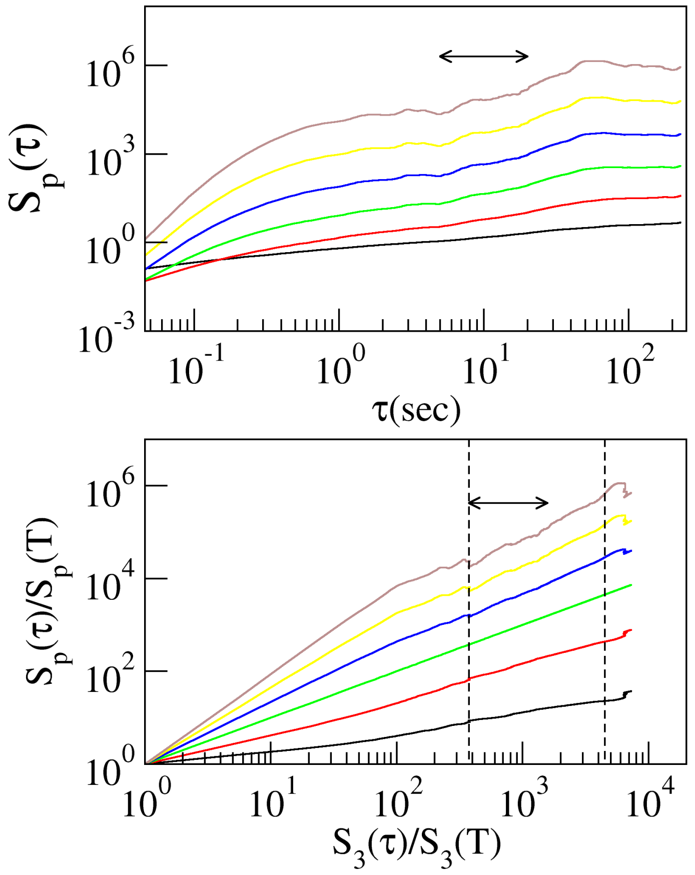

Figure 2.9 - Upper panel: structure functions vs. timescale τ for $p = 1$ (black), $p = 2$ (red), $p = 3$ (green), $p = 4$ (blue), $p = 5$ (yellow) and $p = 6$ (brown). Lower panel: structure functions after applying the Extended Self–Similarity technique. Horizontal arrow represents the previous inertial subrange.

a diamond symbol) in Fig. 2.10 display a noticeable departure from self–similarity. As shown by both panels of Fig. 2.8, the origin of intermittency and non–Gaussianity is the excess of small–scale large–amplitude fluctuations, such as in the regions of SB1 and SB2. The coherent structures, including SB1 and SB2, embedded in the intermittent magnetic turbulence result from amplitude–phase synchronization related to nonlinear multiscale interactions (KOGA et al., 2007; CHIAN; MIRANDA, 2009; CHIAN et al., 2010).

Several models have been proposed to improve the prediction of universality in fluid and magnetohydrodynamic (MHD) turbulence. A model of universal scaling laws for fully developed turbulence in fluids was postulated by She and Leveque (1994) in

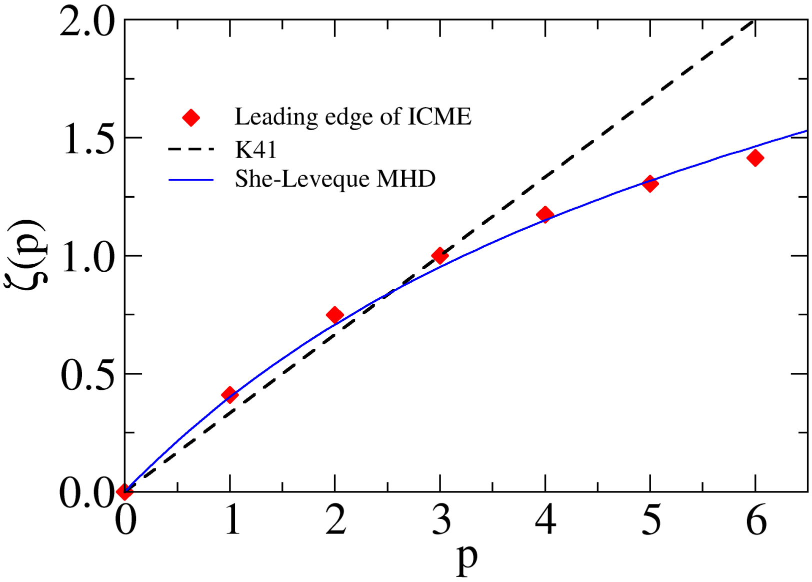

Figure 2.10 - Scaling exponent ζ of the pth–order structure function for observed values (red diamonds), superposed by the K41 self–similar scaling (black dashed line), and the multifractal prediction of the She–Leveque MHD model (blue curve).
SOURCE: Chian and Muñoz (2011)

terms of scaling of a sequence of moment ratios of the energy dissipation field coarse grained at the inertial subrange scale, whereby the moment ratios form a hierarchy of structures and the most singular structures are assumed to be vortex filaments. This model is successful in reproducing both experimental and numerical data of fluid and plasma turbulence. An extension of the universal scaling of She and Leveque (1994) was developed by Politano and Pouquet (1995) in the framework of the Iroshnikov–Kraichnan theory of MHD turbulence for sheetlike dissipative structures, and by Müller and Biskamp (2000) and Müller et al. (2003) within the framework of the Kolmogorov $k^{-5/3}$ law for sheetlike dissipative structures in isotropic and anisotropic MHD turbulence, respectively. In Fig. 2.10 we compare the observed scaling exponents of magnetic turbulence with the She–Leveque MHD model (blue curve) of Müller et al. (2003),

$$\zeta_p = p/g^2 + 1 - (1/g)^{p/g}, \tag{2.5}$$

where g is an adjustable parameter. Evidently, the prediction of the She–Leveque

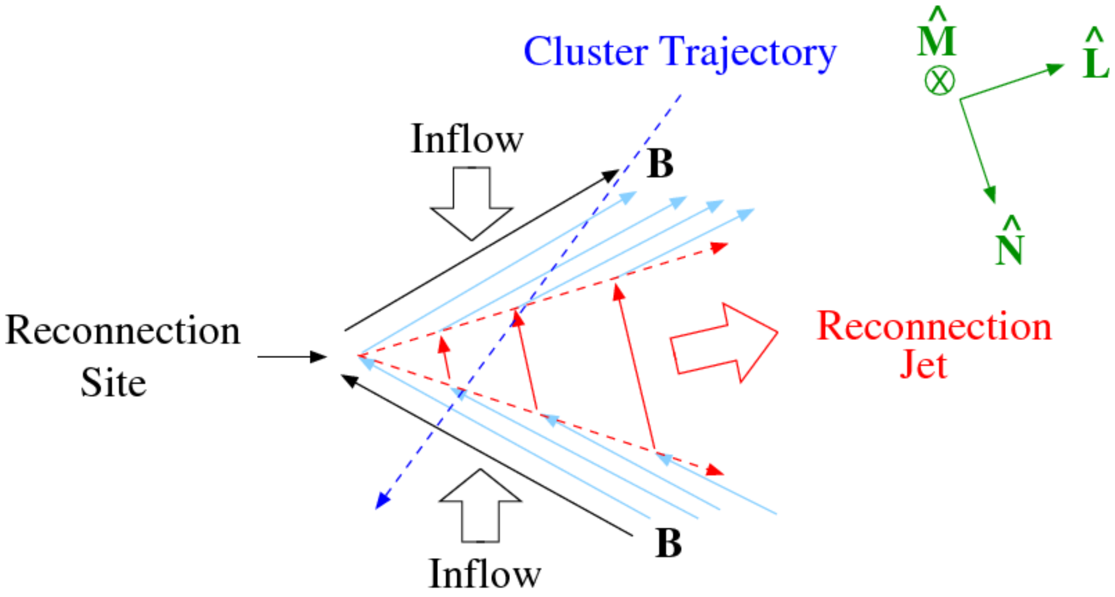

Figure 2.11 - Idealized two–dimensional reconnection exhaust region bounded by a bifurcated current sheet. The field line kinks associated with magnetic reconnection propagate as Alfvén waves along the field lines accelarating plasma away from the reconnection site (adapted from Gosling et al. (2005)).

model for anisotropic MHD turbulence closely reproduces the observed scaling of interplanetary magnetic turbulence, for $g = 3.2257$. Our results also render support for the anisotropic Kolmogorov theory of Alfvén turbulence developed by Goldreich and Sridhar (1995), and present the first evidence of the multifractal universality of magnetic fluctuations in the neighborhood of a front MCBL.

2.4 Magnetic reconnection

In this Section we discuss the detection of magnetic reconnections associated with the two currents sheets SB1 and SB2. Magnetic reconnection in a current sheet is a fundamental mechanism that converts magnetic energy into plasma kinetic energy in astrophysical systems (NISHIDA, 2007; PRIEST, 2007). Gosling et al. (2005) found evidence of the existence of plasma exhausts in the solar wind observed in the interior of an ICME. According to their model (Figure 2.11), as a result of magnetic reconnection, the exhaust region is bounded on either side by kinks that propagate as Alfvén waves along the reconnected field lines. Plasma is accelerated away from the reconnection site when it enters into the exhaust region from both sides. Since Alfvén waves propagating parallel (antiparallel) to **B** produce anticorrelated (correlated) variations in **B** and **V**, anticorrelated (correlated) changes in **V** and **B** are expected at the upper (lower) side of the exhaust region, represented by the dashed red arrows in Figure 2.11. Furthermore, it is expected to observe a depletion of the magnetic field strength at the center of the exhaust region. Note that a larger field rotation occurs across these exhaust edges. Then, the current sheet has a bifurcated structure as seen far from the reconnection site. This splitting of the original reconnecting thin current sheet is a result of the reconnection process (GOSLING et al., 2005).

A quantitative comparison between observations and the model can be made by investigating how well the observed velocity changes match with those predicted from the so–called Walen condition (HUDSON, 1970). From the constancy of the tangential electric field accross any discontinuity, and conservation of mass flux and momentum, it is possible to find an equation for the change of velocity vector $\mathbf{V}_2 - \mathbf{V}_1$ occurred when a plasma passes through an Alfvén wave (SONNERUP et al., 1981):

$$\mathbf{V}_2 - \mathbf{V}_1 = \pm[\rho_1(1-\alpha_1)/\mu_0]^{1/2}(\mathbf{B}_2/\rho_2 - \mathbf{B}_1/\rho_1), \tag{2.6}$$

where subscripts 1 and 2 refer to points upstream and dowsntream from the edge of the exhaust region, respectively. The + and - signs represent, respectively, waves propagating antiparallel and parallel to **B**, ρ is the mass density, μ_0 is the permability of vacuum, and α is the pressure anisotropy defined by

$$\alpha = (p_{\parallel} - p_{\perp})\mu_0/B^2, \tag{2.7}$$

where $p_{\parallel}$ and $p_{\perp}$ are the components of the pressure tensor parallel and perpendicular to **B**.

Figure 2.12 shows the time series of the modulus of the magnetic field $|\mathbf{B}|$ (nT), the modulus of observed ion velocity $|\mathbf{V}|$ (km s^{-1}, black line) and the plasma velocity (orange line) predicted by the magnetic reconnection theory of Sonnerup et al. (1981), and the modulus of current density $|\mathbf{J}|$ (nA m^{-2}) computed from **B** by the curlometer method of Dunlop et al. (2002) using four *Cluster* spacecraft. Intense localized current density is clearly seen in the regions of SB1 and SB2 in Fig. 2.12. The magnetic field data of SB1 and SB2 is analyzed using the minimum variance analysis (MVA) to find the direction along which the field component has minimum variance (N direction), and the directions of maximum (L) and intermediate (M)

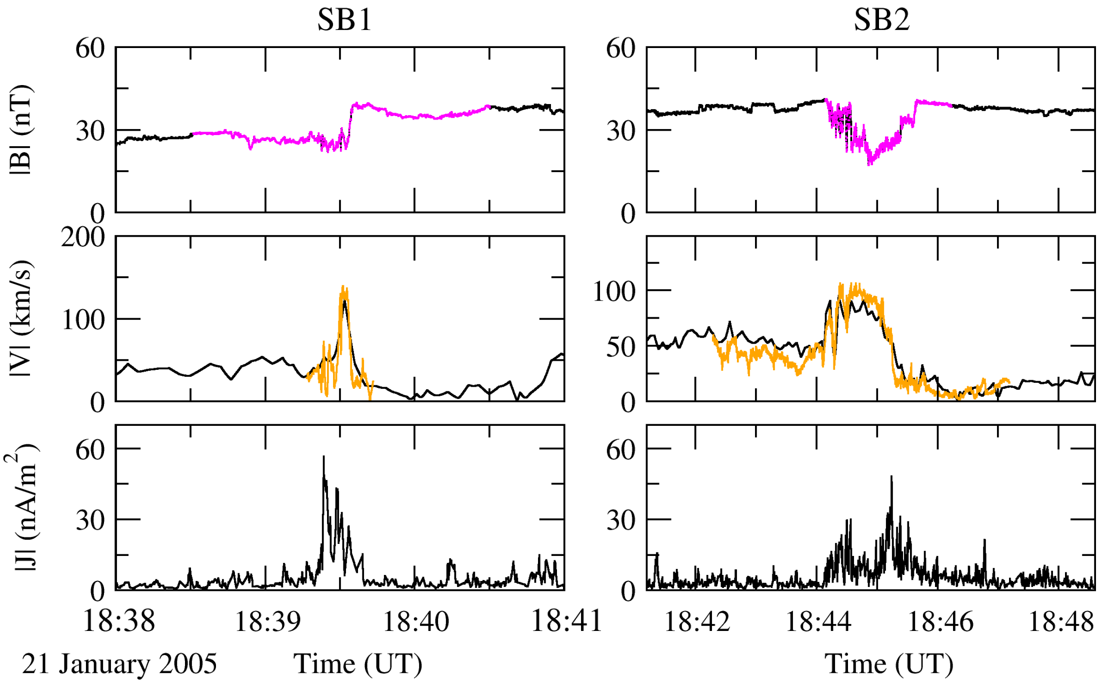

Figure 2.12 - Detection of magnetic reconnections at the leading edge of ICME associated with the current sheets SB1 and SB2 (magenta). $|\mathbf{B}|$ (nT) is the modulus of magnetic field (enlargement of Fig. 2.7(a); $|\mathbf{V}|$ (km s^{-1}) is the modulus of the observed plasma velocity (black) and the plasma velocity (orange) predicted by the magnetic reconnection theory of Sonnerup et al. (1981); $|\mathbf{J}|$ (nA m^{-2}) is the modulus of current density computed by the multi-spacecraft curlometer technique of Dunlop et al. (2002).
SOURCE: Chian and Muñoz (2011)

variance (SONNERUP; CAHILL JR., 1967). These three directions form an orthogonal LMN coordinate system. Considering a current sheet as a two–dimensional planar magnetic structure formed by two sets of oppositely directed field lines lying in a plane, L is then the direction of the field lines, M is the out–of–plane direction, and N is the direction perpendicular to L and M. A thin current sheet is formed between the two oppositely directed field lines, with the current flowing in the M direction. When the oppositely directed field lines reconnect, the current sheet bifurcates. Figure 2.13 shows three components of magnetic field (B_L, B_M, B_N) and ion velocity (V_L, V_M, V_N) in the LMN coordinates. For visualization we have shifted the plasma velocities in Figs. 2.12 and 2.13 by the average solar wind velocity, given by $\langle \mathbf{V}_{\mathrm{SW}} \rangle = (-926, 75, -29)$ km s^{-1} in the GSE coordinates.

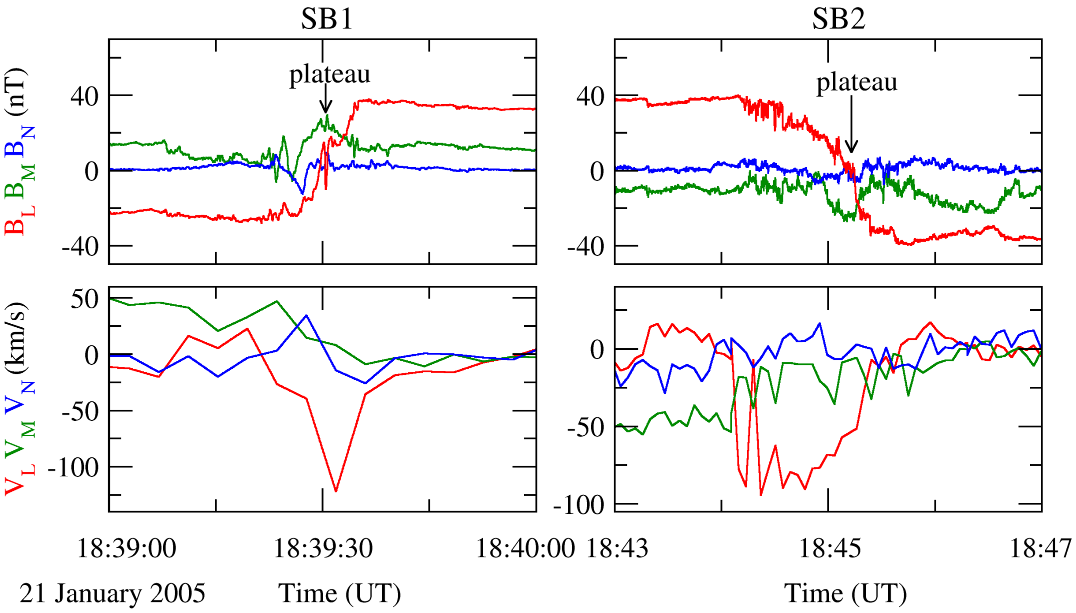

Figure 2.13 - B_L (red), B_M (green) and B_N (blue) are the components of $\mathbf{B}$ measured by Cluster–1 in the LMN coordinates; V_L (red), V_M (green) and V_N (blue) are the components of $\mathbf{V}$. This figure shows observational evidence of bifurcated current sheets SB1 and SB2, with a plateau at B_L in the middle of each bifurcated current sheet, and counter–propagating Alfvén waves at two edges of SB1 and SB2.
SOURCE: Chian and Muñoz (2011)

A signature of a bifurcated current sheet is the appearance of a "plateau" in B_L in the middle of a current sheet related to the region of the reconnection jet, as well as counter–propagating Alfvén waves evidenced by correlated/anti–correlated B_L and V_L at two edges of a current sheet (GOSLING et al., 2005; GOSLING et al., 2007; PHAN et al., 2006). This signature is readily seen in Figs. 2.12 and 2.13 for both SB1 and SB2. Each current sheet SB1 and SB2 is associated with a respective strong jet of ion flow $|\mathbf{V}|$ shown in the middle panels of Fig. 2.12, which flows mainly in the L direction as seen in the lower panels of Fig. 2.13, in agreement with the geometry of a magnetically reconnected current sheet. The observed jet velocity is close to the velocity predicted by the magnetic reconnection theory of Sonnerup et al. (1981), shown in the middle panels of Fig. 2.12. Figure 2.13 shows that V_L is anti–correlated (correlated) with B_L at the leading (trailing) boundary of the current sheet SB1, and V_L is correlated (anti–correlated) with B_L at the leading (trailing) boundary of

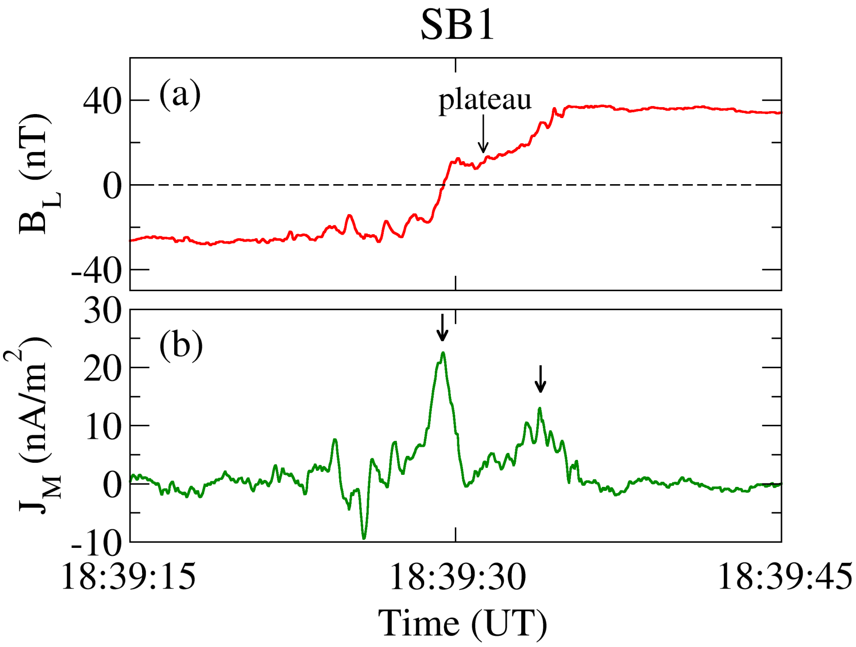

Figure 2.14 - Direct evidence of a bifurcated current sheet SB1 measured by Cluster-3. (a) Two–step temporal variation of B_L with a plateau in the middle of the current sheet. (b) J_M calculated from B_L showing double peaks at both edges of the current sheet.
SOURCE: Chian and Muñoz (2011)

the current sheet SB2. Such pairs of oppositely coupled changes in **V** and **B** are the signatures of counter–propagating Alfvén waves and provide observational support for magnetic reconnection exhausts in bifurcated current sheets in the solar wind (GOSLING et al., 2005; GOSLING et al., 2007; PHAN et al., 2006).

To further clarify the signature of a bifurcated current sheet, we plot in Fig. 2.14 B_L measured by Cluster–3, and J_M estimated from B_L near the plateau of SB1. By assuming time–stationarity and planarity of the current sheet, we compute J_M from a single spacecraft by the Ampere's Law, $J_M = (\Delta B_L/\Delta t)/(\mu_0 V_{\mathrm{CS}})$, where the spatial derivative is substituted by the temporal derivative using the Taylor's hypothesis and V_{CS} is the normal speed of the current sheet (MOZER et al., 2008). Figure 2.14(a) shows that the temporal variation of the reconnected component of magnetic field B_L occurs in two main steps which is an evidence that SB1 is bifurcated. Moreover, Fig. 2.14(b) shows two peaks (indicated by arrows) in the out–of–plane component of current density J_M, at two edges of SB1, demonstrating that the current sheet is bifurcated. Such direct evidence of a double–peak bifurcated current sheet has been obtained previously in association with magnetic reconnections in the Earth's magnetotail (HOSHINO et al., 1996) and in the magnetosheath of Earth's bow shock (RETINÒ et al., 2007). This is the first time such observation is demonstrated in an ICME.

3 INTERMITTENCY IN A MEAN–FIELD DYNAMO MODEL

In this Chapter, we study the deterministic and random chaotic dynamics of a mean–field dynamo model with α–quenching, originally proposed by Schmalz and Stix (1991). In particular, low–dimensional models derived from mean–field dynamo equations are useful to understand the underlying mechanism of observed signatures in solar and stellar magnetic activities (WEISS et al., 1984; MININNI et al., 2001). In this context, and considering that a low–dimensional mean–field modelling neglects the small–scale dynamics, the study of stochastic effects on such systems becomes relevant. The onset of the intermittency induced by noise is important to understand how stochastic perturbations can change the global dynamics of the system, and help to understand in a simpler manner relevant features of solar activity such as the Maunder–type minima (COVAS; TAVAKOL, 1997). Rempel et al. (2006) studied the effect of noise on nonlinear Alfvén waves in a regime with multistability, including coexistence of periodic attracting sets and a chaotic nonattracting set (chaotic saddle), showing that an external stochastic source can destroy attractors, as well as induce chaotic transients and extrinsic intermittency. Moreover, the effects of Gaussian and non–Gaussian noise were compared (REMPEL et al., 2008). Lai et al. (2003) proposed a general theoretical framework to analyze effects of additive noise on the nonlinear dynamical systems which contain chaotic saddles.

In previous chapter we study the relationship between coherent structures in a turbulent plasma and the magnetic reconnecion, a fundamental physical process associated with magnetic to kinetic energy conversion and heating. Turbulence is the typical nonlinear phenomena found in spatially–extended systems. Hereafter, we study the role played by nonlinear coherent structures in the dynamics of a number of spatially–extended systems, which are relevant for the space physics area, using the framework of the dynamical systems theory. In particular, the aim of this chapter is to introduce basic concepts of dynamical systems, and to apply these ideas to a nonlinear solar dynamo model.

3.1 Dynamical systems

Dynamical systems are usually described by a set of coupled ordinary differential equations:

$$\frac{d\mathbf{x}}{dt} = \mathbf{F}(\mathbf{x}, p), \tag{3.1}$$

where $\mathbf{F} = \{F_1, \ldots, F_N\}$ is a nonlinear vector function, $\mathbf{x}(t) = \{x_1(t), \ldots, x_N(t)\}$ is the vector characterizing the state of the system at time t and p represents a set of parameters. The vector space $\mathbb{R}^N$, where all the possible states $\mathbf{x}$ are represented, is called the phase space, and N is the dimension of the dynamical system. For a given initial condition $\mathbf{x}(t_0) = \mathbf{x}_0$, a solution $\mathbf{x}(t)$ of Eq. (3.1) is called trajectory, orbit or flux. The Poincaré surface of section, or Poincaré plane, is a $(N-1)$–dimensional plane in the phase space which is intersected by the trajectory in a particular direction. For example,

$$x_1 = \text{cte}, \qquad \frac{dx_1}{dt} > 0. \tag{3.2}$$

is a Poincaré surface with trajectories crossing in the bottom–up direction. Successive crossing points lying in the Poincaré plane define the Poincaré map. Using such map, the phase space dimension is reduced effectively by one, facilitating visualization and analysis.

The possible asymptotic solutions of system (3.1) are (i) fixed points, (ii) periodic orbits, also known as limit cycles, (iii) quasi–periodic orbits and (iv) chaotic orbits. A bifurcation of the dynamical system is a qualitative change of its dynamics produced by varying parameters p. Local bifurcations are related to the creation/destruction or changes in the stability of equilibrium or periodic solutions. For example, in a period doubling bifurcation, a preexisting stable periodic orbit of period n loses its stability, and a stable periodic orbit of period $2n$ is created. Bifurcations can be studied by using the bifurcation diagram, which can be constructed by fixing the control parameter and collecting a number of Poincaré points after discarding the transients, varying the parameter.

3.1.1 Lyapunov spectrum

The stability of the solutions of a dynamical system can be analyzed by mean of the Lyapunov exponents. For a typical trajectory $\mathbf{x}(t)$, the Lyapunov spectrum is

$$\lambda_i = \lim_{t\to\infty} \frac{1}{t} \ln \frac{|\delta \mathbf{x}_i(t)|}{|\delta \mathbf{x}_i(0)|}, \tag{3.3}$$

where $\{\delta\mathbf{x}_i(t)\}_{i=1}^{N}$ is a set of infinitesimal vectors evolving in the tangent space of the velocity field, as follows:

$$\frac{d\delta\mathbf{x}_i(t)}{dt} = \frac{\partial\mathbf{F}(\mathbf{x},p)}{\partial\mathbf{x}} \cdot \delta\mathbf{x}_i(t) \equiv \mathbf{DF}(\mathbf{x},p) \cdot \delta\mathbf{x}_i(t), \tag{3.4}$$

and $\mathbf{DF}(\mathbf{x},p)$ is the Jacobian matrix evaluated along the trajectory $\mathbf{x}(t)$. The Lyapunov exponents are the time–averaged stretching or contracting rates of infinitesimal vectors along a typical trajectory in the phase space. Performing the Gramm-Schmidt re–orthonormalization procedure described in Wolf et al. (1985), the exponents can be ordered, as follows: $\lambda_1 \geq \lambda_2 \cdots \geq \lambda_N$, where λ_1 is the largest Lyapunov exponent.

Computation of the Jacobian matrix of the flux is numerically unfeasible when the degree of freedom N is too large, such as for some spatially–extended systems. In that case, it is still possible to compute the largest Lyapunov exponent λ_1 using the method by Benettin et al. (1980). In this method, two trajectories $\mathbf{x}(t)$ and $\mathbf{x}(t)+\delta(t)$ are integrated from time t to $t+\Delta t$, and the local separation (or contraction) rate is obtained as

$$\lambda_t = \frac{1}{\Delta t}\ln\frac{|\delta(t+\Delta t)|}{|\delta(t)|}. \tag{3.5}$$

Performing the normalization $\delta(t+\Delta t) \mapsto \delta(t+\Delta t)|\delta(0)|/|\delta(t+\Delta t)|$, and repeating the integration M times, the maximum Lyapunov exponent is given by the average $\lambda_1 = \sum_{k=1}^{M}\lambda_{t_k}/M$. The second Lyapunov exponent can be obtained straightforwardly by integrating a third initial condition forming an orthogonal base with $\mathbf{x}$ and $\mathbf{x}+\delta$. A trajectory can be classified as temporally chaotic if at least the first Lyapunov exponent is positive, $\lambda_1 > 0$.

3.1.2 Numerical detection of chaotic saddles

Chaotic saddle are non–attracting chaotic sets responsible for chaotic transients and intermittency observed in many different applications (REMPEL et al., 2004b; REMPEL et al., 2004a; REMPEL; CHIAN, 2007; CHIAN et al., 2010). Because they are non–attracting, chaotic saddles cannot be studied by simply integrating equations forward in time. Here we review two methods used to detect chaotic saddles.

3.1.2.1 The sprinkler method

Consider a system with an attractor and a chaotic saddle CS coexisting in the phase space. A region R in the phase space containing only the chaotic saddle is called restraining region. The trajectories of all initial conditions in R will eventually leave R and converge to attractor A, except for initial conditions lying on the stable manifold of CS, which is a set of measure zero. Initial conditions close to the stable manifold are first attracted to CS and stay close to its neighborhood for some time, before they are repelled, following its unstable manifold. The closer an initial condition is to the stable manifold of CS, the longer it transient time before leaving R. These facts lead to the sprinkler algorithm to find chaotic saddles and their manifolds (KANTZ; GRASSBERGER, 1985; HSU et al., 1988). For each initial condition in a uniformly distributed grid in R the exit time T is computed, that is, the time it takes the condition to leave R. Those initial conditions with an exit time larger than some specified time T_c constitute an approximation to the stable manifold of CS, and their last iterations before leaving R approximate the unstable manifold. The points at some time $T_{CS} = \xi T_c$ are the approximation to the chaotic saddle. Usually T_c is chosen to be large compared to the average exit time $\bar{T}$ and $\xi = 1/2$.

3.1.2.2 The stagger–and–step method

Some applications, such as the computation of Lyapunov exponents, require a long trajectory. A method to find an arbitrarily long trajectory close to the chaotic saddle, called the stagger–and–step was introduced by Sweet et al. (2001). The method uses the same concepts of restraining region R and escape time T defined in the sprinkler method. The chaotic saddle is the collection of points $\mathbf{x}$ in R such that $T(\mathbf{x}) = \infty$. Hence, we look for initial conditions with escape time longer than some suitable threshold T^*. Let us start with an initial condition $\mathbf{x}_0$ with escape time $T(\mathbf{x}_0) = T_0 < T^*$. The escape time of the randomly perturbed initial condition $\mathbf{x}_0' = \mathbf{x}_0 + \mathbf{r}$ is computed until $T(\mathbf{x}_0') > T^*$. Then, $\mathbf{x}_0 + \mathbf{r}$ is evolved until the escape time of the current point $T(\mathbf{x}) < T^*$. This point is used as the new initial condition to iterate the process. The key point of the stagger–and–step method is the choice of the distribution of the random perturbation $\mathbf{r}$.Sweet et al. (2001) suggest using the "exponential stagger distribution", which is generated as follows. Let a be such that $10^{-a} = \delta$, with $\delta = |\mathbf{r}|$, and let $a_{\max}$ be the maximum value of a allowed by the machine's numerical precision. Generate a uniformly distributed random number s between a and $a_{\max}$. Choosing a random unit vector $\hat{\mathbf{r}}$, the perturbation vector is defined as $\mathbf{r} = 10^{-s}\hat{\mathbf{r}}$. In general, the threshold escape time T^* must be greater than the average escape time $\bar{T}$.

3.2 Mean–field $\alpha\Omega$ dynamo

Magnetic fields are ubiquitous in the universe. In many astrophysical bodies, the process by which this fields are amplified and sustained is the conversion of kinetic energy into magnetic energy, the so–called magnetic dynamo (BRANDENBURG; SUBRAMANIAN, 2005). In the case of the Sun, the kinetic energy comes from the plasma motion in the convection zone. Two large–scale effects are responsible for the main observational features in solar dynamo: the Ω and α effects. The Ω effect is the way an originally poloidal magnetic field is converted into toroidal magnetic field, due to the differential rotation of the Sun, which is stronger deep in the convection zone, at the tachocline (SOLANKI et al., 2006). The tachocline is the layer where the latitudinal differential rotation turns into rigid rotation, and coincide with the bottom of the convection zone (BRANDENBURG; SUBRAMANIAN, 2005). The resulting toroidal magnetic flux is carried out to the surface by convective motions and buoyancy. Convection and the Coriollis force due to rotation twist the magnetic lines, leading to the restitution of the poloidal magnetic field. The twisting of magnetic field lines due to turbulent convective motions and the Coriollis force is called the α effect.

The solar dynamo can be modelled by mean–field equations, where the fluctuations due to the turbulent velocity field of the convection zone appear only in the form of certain parameters. Schmalz and Stix (1991) proposed an $\alpha\Omega$ dynamo model for the solar dynamo, including an α–quenching effect, dimensionless partial differential equations are

$$\frac{\partial A}{\partial t} = \frac{\partial^2 A}{\partial x^2} + DB\cos x - CB, \tag{3.6}$$

$$\frac{\partial B}{\partial t} = \frac{\partial^2 B}{\partial x^2} + \frac{\partial A}{\partial x}, \tag{3.7}$$

$$\frac{\partial C}{\partial t} = \nu\frac{\partial^2 C}{\partial x^2} + AB, \tag{3.8}$$

where A and B are the normalized poloidal vector potential and toroidal magnetic field, respectively, and C is the normalized dynamic α coefficient (SCHMALZ; STIX, 1991). The are two control parameters: the ratio between the turbulent diffusivity and magnetic resistivity $\nu = \nu_t/\eta_t$, and the so–called dynamo number

$$D = \frac{\alpha_0 \omega_0 R^3}{\eta_t^2}, \tag{3.9}$$

where ω_0 is the angular velocity in the equator, R is the radius of the star and α_0 is a constant. The spatial variable x points in the poloidal direction, and the full range of latitude $0 \leq x \leq \pi$ is considered. At $x = 0$ and $x = \pi$ null boundary conditions are imposed

$$A(0) = A(\pi) = B(0) = B(\pi) = C(0) = C(\pi) = 0. \tag{3.10}$$

Boundary conditions are satisfied by the functions $\sin nx$. By using a spectral expansion of the form

$$A = \sum_{n=1}^{N} A_n(t) \sin nx, \tag{3.11}$$

$$B = \sum_{n=1}^{N} B_n(t) \sin nx, \tag{3.12}$$

$$C = \sum_{n=1}^{N} C_n(t) \sin nx, \tag{3.13}$$

the set of Eqs. (3.6)–(3.8) is transfomed into the form

$$\frac{dA_n}{dt} = -n^2 A_n + \frac{D}{2}(B_{n-1} + B_{n+1}) + \sum_{j=1}^{N}\sum_{k=1}^{N} F_{njk} B_j C_k + \sigma \xi_{A_n}(t), \tag{3.14}$$

$$\frac{dB_n}{dt} = -n^2 B_n + \sum_{j=1}^{N} G_{nj} A_j + \sigma \xi_{B_n}(t), \tag{3.15}$$

$$\frac{dC_n}{dt} = -\nu n^2 C_n - \sum_{j=1}^{N}\sum_{k=1}^{N} F_{njk} A_j B_k + \sigma \xi_{C_n}(t), \tag{3.16}$$

where

$$F_{njk} = \frac{8njk}{\pi(n+j+k)(n+j-k)(n-j+k)(n-j-k)}, \tag{3.17}$$

if $n + j + k$ is odd and $F_{njk} = 0$ otherwise and

$$G_{nj} = \frac{4nj}{\pi(n^2 - j^2)}, \tag{3.18}$$

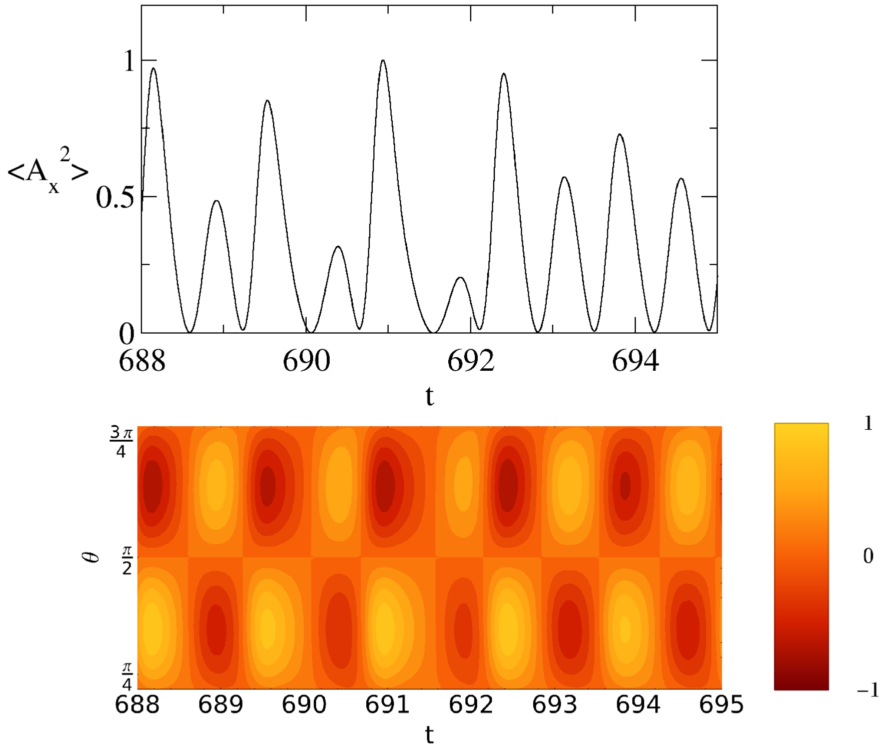

Figure 3.1 - Typical solution of the mean–field dynamo model of Eqs. (3.14)–(3.16) for $D = 205$, $\nu = 0.5$ and $\sigma = 0$. Upper panel: Temporal evolution of the averaged poloidal magnetic energy. Lower panel: Saptio–temporal pattern of the poloidal magnetic field. The vertical axis represents the latitude, with $\theta = \pi/2$ being the equator.

if $n + j$ is odd and $G_{nj} = 0$ otherwise. A_n and B_n are the spectral amplitudes of the poloidal and the toroidal components of the mean magnetic field, and C_n is the spectral amplitude of the dynamical α–quenching (SCHMALZ; STIX, 1991; COVAS; TAVAKOL, 1997). We have introduced additive noise to the system. The variables $\xi_A(t)$, $\xi_B(t)$ and $\xi_C(t)$ are vectors whose components are Gaussian random variables of zero mean and unit variance. The control parameters are the noise amplitude σ and the dynamo number D. The ratio between turbulent diffusivity and magnetic resistivity is fixed to $\nu = 0.5$. By choosing the truncation order $N = 4$, and limiting our study to the antisymmetric subspace of solutions, as in Covas and Tavakol (1997), Eqs. (3.14)–(3.16) reduce to a six–dimensional dynamical system. Note that when $N = 1$ Eqs. (3.14)–(3.16) reduce to the Lorenz system (LORENZ, 1963). For $N > 4$ the dynamical properties of the resulting set of equations remain essentially the same.

We solve Eqs. (3.14)–(3.16) using a fourth–order Runge–Kutta scheme with a fixed time step $\Delta t = 0.01$. A typical solution of the mean–field dynamo model, for $D = 205$, $\nu = 0.5$ and $\sigma = 0$, is shown in Fig. 3.1. The upper panel shows the time series of the averaged poloidal magnetic energy $(\partial_x A)^2$ and the lower panel is a densityplot of the poloidal magnetic field. Both quantities are normalized to facilitate visualization. Although rather simple, this $\alpha\Omega$ mean–field dynamo model shows a behavior similar to that observed in the solar dynamo. The time series of the poloidal magnetic field is cyclic, with maxima and minima of activity. Moreover, the maxima of magnetic activity do not have constant amplitude, with some cycles with lower activity. The spatiotemporal behavior of the poloidal magnetic field shows opposite polarities in both hemispheres and periodic reversals from cycle to cycle. Cycles, minima of activity and polarity reversals are all features which have been observed in the Sun and other stars with magnetic activity (SOON et al., 1993; HOYT; SCHATTEN, 1997; TOBIAS, 2002).

3.3 Bifurcation diagram

First, let us consider a deterministic dynamo in the absence of noise ($\sigma = 0$) by constructing a bifurcation diagram from the numerical solutions of Eqs. (3.14)–(3.16), varying the dynamo number D. The Poincaré plane is chosen as A_1=0 and $\dot{A}_1 < 0$. For each value of D, we perform 500 iterations of the Poincaré map, discarding the transients and keeping the last 300 points. Figure 3.2 shows the resulting bifurcation diagram, where we plot variable C_2 of the Poincaré points as a function of D. The black line from the left denotes a period–1 periodic orbit. At $D \approx 179.7$ this periodic orbit suffers a pitchfork bifurcation (PB), and loses its stability. In that moment two period–1 periodic orbits are created, denoted by red and blue lines. These new periodic attractors undergo a period doubling bifurcation at $D \approx 197.4$. Both attractors become chaotic through an infinite succession of period doubling bifurcations, also known as period doubling cascade, an universal route to chaos (FEIGENBAUM, 1979). These two chaotic attractors merge into one larger attractor at $D \approx 204.3$, in a global bifurcation known as merging crisis. Within the chaotic interval denoted by black dots in Fig. 3.2 there are subintervals where the system is periodic. We will focus in one periodic window (PW) near $D = 206$. The interval spanned by this periodic window is too small to be seen in Fig. 3.2.

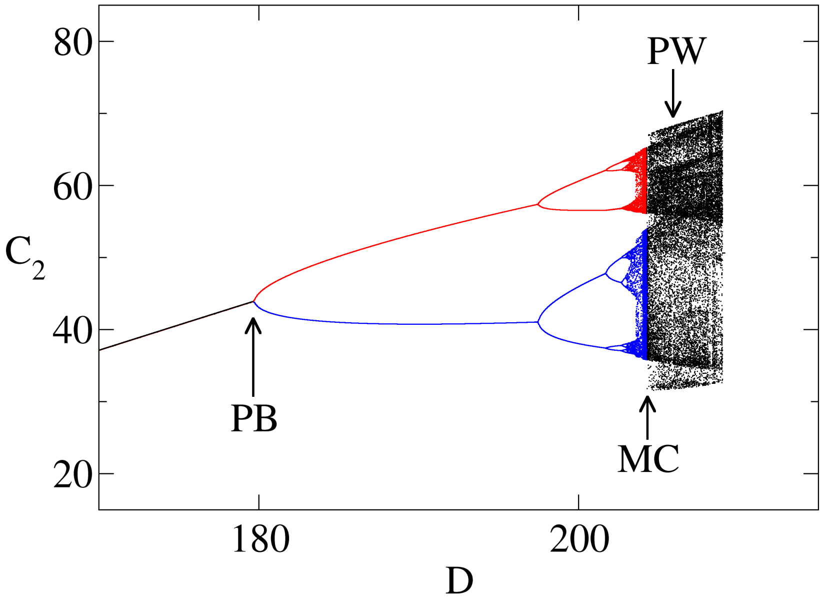

Figure 3.2 - Bifurcation diagram of Eqs. (3.14)–(3.16) using as control parameter the dynamo number D. PB denotes the pitchfork bifurcation where a periodic attractor (black) loses its stability and two new periodic attractors (blue and red) arises. These two attractors become chaotic through a cascade of period doubling bifurcations. MC denotes the merging crisis, when the attractors merge one to each other to form a single chaotic attractor. PW indicates a periodic windows embedded in the chaotic region.

3.3.1 Periodic window

A periodic window is a region of the parameter space where an interval containing stable periodic solutions is surrounded by chaos. Even though the attracting solutions within a periodic window are not chaotic, trajectories typically display chaotic transients before they converge to the periodic attractors. Hence, a chaotic saddle, a non attracting chaotic set responsible for chaotic transients, is expected within a periodic window.

In figure 3.3(a) a periodic window of the system is shown, where both the attractor (black) and the surrounding chaotic saddle (SCS, green) are plotted. This periodic window begins at $D_{\rm SNB} \sim 205.901$ where a pair of stable and unstable periodic orbits of period–13 are created by a saddle–node bifurcation (SNB), and ends at $D_{\rm IC} \sim 205.852305$ where an interior crisis takes place. The two largest Lyapunov exponents of the attractor (black and red) are plotted in 3.3(b). The period–13

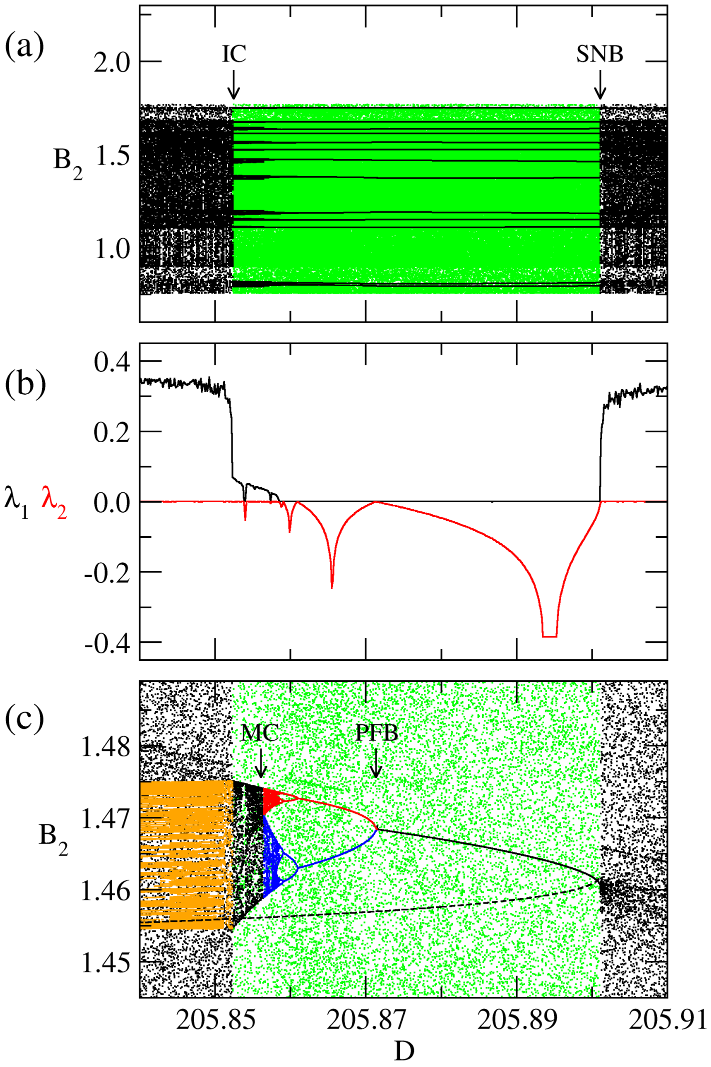

Figure 3.3 - (a) Periodic window of the bifurcation diagram, where both the attractor (black) and the surrounding chaotic saddle (green) are plotted. (b) The two largest Lyapunov exponents of the attractor (black and red). (c) Enlargement of one of the thirteen branches of (a).

stable periodic orbit evolves to a banded chaotic attractor (BCA) via a cascade of period doubling bifurcations. An enlargement of one of the thirteen branches of the attractor is plotted in 3.3(c). Two bifurcations are indicated by arrows. A pitch–fork bifurcation (PFB) at $D_{\mathrm{PFB}} \sim 205.872$, where two coexisting attractors (blue and red) are born, and an attractor–merging crisis (MC) at $D_{\mathrm{MC}} \sim 205.856$ involving the merging of two coexisting attractors, forming a single attractor (black). The surrounding chaotic saddle (green) is robust and persists after the interior crisis. At

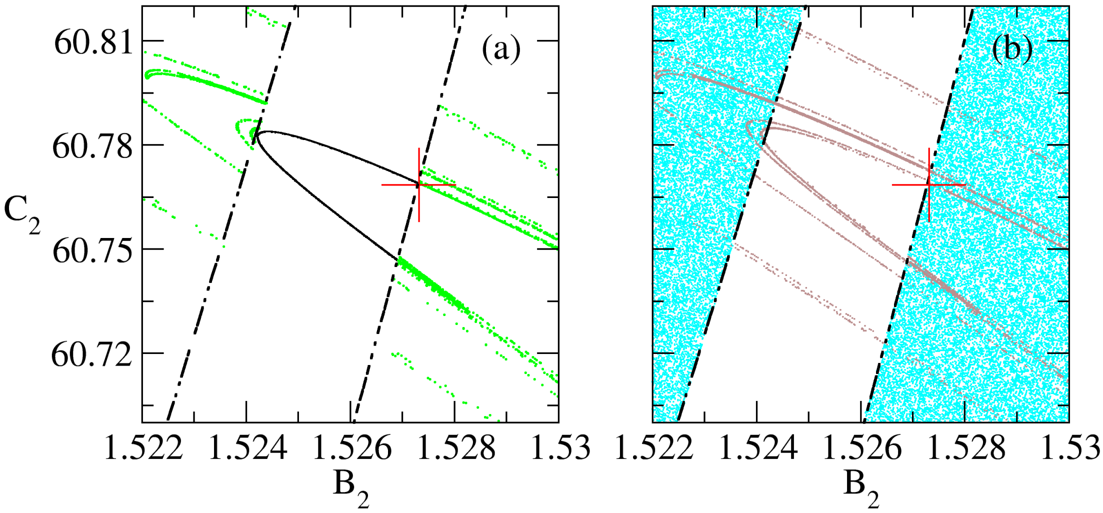

Figure 3.4 - The characterization of IC due to a chaotic attractor–chaotic saddle collision at the end of the periodic window. (a) The BCA (black), the SCS (green), one Poincaré point of the period–13 mediating UPO (cross) and its stable manifold (dashed line). (b) Stable (light blue) and unstable (brown) manifolds of the SCS.

the onset of the interior crisis, the banded chaotic attractor loses its stability due to a global bifurcation and is converted into a banded chaotic saddle (BCS) (orange).

3.4 Interior crisis

An interior crisis is characterized by a sudden enlargement of a chaotic attractor as a parameter is varied, and it is a common feature of periodic windows. The collision of a mediating unstable periodic orbit and its stable manifold with the chaotic attractor is responsible for this chaotic transition (GREBOGI et al., 1983b). Furthermore, it was demonstrated by Rempel et al. (2004b) that a surrounding chaotic saddle and its stable manifold also collide with the attractor. This important fact can be used to characterize the collision.

The characterization of an interior crisis due to the collision described above at the end of the periodic window of Fig. 3.3 is shown in Fig. 3.4(a). Only one of thirteen branches of the banded chaotic attractor BCA (black solid line) and only one of thirteen Poincaré points of the period–13 mediating unstable period orbit (cross) are plotted. At crisis $D = D_{\mathrm{IC}}$, BCA collides head–on with the surrounding chaotic saddle SCS (green) as well as the mediating unstable periodic orbit of period–13

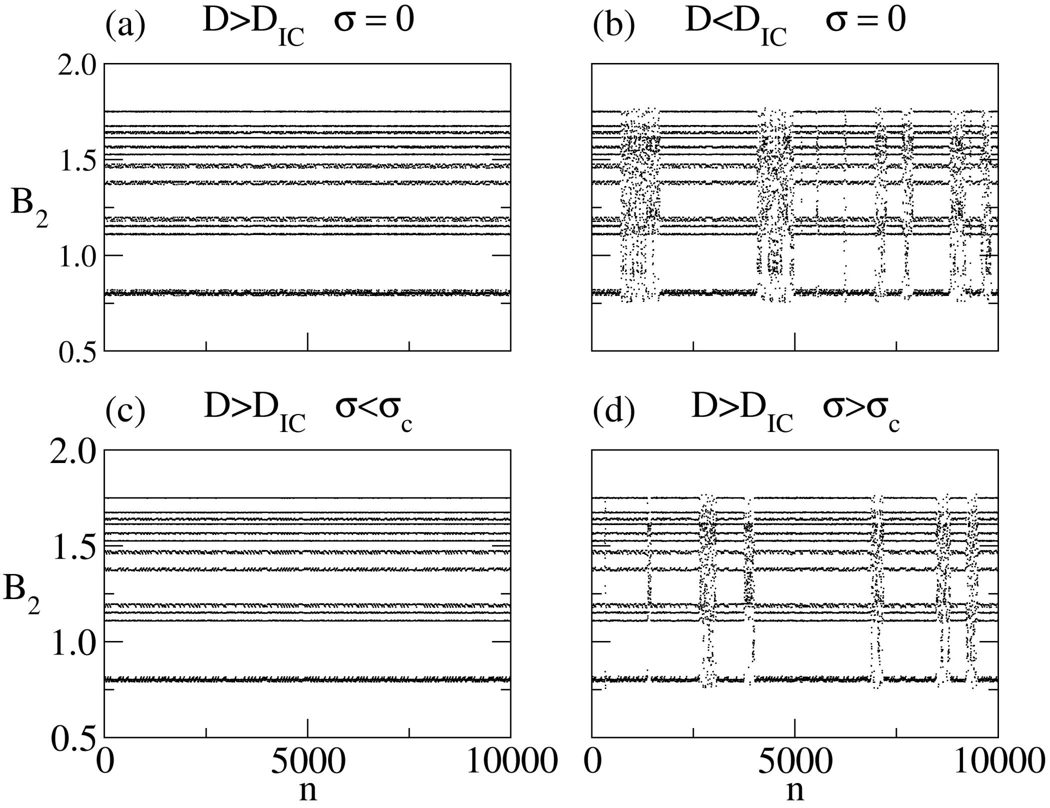

Figure 3.5 - (a) A Poincaré map time series of the banded chaotic attractor (BCA) at $D = 205.8525 > D_{\mathrm{IC}}$, before the interior crisis. (b) The time series of crisis-induced intermittency corresponding to the post-crisis chaotic attractor. (c) Time series of the random attractor for a small noise amplitude $\sigma = 10^{-3.5}$. The trajectory traverses the vicinity of BCA. (d) For a larger value of the noise amplitude, $\sigma = 10^{-3}$, the time series of the random chaotic attractor shows evidence of noise–induced intermittency.

and its invariant stable manifold (dashed line). The mediating orbit is created by the saddle–node bifurcation at $D = D_{\mathrm{SNB}}$, as demonstrated in Fig. 3.3(c). The surrounding chaotic saddle is formed by the intersection of its stable (light blue) and unstable (brown) manifolds, shown in Fig. 3.4(b), which exhibits gap regions typical of non–attracting chaotic sets. Note that the stable manifold of the mediating unstable periodic orbit (dashed line) of Fig. 3.4(a) coincides with the edge of the stable manifold of the surrounding chaotic saddle of Fig. 3.4(b).

Now we discuss crisis–induced intermittency. A time series of Poincaré map of the BCA at $D = 205.8525 > D_{\mathrm{IC}}$, before the interior crisis, is plotted in Fig. 3.5(a), and its corresponding two dimensional projection is plotted in Fig. 3.6(a). After the

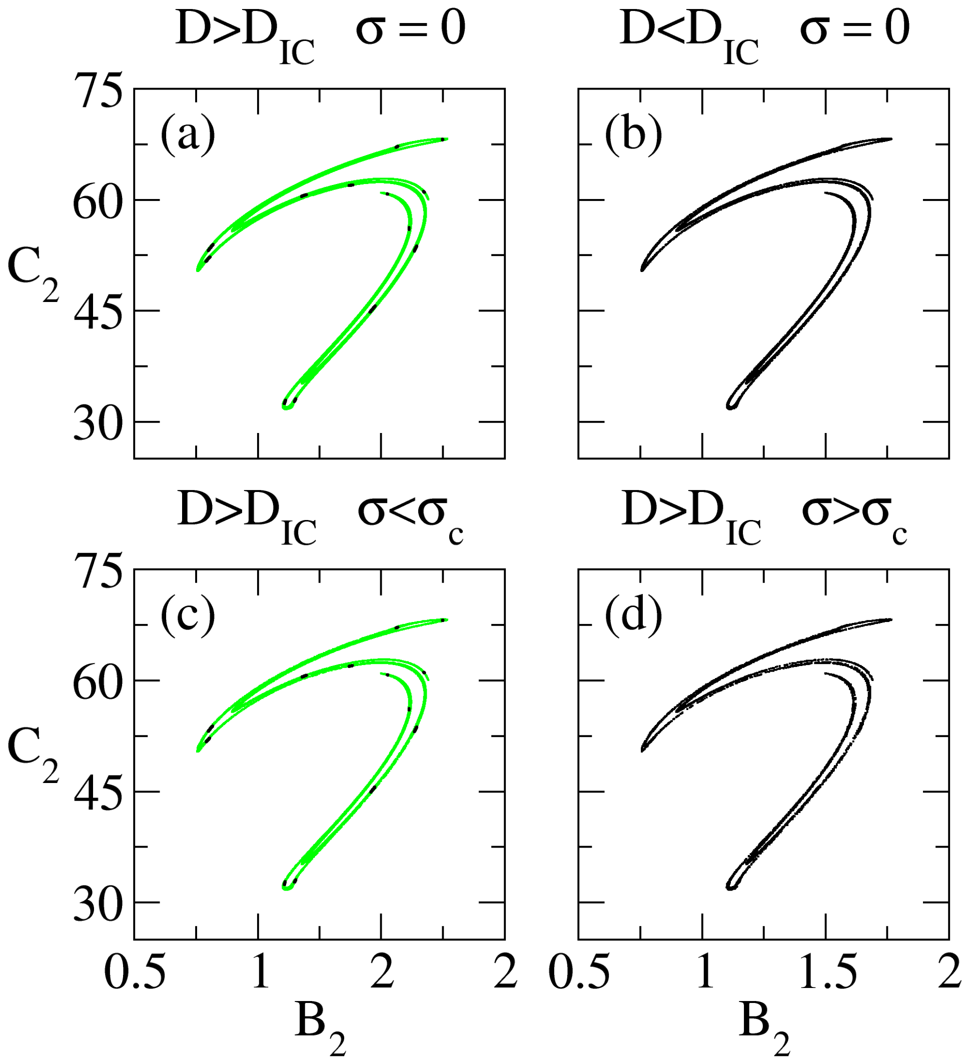

Figure 3.6 - Two dimensional Poincaré maps corresponding to the cases of Fig. 3.5. The random chaotic attractors (black) in (c) and (d) have similar features as the deterministic chaotic attractors of (a) and (b), respectively. Figures (a) and (c) show the SCS in the deterministic and stochastic cases, respectively (green).

onset of the interior crisis, coupling unstable periodic orbits are created at the gap regions of the SCS and BCS via an explosion of chaotic sets (ROBERT et al., 2000) and topological gap filling (SZABÓ et al., 2000) which couple two chaotic saddles, leading to the formation of a large chaotic attractor shown in Fig. 3.6(b). The time series of crisis–induced intermittency corresponding to the post–crisis chaotic attractor of Fig. 3.6(b) is shown in Fig. 3.5(b). We distinguish two kinds of behavior in the time series. The banded or "laminar" periods correspond to the trajectory visiting the vicinity of BCS, and the surrounding or "bursty" periods occurs when the trajectory visits the vicinity of SCS. This is a direct consequence of the coupling between two chaotic saddles BCS and SCS after the interior crisis. An importance of intermittent behavior is found in nonlinear dynamo models is in understanding the mechanism of production of the so–called grand or Maunder–type minima in solar and stellar activity, during which the amplitude of the stellar cycle is greatly diminished (COVAS; TAVAKOL, 1997).

3.5 Noise–induced intermittency

In the previous section we discussed the typical phase space landscape during an interior crisis in the border of a periodic window of the mean–field dynamo model. We have shown the dynamical mechanism responsible for the interior crisis, as well as the intermittency resulting from the coupling of two chaotic saddles BCS and SCS. In this section we fix the parameter D before the interior crisis to study the system under the influence of additive noise. The theoretical framework to study the role of additive noise in nonlinear dynamical systems was developed by Lai et al. (2003). It was shown that the key mechanism for the onset of noise–induced unstable dimension variability, transition to chaos and intermittency in stochastic differential equations, is the presence of a chaotic saddle in the originally deterministic system.

The stochastic differential equations (3.14)–(3.16) with $\sigma > 0$ are solved using the standard Heun's method (KLOEDEN; PLATEN, 1992), which is a second–order predictor–corrector method. We fix parameters $D = 205.8525 > D_{\mathrm{IC}}$, just before the interior crisis, using the noise amplitude σ as control parameter. The Poincaré map time series of the random attractor for a small noise amplitude $\sigma = 10^{-3.5}$ is shown in Fig. 3.5(c). Comparing with the deterministic case in Fig. 3.5(a), we see that for $\sigma = 10^{-3.5}$ the random attractor trajectory traverses the vicinity of the deterministic banded chaotic attractor BCA. Encreasing only slightly the noise amplitude to $\sigma = 10^{-3}$, the time series of the random attractor shows evidence of noise–induced intermittency, with "laminar" periods intermingled with "bursty" periods, similar to that observed for the crisis–induced intermittency.

Lai et al. (2003) proposed an explanation for the phenomena of noise–induced intermittency within periodic windows. The external additive noise induces the interaction between the random attractor and the chaotic saddle, changing the dynamical properties of the trajectories. This process depends on the amplitude of noise, as

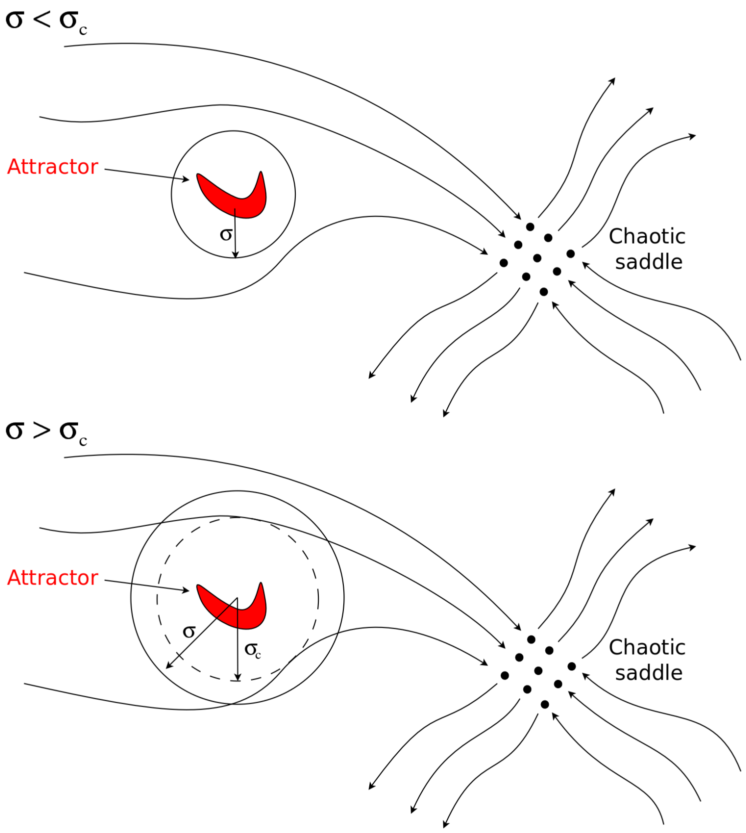

Figure 3.7 - Schematical representation of transition to chaos and noise–induced intermittency in a stochastical dynamical system.

suggested by Fig. 3.5(c) and (d). Hence, a crisis–like chaotic transition is expected. The schematical representation of such a transition is shown in Fig. 3.7. The upper panel of Fig. 3.7 shows the typical configuration of the phase space before the transiton, for $\sigma < \sigma_\mathrm{c}$. A random attractor (red area plus the circle) coexists with a chaotic saddle (black dots) and its stable and unstable manifolds, represented by lines. The additive noise creates a sphere of influence around the old deterministic attractor (red) called the noisy basin of the attractor. There is no overlap between the stable manifold of the chaotic saddle, denoted by lines entering the black dots, and the noisy basin. In this case, a random initial condition leads to a trajectory confined in the vicinity of the deterministic attractor, although there can be transient chaos initially, in the sense that the trajectory may move toward the chaotic saddle along its stable manifold, wander near the saddle for a finite amount of time, and leave it along its unstable manifold. At $\sigma \approx \sigma_\mathrm{c}$, the noisy basin "touches" the stable manifold of the chaotic saddle. For $\sigma > \sigma_\mathrm{c}$, a subset of the stable manifold of the chaotic saddle is located in the noisy basin, as shown in the lower panel of Fig.

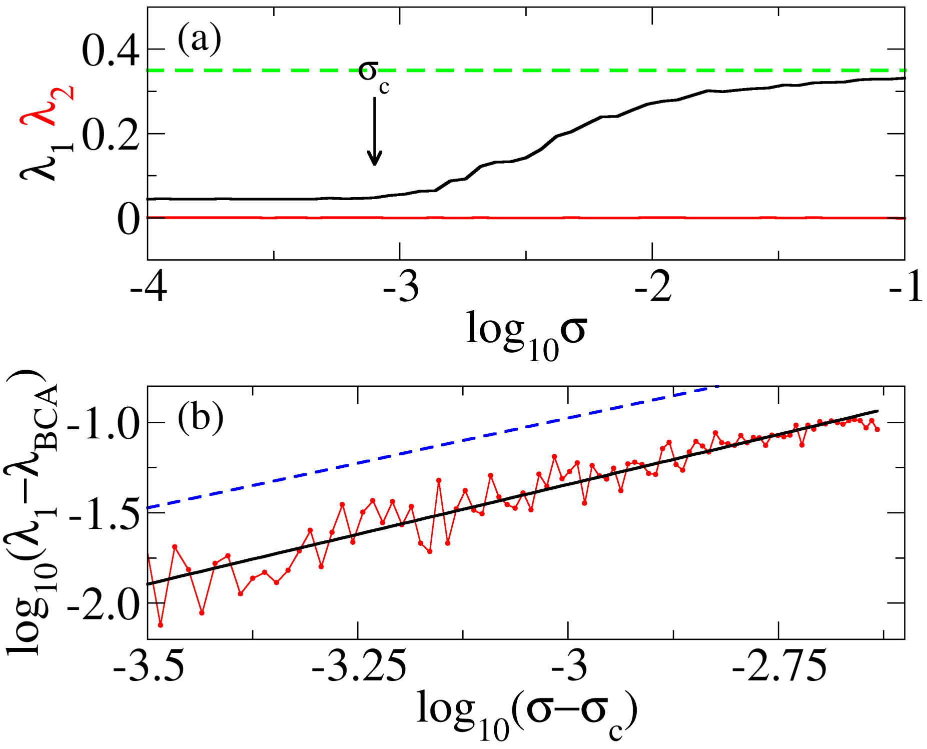

Figure 3.8 - (a) First two Lyapunov exponents of the random chaotic attractor as a function of the noise amplitude, near the transition to a more chaotic state $D = 205.8525$. (b) The scaling of the first Lyapunov exponent of the random chaotic attractor for $\sigma \gtrsim \sigma_c$.

3.7. As a result, there is a nonzero probability that a trajectory near the attractor is kicked out of the noisy basin and moves toward the chaotic saddle along its stable manifold. Because the chaotic saddle is nonattracting, the trajectory can stay in its vicinity for only a finite amount of time before leaving along its unstable manifold and then, enter the noisy basin again, and so on. Thus, the intermittent behavior observed for $\sigma \gtrsim \sigma_c$ is explained as a noise–induced coupling between the noisy basin of the attractor and the chaotic saddle.

Transition to noise–induced intermittency can be studied by examining the dynamical properties of the random attractor characterized by the Lyapunov exponents. The upper panel of Fig. 3.8 shows the first two Lyapunov exponents of the random chaotic attractor as a function of the noise amplitude, indicating the critical noise amplitude $\sigma_c \approx 10^{-3.1}$, above which λ_1 of the random chaotic attractor exceeds λ_1 of the deterministic BCA and increases monotonically until it approaches λ_{SCS} of the surrounding chaotic saddle (dashed green line).

Lai et al. (2003) have shown that for $\sigma \gtrsim \sigma_\mathrm{c}$, the first Lyapunov exponent λ_1 of the random chaotic attractor scales as

$$(\lambda_1 - \lambda_\mathrm{BCA}) \sim (\sigma - \sigma_\mathrm{c})^\alpha, \tag{3.19}$$

with the scalling exponent given by

$$\alpha = 1 - \frac{1}{(\tau \lambda_\mathrm{SCS})}, \tag{3.20}$$

where τ is the average exit time of the SCS from the restraining region. The scaling of the first Lyapunov exponent λ_1 of the random chaotic attractor for $\sigma \gtrsim \sigma_\mathrm{c}$ is shown in the lower panel of Fig. 3.8, where λ_BCA refers to the λ_1 of the deterministic banded chaotic attractor. The black line is the linear fit of the data, with a a slope of 1.104 ± 0.04. In this case, $\tau \approx 362$ and $\lambda_\mathrm{SCS} \approx 0.345$, giving a theoretical scalling exponent $\alpha = 0.992$, represented by the dashed blue line. The observed scalling exponent is in good agreement with the theory.

4 EDGE STATE AND CRISIS IN THE PIERCE DIODE

In Chapter 3 we introduced the basic concepts of dynamical systems and applied them to study a model of solar dynamo in the presence of additive noise. That set of six differential equations is a low–dimensional problem, even though this model arises from a spatially–extended system. Now, we study a physical system where a much larger number of degrees of freedom is considered.

In this chapter we study the chaotic dynamics in the Pierce diode, a simple spatially–extended system for collisionless bounded plasmas, focusing on the concept of edge of chaos, the boundary that separates transient from asymptotic dynamics. We fully characterize an interior crisis at the end of a periodic window, thereby showing direct evidence of the collision between a chaotic attractor, a chaotic saddle and the edge of chaos, formed by a period–3 unstable periodic orbit and its stable manifold. The edge of chaos persists after the transition from weak to strong chaos.

4.1 Edge of chaos

In a dynamical system, the basin of attraction of a given attractor is the set of initial conditions which converge to that attractor. If the system has more than one attractor, we can define a subset that separates the basins: the boundary of basins. An extension of this concept was introduced by Skufca et al. (2006) while studying transition to turbulence in shear flows using a nine–dimensional truncation of the Navier–Stokes equation. In that model, the system has one attractor, coexisting with a chaotic saddle, the structure responsible for the chaotic transients (REMPEL et al., 2004a; REMPEL; CHIAN, 2007; REMPEL et al., 2010). Skufca et al. (2006) observed that, even though only one basin of attraction is present, the phase space can be divided into two regions, depending on whether an initial condition displays a chaotic transient behavior or not. The boundary between these two regions is called the edge of chaos. In the last years, the dynamical properties of the edge of chaos have been studied in a wide variety of applications, such as direct numerical simulations of pipe flow (SCHNEIDER et al., 2007), a numerical MHD simulation for two–dimensional magnetic reconnection (CASSAK et al., 2007), and a generic two–dimensional map (VOLLMER et al., 2009). These works illustrate the rich dynamical behavior of the edge of chaos and its important role in transitions to chaos and turbulence.

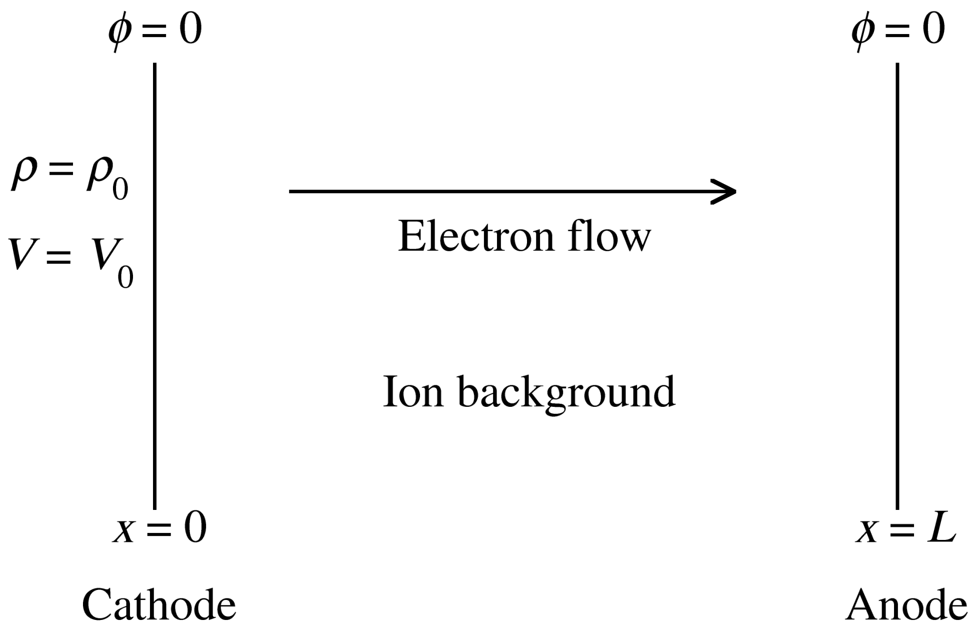

Figure 4.1 - Schemtaic diagram of the Pierce diode.

4.2 Pierce diode

In this Chapter we apply ideas of Section 4.1 to the Pierce diode, a one–dimensional spatially–extended plasma model. Constituting the simplest model for collisionless bounded plasma systems, the classical Pierce diode (LAWSON, 1989) is a one–dimensional electrostatic parallel–plane diode with gap spacing L into which a monoenergetic electron beam at constant velocity v_0 and charge density ρ_0 is injected. An immobile neutralizing ion background with density ρ_0 is present between the planar electrodes held at the same potential (short–circuit condition). Figure 4.1 is a schematic representation of this system. In particular, the presence of a controlled amount of background ions inside microwave tubes allows plasma–filled devices to operate at currents much higher than the maximum current for vacuum tubes, thereby increasing significantly the power handling capabilities of microwave tubes. From the emitter (at $x = 0$), the monoenergetic electron beam, after crossing the gap spacing between the plates, is completely absorbed by the collector at $x = L$. Although rather simple, this distributed model exhibits many features of the electron beam dynamics in a variety of microwave electronic devices such as the klystron and the virtual cathode oscillator (TRUBETSKOV et al., 1996). In addition, this model is used for studying the stability of electron flows in plasma–filled diodes and charge neutralized ion beam transport for inertial confinement fusion (BARROSO et al., 2001), and also space physics applications such as double layers in the magnetospheric cusp (TREUMANN; BAUMJOHANN, 1997). A biparametric version of the model (TERRA, 2011) and helix travelling–waves (DATTA et al., 2011) have been investigated recently, showing the Pierce as a still interesting problem to study.

The system is characterized by the single control parameter $\alpha = \omega_p L/v_0$, often referred to as the Pierce parameter, where $\omega_p = \sqrt{\rho_0 e/\epsilon_0 m_e}$, denotes the plasma frequency of the electron beam, with ϵ_0 the vacuum permittivity, and e and m_e the electronic charge and the electron mass respectively. The electron flow in this system can be described by the cold fluid equations, namely, continuity, momentum and the Poisson's equations

$$\frac{\partial \rho}{\partial t} + \frac{\partial (\rho v)}{\partial x} = 0, \tag{4.1}$$

$$\frac{\partial v}{\partial t} + v\frac{\partial v}{\partial x} = \frac{\partial \phi}{\partial x}, \tag{4.2}$$

$$\frac{\partial^2 \phi}{\partial x^2} = \alpha^2(\rho - 1), \tag{4.3}$$

where ρ is the mass density, v is the electron flow velocity and ϕ is the electric potential. In Eqs. (4.1)–(4.3) dimensionless variables (density ρ, velocity v, electric potential ϕ, space coordinate x and time t) are used (HRAMOV et al., 2006). They are related to the corresponding dimensional variables as follows:

$$\rho' = \rho_0\rho, \quad v' = v_0 v, \quad \phi' = (m_e v_0^2/e)\phi,$$

$$x' = Lx, \quad t' = (L/v_0)t, \tag{4.4}$$

where the symbols denoted by a prime correspond to the dimensional values. Using this normalization scheme, the boundary conditions of system (4.1)–(4.3) read as $\rho(0,t) = 1$, $v(0,t) = 1$ and $\phi(0,t) = \phi(1,t) = 0$. A linear approximation analysis (PIERCE, 1944; LAWSON, 1989) can be performed on the assumption of solutions of the form $\rho(x,t) = \rho_0 + \rho_1(x,t)$ and $v(x,t) = v_0 + v_1(x,t)$, where time and spatial dependence of $\rho_1(x,t)$ and $v_1(x,t)$ are respectively of the form $\exp(-i\omega t)$ and $\exp(ikx)$. Substituting these ansatz solutions in Eqs. (4.1)–(4.3) and taking just leading terms,

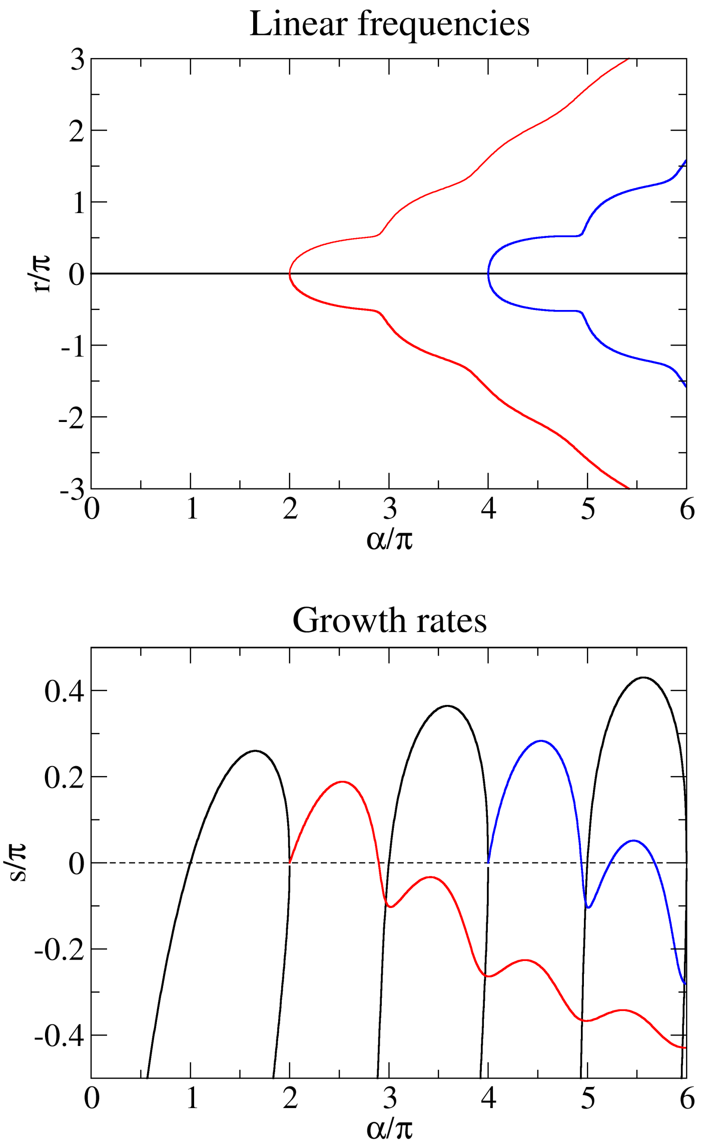

Figure 4.2 - Numerical solutions of the Pierce diode linear dispersion relation Eq. (4.5). Black lines represent nonoscillatory solutions, and red and blue lines represent oscillatory solutions. Upper panel: linear frequencies. Lower panel: growth rates.

we obtain the a linear dispersion relation given by (PIERCE, 1944; MATSUMOTO et al., 1996)

$$2\omega^2(\omega^2-\alpha^2)+i\alpha\{(\omega+\alpha)^2[e^{i(\omega-\alpha)}-1]-(\omega-\alpha)^2[e^{i(\omega+\alpha)}-1]\}=0, \qquad (4.5)$$

where ω as a complex frequency

$$\omega = r + is. \tag{4.6}$$

The derivation of linear dispersion (4.5) is given in Appendix A. Figure 4.2 shows numerical solutions of (4.5), normalized by π. Linear frequencies, given by the real part of Ω, are plotted as a function of α/π in the upper panel of Fig. 4.2. Imaginary part of Ω gives the linear growth rates, shown in the lower panel of Fig. 4.2. Black lines indicate non–oscillatory solutions, while red and blue indicate oscillatory solutions. Dispertion relation (4.5) provides time growing (unstable) non–oscillatory solutions for $(2n-1)\pi \leq \alpha \leq 2\pi n$, $(n = 1, 2, 3, \dots)$, growing (unstable) oscillatory solutions for $2\pi n \leq \alpha \leq (2n + 1 - \epsilon_n)\pi$, and damped (stable) oscillatory solutions for $(2n - 1 - \epsilon_n)\pi \leq \alpha \leq (2n - 1)\pi$, where $0 < \epsilon_n \ll 1$ varies slightly with n. Thus the stability character of linear oscillatory solutions alternates as the parameter α is increased by π. Then an otherwise single damped mode starts growing at $\alpha = \pi$ and remains unstable until $\alpha = 2\pi$, a situation in which a virtual cathode is formed with electrons being reflected back to the emitter. Moreover, the transition from instability to stability just below each odd multiple of π is due to a Hopf bifurcation (LAWSON, 1989).

4.3 Bifurcation diagram

We solve the continuity and momentum equations (4.1)–(4.3) using a first–order backward difference scheme in space and a second–order implicit scheme in time, over a spatial grid with $N = 512$ points. In order to satisfy the zero–potential conditions, the Poisson's equation is solved by means of the sine fast Fourier transform method (MATSUMOTO et al., 1996). The state of the system at each discrete time t_k is given by $\rho_i^k = \rho(x_i, t_k)$ and $v_i^k = v(x_i, t_k)$, where x_i is a grid point. We define a Poincaré map as $\rho(x = L/4, t) = 1$ and $\partial_t \rho(x = L/4, t) < 0$ to construct a bifurcation diagram by varying the parameter α. For every value of α, we discard the initial transient (100 iterations) and plot the next 200 iterations of the map. We are interested in a periodic window of period–3 (p–3) near $\alpha = 3\pi$. Figure 4.3(a) shows the bifurcation diagram of this periodic window, and Fig. 4.3(b) the first and second Lyapunov exponents of the attractor computed using the technique described in Benettin et al. (1980). Three types of bifurcation that characterize the periodic window, as was shown in Chapter 3, are noteworthy: a saddle–node bifurcation (SNB) at $\alpha \approx 2.85584\,\pi$, where a splitting pair of p–3 stable and unstable periodic orbits arises; a period–

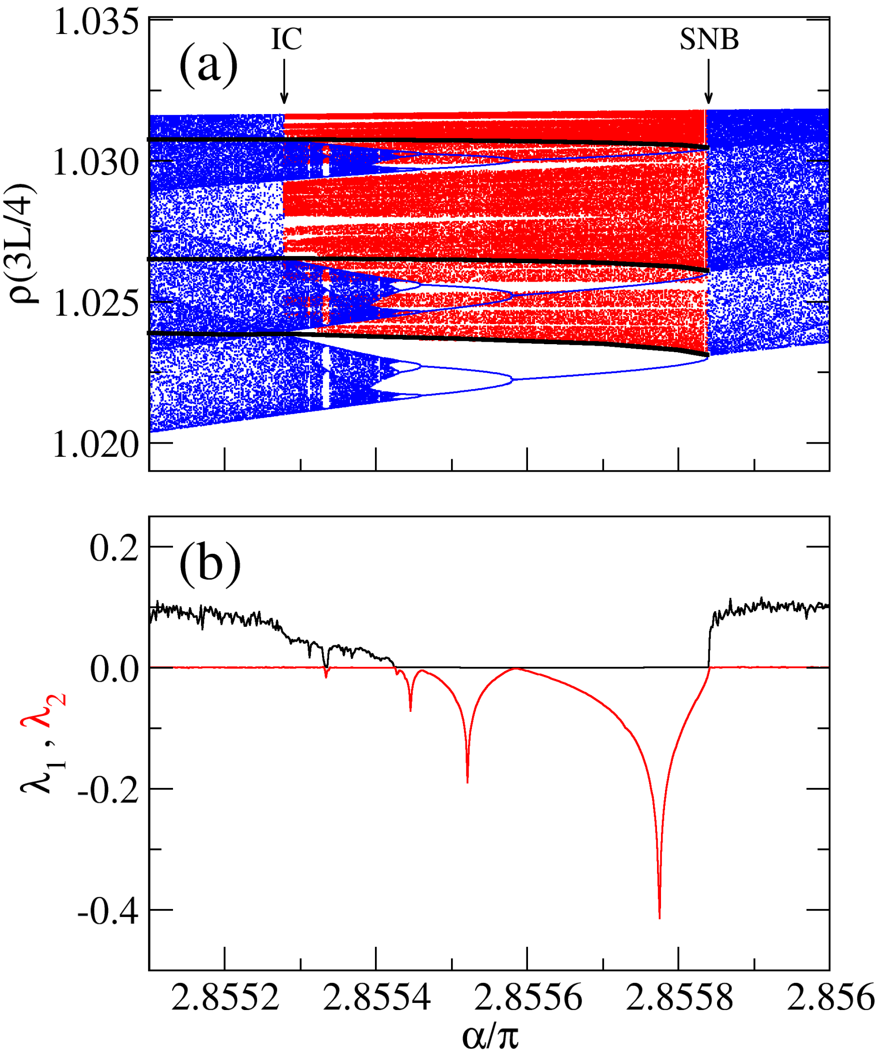

Figure 4.3 - (a) Bifurcation diagram: a p–3 periodic window in the Pierce diode. Within the window the attractor (blue dots) coexists with the surrounding chaotic saddle (red dots) and a p–3 UPO (black lines). SNB (IC) denotes saddle–node bifurcation (interior crisis). (b) First (black) and second (red) Lyapunov exponents.

doubling cascade leading to a banded chaotic attractor (BCA); and an interior crisis (IC) at $\alpha = \alpha_C \approx 2.8552792\,\pi$, where the banded chaotic attractor is converted into a banded chaotic saddle (BCS), and the size of the chaotic attractor is increased, as will be discussed in Section 4.5. Coexisting with a banded attractor inside the periodic window, a surrounding chaotic saddle (SCS), given by red dots in Fig. 4.3(a), is responsible for chaotic transients which mimic the dynamics of the larger chaotic attractor outside the periodic window.

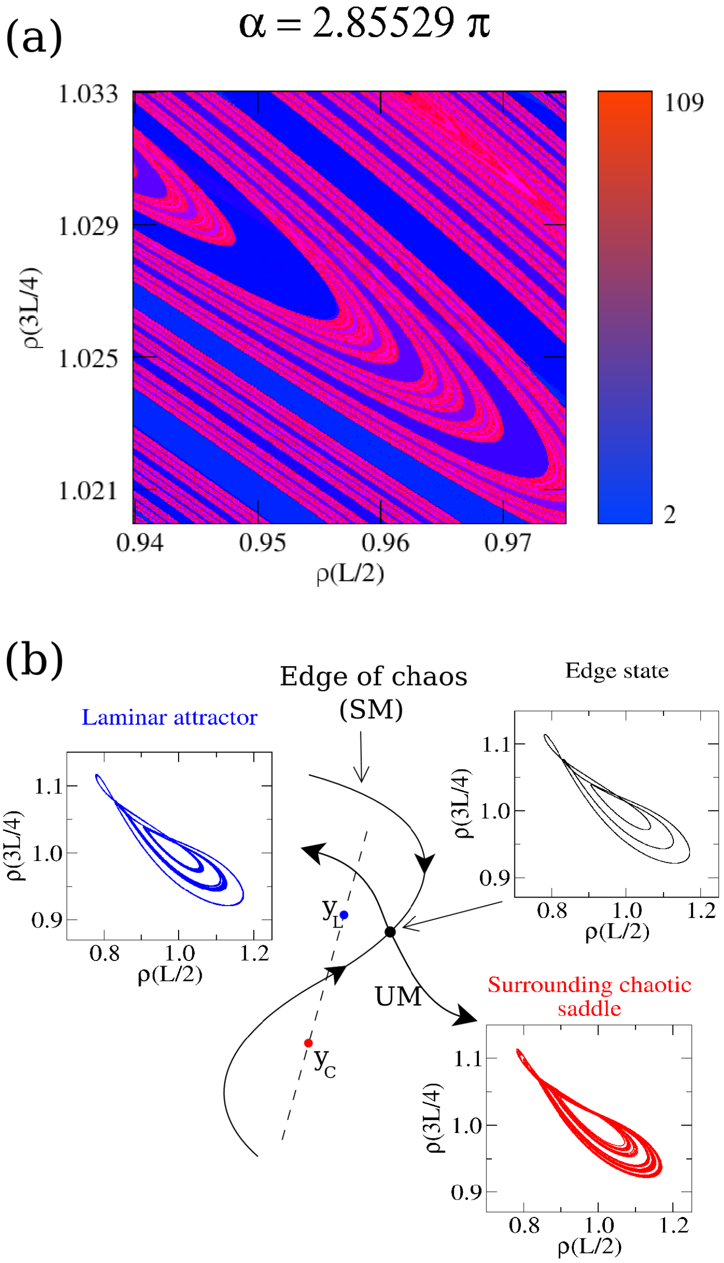

Figure 4.4 - (a) Density plot of the lifetime, given in units of Poincaré map iterations, in a two–dimensional phase–space projection at $\alpha = 2.85529\pi$. Blue areas indicate initial conditions that converge quickly to the attractor. Initial conditions leading to longer lifetimes are represented by red tones. The edge of chaos is given by the boundary between the blue and red areas. (b) Schematic representation of the edge of chaos (SM) indicated by a solid line and its associated saddle object (the edge state). Any initial condition lying on the edge of chaos will converge to the edge state.

4.4 Lifetime function and bisection method

To study how the surrounding chaotic saddle SCS shapes the phase space within the periodic window of Fig. 4.3, we introduce the lifetime function (SKUFCA et al., 2006) of an initial condition

$$\mathbf{y}_0 = \{\rho_i^0, v_i^0\},\ i = 1, \ldots, N, \tag{4.7}$$

where ρ_i^0 and v_i^0 are the initial density and velocity profiles in the spatial grid. The lifetime is defined as the time the initial condition $\mathbf{y}_0$ takes to converge to the attractor inside the periodic window. We use a two–dimensional projection of the Poincaré map $\mathbf{z}_k = \{\rho(x = L/2, t_k), \rho(x = 3L/4, t_k\}$ to facilitate the definition of convergence. Fist, we collect a set of M Poincaré points $S = \{\mathbf{z}_A^j, j = 1, \ldots, M\}$ in the attractor. Then, we integrate the initial condition $\mathbf{y}_0$ generating the discrete two–dimensional Poincaré map $\mathbf{z}_k$. For each discrete time step k, we define the distance between $\mathbf{z}_k$ and S as

$$\Delta(\mathbf{z}_k, S) = \min(||\mathbf{z}_k - \mathbf{z}_A^j||, j = 1, \ldots, M), \tag{4.8}$$

where $||\mathbf{z}_k - \mathbf{z}_A^j||$ is the Euclidean distance. When the distance to the attractor is less than some suitable threshold $\Delta(\mathbf{y}_k, S) < \delta$, we consider $\mathbf{y}_k$ has converged to the attractor. In this case we use $\delta = 10^{-4}$. A two–dimensional density plot of the lifetime in the phase–space at $\alpha = 2.85529\pi$ is shown in Figure 4.4(a). Blue areas denote initial conditions that converge quickly to the banded chaotic attractor. Areas of longer lifetime, in red tones, exhibit an apparent fractal structure, which indicates the proximity of the corresponding initial conditions to the stable manifold of the surrounding chaotic saddle. Thus, there exist two possible trajectories for a given initial condition in the phase space: (i) the trajectory may converge directly to the attractor, or (ii) the trajectory may visit the vicinity of the surrounding chaotic saddle before converging to the attractor. Under this circumstance, we can define two regions or pseudo–basins of attraction in the phase space: the laminar basin (blue region) related to (i), and the chaotic basin (red region) related to (ii). The basin boundary separating laminar and chaotic basins is the edge of chaos (SKUFCA et al., 2006). The asymptotic trajectory on this boundary is called the edge state (ES). In order to determine the ES, we apply the bisection method (SKUFCA et al., 2006). From Fig. 4.4(a) we note that any path connecting the two basins must intersect the edge of chaos (dashed line in Fig. 4.4(b)). First we select two initial conditions, $\mathbf{y}_L$ and $\mathbf{y}_C$, in the laminar and chaotic basins, respectively. Then we integrate the

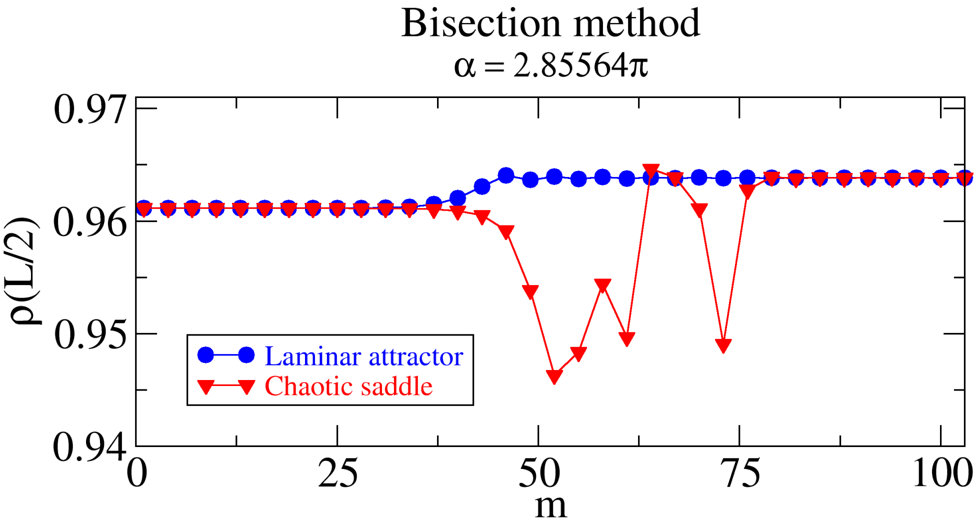

Figure 4.5 - Poincaré time series of two trajectories on the laminar side (blue circles) and chaotic side (red triangles) of the edge of chaos before converging to the p–3 periodic attractor for $\alpha = 2.85564\pi$. Poincaré points are plotted for each three iterations, $m = 1, 4, 7, \ldots$.

initial condition $\mathbf{y}_M{=}(\mathbf{y}_L + \mathbf{y}_C)/2$ and decide which side the initial condition is on. By sucessive bisections we reduce the distance $d = ||\mathbf{y}_L - \mathbf{y}_C||$, and bring $\mathbf{y}_L$ and $\mathbf{y}_C$ close to the edge of chaos. By integrating the system using the final $\mathbf{y}_L$ and $\mathbf{y}_C$ as initial conditions we generate trajectories that track along the edge of chaos, spend some time near the ES, and then depart either to the attractor or to the chaotic saddle.

As an example, we apply the bisection method for $\alpha = 2.85564\,\pi$, in the middle of the periodic window (Fig. 4.3), where the attractor is a p–3 stable periodic orbit. Figure 4.5 shows the Poincaré points of every three iterations of laminar (blue circles) and chaotic (red triangles) initial conditions. Both trajectories go along the edge of chaos in the beginning, passing near the edge state, after which they separate. The laminar trajectory converges quickly and smoothly to the attractor, whereas the chaotic one spends some time near the surrounding chaotic saddle before converging to the attractor. We compute the ES for several values of the control parameter α in the periodic window, and conclude that the saddle object that separates the laminar and chaotic basins is the p–3 UPO that arises jointly with the p–3 periodic attractor at the SNB (black line in Fig 4.3(a)). Hence, the edge state is the p–3 UPO and its stable manifold (SM) is the edge of chaos.

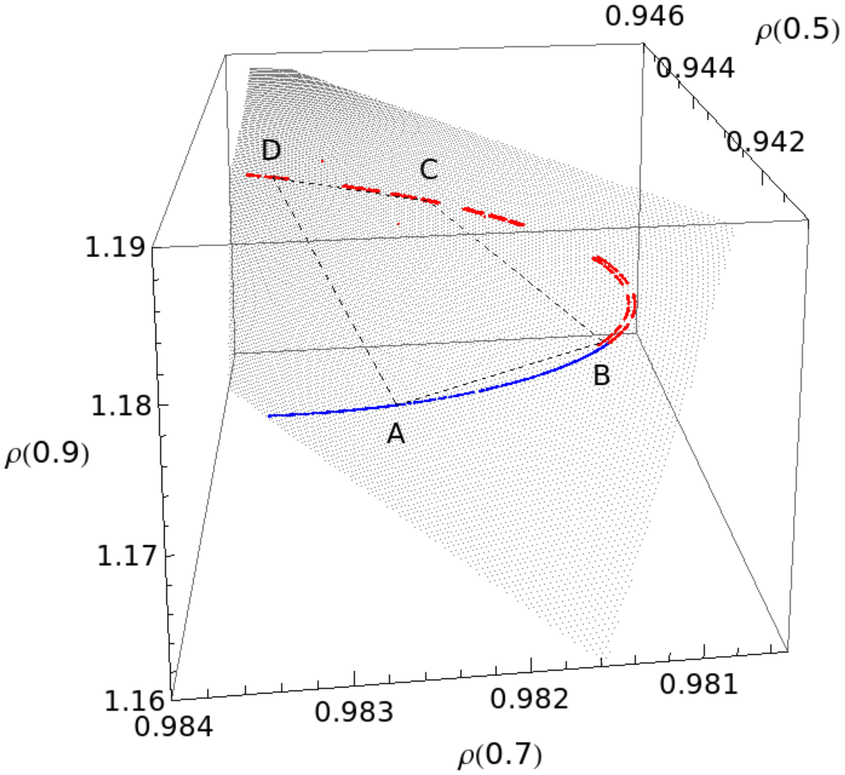

Figure 4.6 - Three–dimensional projection of the grid of initial conditions generated from four points A, B, C and D, containing part of the banded chaotic attractor BCA (blue) and the chaotic saddle SCS (red).

4.5 Interior crisis

In the following, we examine the role of the edge state ES played in the interior crisis which occurs at the end of the periodic window (Fig. 4.3). In chaotic systems with one positive Lyapunov exponent, an interior crisis is a sudden transition triggered by a collision between a chaotic attractor, a mediating unstable periodic orbit UPO and its stable manifold (GREBOGI et al., 1983b), already shown for the mean field dynamo system of Chapter 3. Morever, at the onset of crisis, the surrounding chaotic saddle (SCS) also collides with the attractor (CHIAN et al., 2007). One has to find all these four structures to characterize the crisis. When the crisis takes place, at $\alpha = \alpha_C$, we numerically find the chaotic attractor, the chaotic saddle SCS using the sprinkler method (HSU et al., 1988), and the edge state ES with the bisection

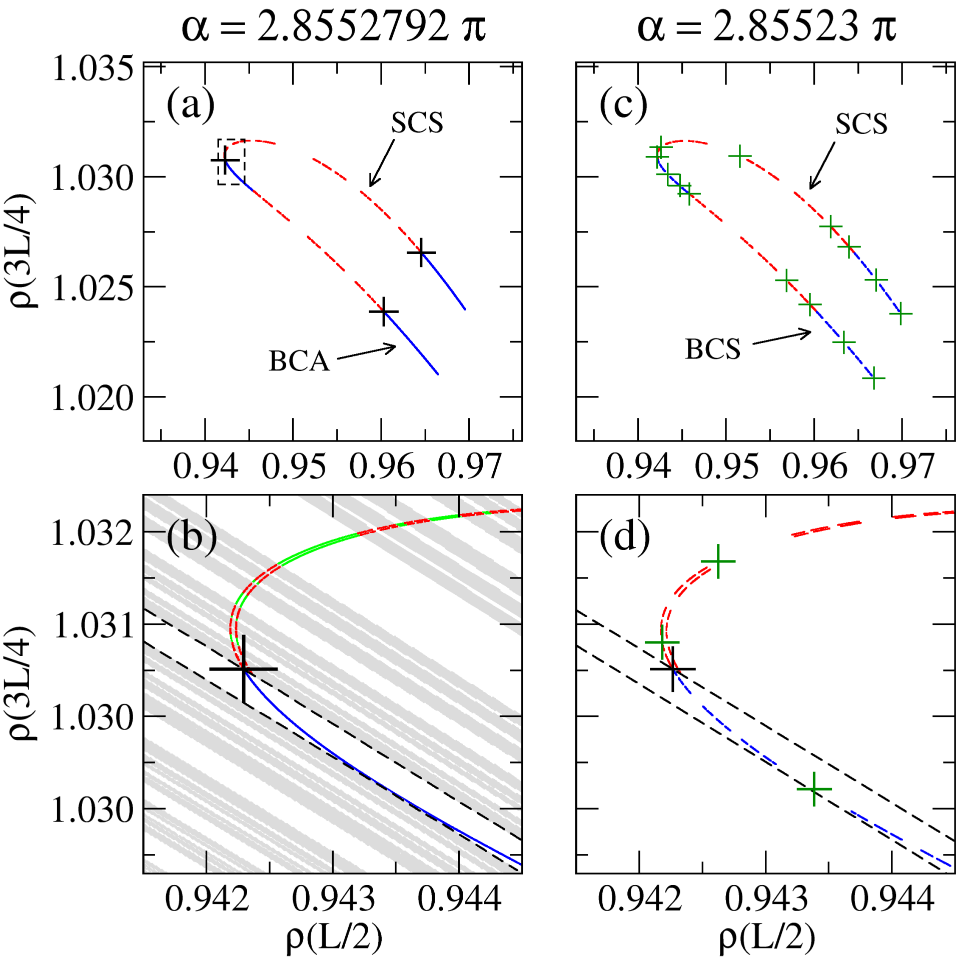

Figure 4.7 - Two–dimensional Poincaré plots at the onset of ((a) and (b)) and after ((c) and (d)) the interior crisis. (a) Three structures involved at the onset of crisis: the banded chaotic attractor (BCA, blue), the surrounding chaotic saddle (SCS, red) and the *p*-3 edge state (black crosses). (b) An enlargement of the dashed rectangle region indicated in (a). The *p*-3 mediating UPO (the edge state) and its stable manifold (the edge of chaos, dashed line) collide with BCA and SCS . The stable (grey) and unstable (green) manifolds of SCS are also shown. (c) Post–crisis banded chaotic saddle (BCS, blue), SCS, and a *p*–14 coupling UPO (green crosses) with its branches in the gaps of both banded and surrounding regions. (d) An enlargement of (c). The edge state (black cross) and the edge of chaos (dashed lines) are also shown.

method (SKUFCA et al., 2006). As in Chapter 3, we use the fact observed by Rempel et al. (2004a) that the boundary of the stable manifold of SCS approximates the stable manifold of the mediating UPO. We compute the stable manifold of the SCS with the projection technique developed by Rempel et al. (2004a) to study chaotic

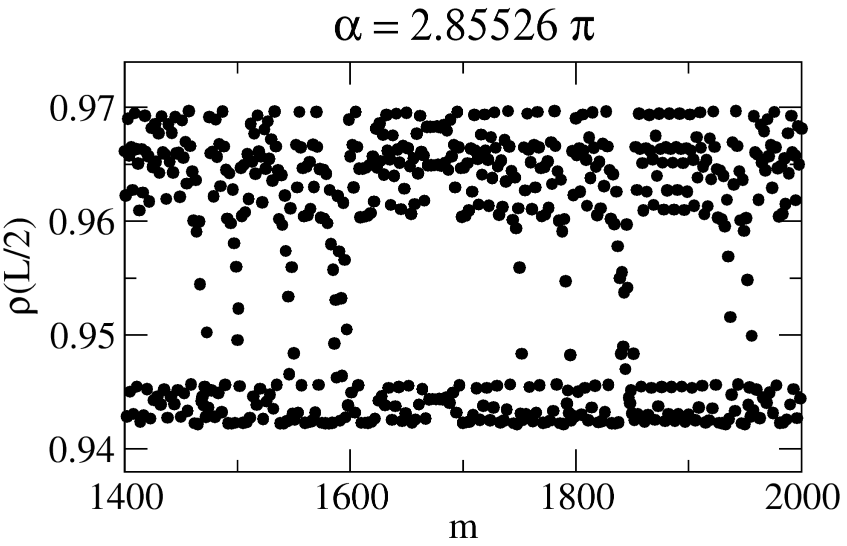

Figure 4.8 - Poincaré time series showing crisis–induced intermittency.

transitions in high–dimensional systems. A suitable grid of chosen initial conditions is constructed using one point A from BCA and three points B, C and D from SCS at the vicinity of the collision. Figure 4.6 shows a three–dimensional projection of this grid (grey points) jointly with the attractor BCA (blue) and the chaotic saddle SCS (red) at the moment of the interior crisis. Figure 4.7(a) shows the attractor BCA (blue), the surrounding chaotic saddle SCS (red dot) and the p–3 edge state ES (black crosses) in a two–dimensional projection of the phase space. The grid of initial conditions near the collision corresponds to the dashed rectangle of Fig. 4.7(a). Figure 4.7(b) displays a zoomed–in view of this region to elucidate the collision which characterizes the interior crisis. At the onset of the interior crisis, the chaotic saddle (red) and the boundary of its stable manifold (grey) collide with the banded chaotic attractor (blue). The edge state (black cross) and its stable manifold (dashed lines) form the boundary between the attractor and the chaotic saddle pseudo–basins (blue and red regions, respectively, in Fig. 4.4(a)), and when they collide, the edge of chaos also collides simultaneously with them.

4.6 Intermittency

At the collision the chaotic attractor loses its stability and is converted into a banded chaotic saddle (BCS). The SCS is robust and persists after the crisis. Figure 4.7(c) shows these two non–attracting chaotic sets at $\alpha = 2.85523\,\pi$, after crisis characterized by gaps. After the onset of the interior crisis, an infinite number of coupling UPOs are created, filling the gap regions via an event called *explosion* (ROBERT et al., 2000; SZABÓ et al., 2000). These newly created unstable periodic orbits have components in both surrounding and banded regions and are responsible for the coupling of the two regions. In general, the coupling UPOs are difficult to find numerically, due to their long periods. This is a particularly complex task in a spatially extended system. Using the technique introduced by Lathrop and Kostelich (1989) we found a p–14 coupling UPO, which is plotted as green crosses in Fig. 4.7(c). An enlargement of the same region of phase space as in Fig 4.7(b) is shown in Fig 4.7(d), including the edge state (black cross) and its stable manifold (dashed lines). After the crisis the edge of chaos separates the two regions occupied by SCS and BCS.

The link between both regions provided by the coupling UPOs has, as a direct consequence, the formation of a larger chaotic attractor characterized by an intermittent behavior. Figure 4.8 shows the time series of crisis–induced intermittency corresponding to the post–crisis chaotic attractor. The laminar and bursty periods of the crisis–induced intermittency correspond to the trajectory visiting the vicinity of the BCS and SCS chaotic saddles, respectively.

5 EDGE OF CHAOS AND SPATIOTEMPORALLY CHAOTIC SADDLES AT THE LAMINAR–TURBULENCE TRANSITION

Three–dimensional turbulence in fluids and plasmas can be studied both, by means of experimental measurements, as in Chapter 2, and by solving numerically the partial differential equations describing the spatio–temporal evolution of density, velocity, magnetic field, etc. Direct numerical simulations of turbulence require a considerable computational effort, involving large and expensive hardware and long runs. Chaos theory can describe some phenomena related to turbulence, as we showed in Chapters 3 and 4, but the lack of spatial information in low–dimensional systems makes it hard to draw conclusions to understand the nonlinear dynamics of real fluids (REMPEL et al., 2009a). On the other hand, many applications of chaos theory are based on the possibility of exploring wide regions of the phase space, in other words, it is necessary to evolve many initial configurations until they reach some final state. For this reason, a direct application of chaos theory to the fluid equations is sometimes unfeasable. A possible solution to this problem is to use systems with just one spatial dimension modeled by a partial differential equation that can exhibit spatiotemporally chaotic behavior.

In this Chapter the ideas presented in Chapters 3 and 4 are applied to the Benjamin–Bona–Mahoney equation, a partial differential equation used to model nonlinear drift waves in magnetized plasmas and shallow water waves in fluids, such as tsunamis. This equation is also known as the regularized long–wave equation (RLWE). In Section 5.1 and 5.2 we present the equation and the representation of dynamical variables we use in our work. In Section 5.3 a Hamiltonian formalism is derived for the conservative case of the RLWE. In Section 5.4 a detailed description of all attractors found in the system and the bifurcations they undergo is given. The genesis of an edge state and the chaotic saddle responsible for the spatiotemporally chaotic transients are studied in Section 5.5. Finally, in Section 5.6 we analyze the transition to turbulence in terms of the edge of chaos.

5.1 Regularized Long–Wave Equation

The driven–damped regularized long–wave equation (RLWE), also known as Benjamin–Bona-Mahony equation, is given by

$$\partial_t u + a\partial_{txx} u + c\partial_x u + f u \partial_x u = -\gamma u - \epsilon \sin(x - \Omega t) \tag{5.1}$$

where $u(x,t)$ is a real function of space and time, a, c and f are constants, ν is a damping parameter, ϵ is the driver amplitude, and Ω is the driver frequency. We define periodic boundary conditions $u(x,t) = u(x+2\pi,t)$, and fix $a = -0.28711$, $c = 1$, $f = -6$, $\nu = 0.1$, and $\Omega = 0.65$. These parameter values can be chosen arbitrarily, with the exception of a, which must be negative for physical reasons and to avoid numerical instability (HE; SALAT, 1989). Here, the values are chosen following the previous works of He and Chian (2003), Rempel and Chian (2007) and Chian et al. (2010).

We solve Eq. (5.1) using a pseudo–spectral method, by expanding $u(x,t)$ in a Fourier series (REMPEL; CHIAN, 2007):

$$u(x,t) = \sum_{k=-N/2}^{N/2} \hat{u}_k(t) e^{ikx}. \tag{5.2}$$

We set the number of modes $N = 32$. By introducing (5.2) into (5.1) we obtain a set of ordinary differential equations for the complex Fourier amplitudes $\hat{u}_k(t)$:

$$(1-ak^2)\frac{d\hat{u}_k}{dt} = -ick\,\hat{u}_k - \nu\hat{u}_k + \frac{\epsilon}{2}[(\sin\Omega t + i\cos\Omega t)\delta_{1,k} - f\mathcal{F}(u\partial_x u), \tag{5.3}$$

where the last term on the right–hand side is the Fourier transform of the nonlinear part of (5.1). In the pseudo–spectral method this term is computed in the real space using information from the Fourier space. First, we compute the derivative in the Fourier space $\partial_x u \to ik\hat{u}_k$ and then both $\hat{u}_k$ and $ik\hat{u}_k$ are inverse Fourier transformed to real space, where the multiplication $fu\partial_x u$ is performed. Finally, the result is Fourier transformed back to the Fourier space. Numerical integration is performed using a fourth–order Runge–Kutta integrator, with a time step $\Delta t = T/500$, where $T = 2\pi/\Omega$ is the driver period in Eq. (5.1). At each time step, 1/3 of the highest k modes are set to zero to avoid aliasing errors. Thus, the effective number of modes is $N = 20$.

5.2 Amplitude–phase representation and Poincaré section

An important issue to consider when studying different kinds of solutions in high–dimensional systems is to choose a good representation of the available information, in order to achieve a correct interpretation of the physical situation being investigated. Based on the fact shown by He (2005), that for a small ϵ the asymptotic solution of equation (5.1) is a steady wave (SW) in the form $u_0(x,t) = u(x - \Omega t)$, we adopt the amplitude–phase representation of the variables $\hat{u}_k$ to describe the dynamics of the system. Expression (5.2) can be written in terms of amplitude and phase in the laboratory frame of reference (x,t) as

$$u(x,t) = \sum_{k=1}^{N} |\hat{u}_k(t)| \cos(kx + \phi_k^L(t)), \tag{5.4}$$

where

$$|\hat{u}_k| = \sqrt{[\mathrm{Re}\, \hat{u}_k]^2 + [\mathrm{Im}\, \hat{u}_k]^2} \qquad \text{and} \qquad \phi_k^L = \tan^{-1}\left(\frac{\mathrm{Im}\, \hat{u}_k}{\mathrm{Re}\, \hat{u}_k}\right). \tag{5.5}$$

The driver frame of reference (ξ, τ) is given by the follow transformation:

$$\xi = x - \Omega t \qquad \tau = t. \tag{5.6}$$

Introducing (5.6) into (5.4), we have

$$\begin{aligned} u(\xi,\tau) &= \sum_{k=1}^{N} |\hat{u}_k(\tau)| \cos(k[\xi + \Omega t] + \phi_k^L(t)) && (5.7) \\ &= \sum_{k=1}^{N} |\hat{u}_k(\tau)| \cos(k\xi + \phi_k^D(t)), && (5.8) \end{aligned}$$

with the phase in the driver frame

$$\phi_k^D = \phi_k^L + k\Omega t. \tag{5.9}$$

Here, the phase shift $k\Omega t$ arises from the Doppler effect depending on wave number k. Comparing expression (5.8) with the form of the SW solution $u_0 \equiv u_0(\xi)$, we see that both $|\hat{u}_k|$ and ϕ_k^D have to be independent of time. Hence, the SW solution is a fixed point in the driver frame using the amplitude–phase Fourier representation. An example of the steady wave for $\epsilon = 0.01$ is shown in Fig. 5.3(b), plotted using (5.8).

Furthermore, He (2005) showed that at a certain value ϵ_H a Hopf bifurcation occurs, the SW fixed point becomes unstable and a limit cycle replaces it as the new attractor. For $\epsilon > \epsilon_H$ all the solutions oscillates around some value in time. For this reason it is convenient to introduce a Poincaré section to construct a map, from which the bifurcation behavior can be revealed. Inspecting the numerical solutions, we choose

$A_2 = 0.1$ and $dA_2/dt > 0$ as the Poincaré map in this case.

The temporal evolution of the wave energy, which is a constant of motion for $\nu = \epsilon = 0$, is

$$E(t) = \frac{1}{4\pi}\int_0^{2\pi} [u(x,t)^2 - a u_x(x,t)^2]\, dx. \tag{5.10}$$

Substituting (5.8) into (5.10), and recalling that $\tau = t$, we have the energy in terms of the Fourier spectrum,

$$E(t) = \frac{1}{4}\sum_{k=1}^{N}(1 - ak^2)|\hat{u}_k(t)|^2. \tag{5.11}$$

We will use this quantity to investigate bifurcations in the parameter space in Section 5.4.

5.3 Hamiltonian formulation

In the absence of dissipation and an external source of energy ($\nu = \epsilon = 0$), the long wave equation (5.1) is written as

$$\partial_t u + a\partial_{txx} u + c\partial_x u + f u \partial_x u = 0, \tag{5.12}$$

As a first approach, in this section we study travelling waves of Eq. (5.12) with the form

$$u(x,t) = u(x - Vt). \tag{5.13}$$

Introducing the new variable $\xi = x - Vt$ and using the chain rule, the temporal and spatial derivatives are transformed into a total derivative of ξ:

$$\frac{\partial}{\partial t} = \frac{\partial \xi}{\partial t}\frac{d}{d\xi} = -V\frac{d}{d\xi} \qquad \frac{\partial}{\partial x} = \frac{\partial \xi}{\partial x}\frac{d}{d\xi} = \frac{d}{d\xi}. \tag{5.14}$$

using Eqs. (5.14) in Eq. (5.12), we obtain the following third–order ODE:

$$\frac{d^3 u}{d\xi^3} = A\frac{d}{d\xi}u^2 + B\frac{du}{d\xi}, \tag{5.15}$$

where $A = f/(2aV)$ and $B = (c - V)/(aV)$. Integrating once, we obtain

$$\frac{d^2 u}{d\xi^2} = Au^2 + Bu + C, \tag{5.16}$$

where C is an integration constant. Finally, introducing a new variable $v = du/d\xi$, we can rewrite Eq. (5.16) in a Hamiltonian form:

$$\frac{du}{d\xi} = \frac{\partial H}{\partial v}, \tag{5.17}$$

$$\frac{dv}{d\xi} = -\frac{\partial H}{\partial u}, \tag{5.18}$$

with

$$H(u, v) = -\left(A\frac{u^3}{3} + B\frac{u^2}{2} + Cu\right) + \frac{v^2}{2}. \tag{5.19}$$

The equilibrium solutions or fixed points of the Hamiltonian system can be found equating equations (5.17)–(5.18) to zero. In this case, due to the quadratic nonlinearity, there are two fixed points $\mathbf{p}_\pm$ given by

$$\mathbf{p}_\pm = \{u_\pm, 0\} = \left\{\frac{-B \pm \sqrt{B^2 - 4AC}}{2A}, 0\right\}. \tag{5.20}$$

To classify the two fixed points $\mathbf{p}_\pm$ and their stability, first we linearize equations (5.17)–(5.18) around the fixed point $\mathbf{p}_\pm$,

$$\frac{d}{d\xi}\begin{pmatrix} u \\ v \end{pmatrix} = \mathbf{J}(\mathbf{p}_\pm)\begin{pmatrix} u \\ v \end{pmatrix}, \tag{5.21}$$

where $\mathbf{J}(\mathbf{p}_\pm)$ is the Jacobian matrix

$$\mathbf{J}(\mathbf{p}_\pm) = \begin{pmatrix} \frac{\partial^2 H}{\partial u \partial v} & \frac{\partial^2 H}{\partial v^2} \\ -\frac{\partial^2 H}{\partial u^2} & -\frac{\partial^2 H}{\partial u \partial v} \end{pmatrix} = \begin{pmatrix} 0 & 1 \\ 2Au_\pm + B & 0 \end{pmatrix}. \tag{5.22}$$

The classification and stability of $\mathbf{p}_\pm$ are given by the two eigenvalues of matrix (5.22),

$$\lambda_1^\pm = \sqrt{2Au_\pm + B} \quad \text{and} \quad \lambda_2^\pm = -\sqrt{2Au_\pm + B}. \tag{5.23}$$

We are interested in the case where the two fixed points coexist. Using the values of a, c and f defined in Section 5.1, the condition $C < 0$ is enough to ensure the coexistence of two fixed points. Under these conditions, the eigenvalues of $\mathbf{p}_-$ only have imaginary part, and the eigenvalues of $\mathbf{p}_+$ are real numbers, one positive and one negative, as shown in Fig. 5.1. We conclude that $\mathbf{p}_-$ is a center point, generating oscillatory solutions around it, and u_+ is a saddle point, with one attracting direction related to the negative eigenvalue, and one repelling direction, related to the positive

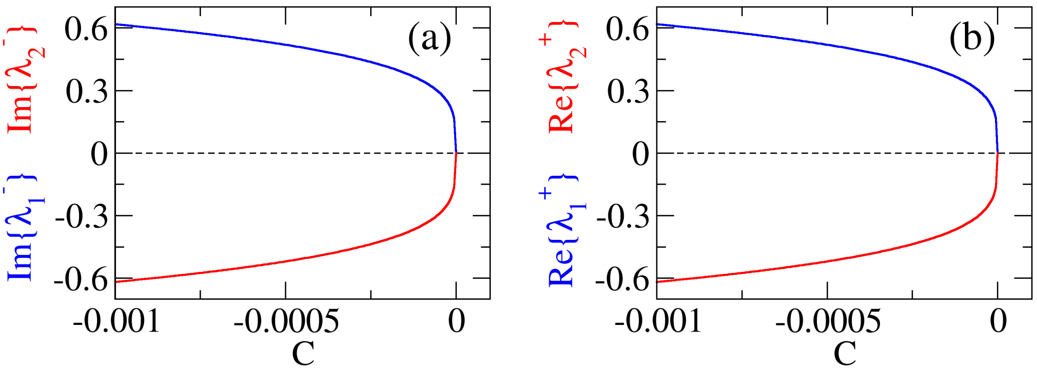

Figure 5.1 - Stability analysis of fixed points $\mathbf{p}_-$ (left panel) and $\mathbf{p}_+$ (right panel). For $C < 0$, the eigenvalues of $\mathbf{p}_-$ are imaginary, and the eigenvalues of $\mathbf{p}_+$ are real, one positive and one negative. $\mathbf{p}_-$ is a center and $\mathbf{p}_+$ is a saddle. When $C = 0$ both fixed points cease to exist.

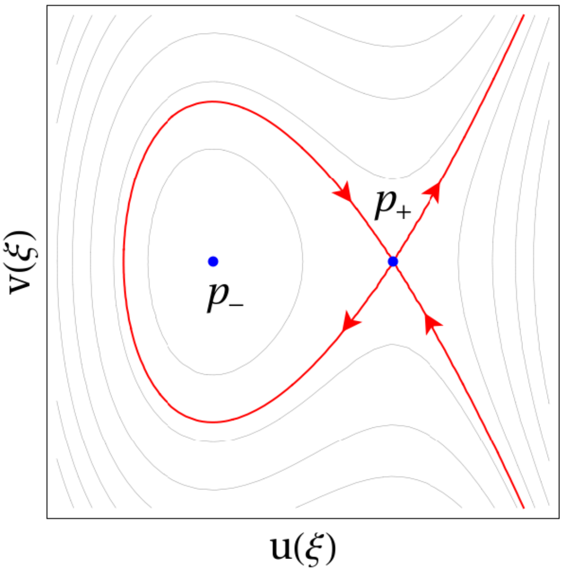

Figure 5.2 - Contours of $H(u, v)$. Each curve defines a constant energy solution of the system of equations (5.17)–(5.18). Red lines denote the stable and unstable manifolds of $\mathbf{p}_+$.

eigenvalue.

Figure 5.2 is a visualization of the phase space. The fixed points $\mathbf{p}_-$ and $\mathbf{p}_+$ are represented by blue dots. Because the system is conservative, each contour line $H(u, v)$ =constant represents a particular solution. The attracting and repelling directions of $\mathbf{p}_+$, shown as a red line surrounding the center point $\mathbf{p}_-$, define a

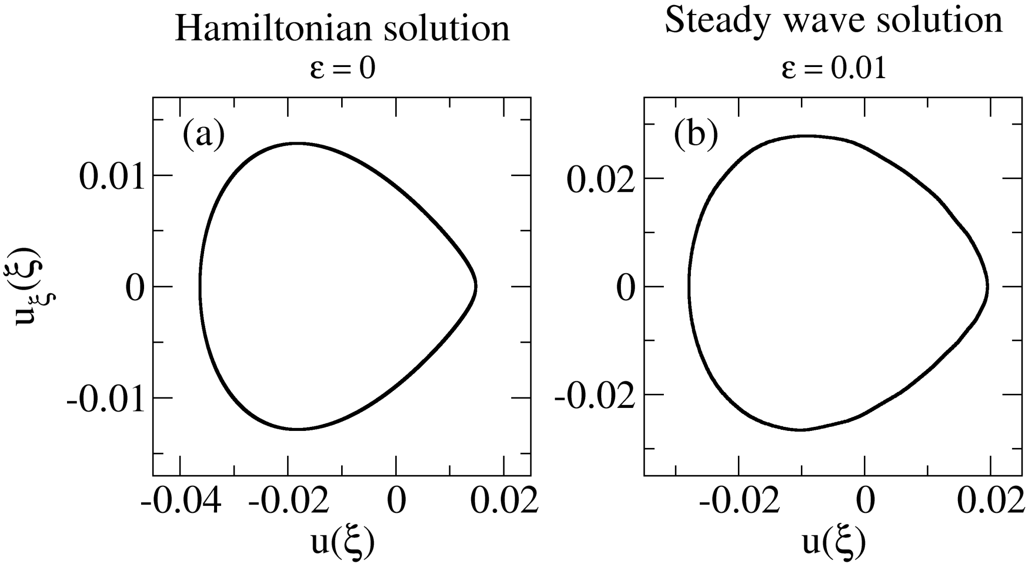

Figure 5.3 - Solutions of Eq. (5.1) for: (a) $\epsilon = 0$ and $\nu = 0$, and (b) $\epsilon = 0.01$ and $\nu = 0.1$.

separatrix of the phase space, and it is called a homoclinic curve. Solutions within the curve are oscillatory, and solutions outside the curve are unbounded. The separatrix itself defines a solitary wave.

Even though the Hamiltonian system for travelling waves (5.17)–(5.18) represents a severe simplification of the complete problem (5.1), it predicts fairly well the shape of solutions when dissipation and an external source are added. Figure 5.3 shows an oscillatory solution of the Hamiltonian system (left panel) compared with a solution obtained by solving numerically Eq. (5.1) for $\epsilon = 0.01$ and $\nu = 0.1$. This result shows that the phase space portrait of the long wave equation for the conservative case is a mimic of the complete phase space, at least for small values of ϵ and ν. The consequences of adding more driver energy into the system will be discussed in the following section.

5.4 Attractors and bifurcations

In this section we analyze the different kind of solutions of Eq. (5.1) and the bifurcations they suffer as the control parameter ϵ is varied. We are interested in investigating the domain of solutions in the interval $\epsilon \in [0, 0.25]$, which has been reported in previous works as containing a rich variety of nonlinear dynamics, including steady travelling waves (SW), periodic, quasiperiodic, temporally chaotic

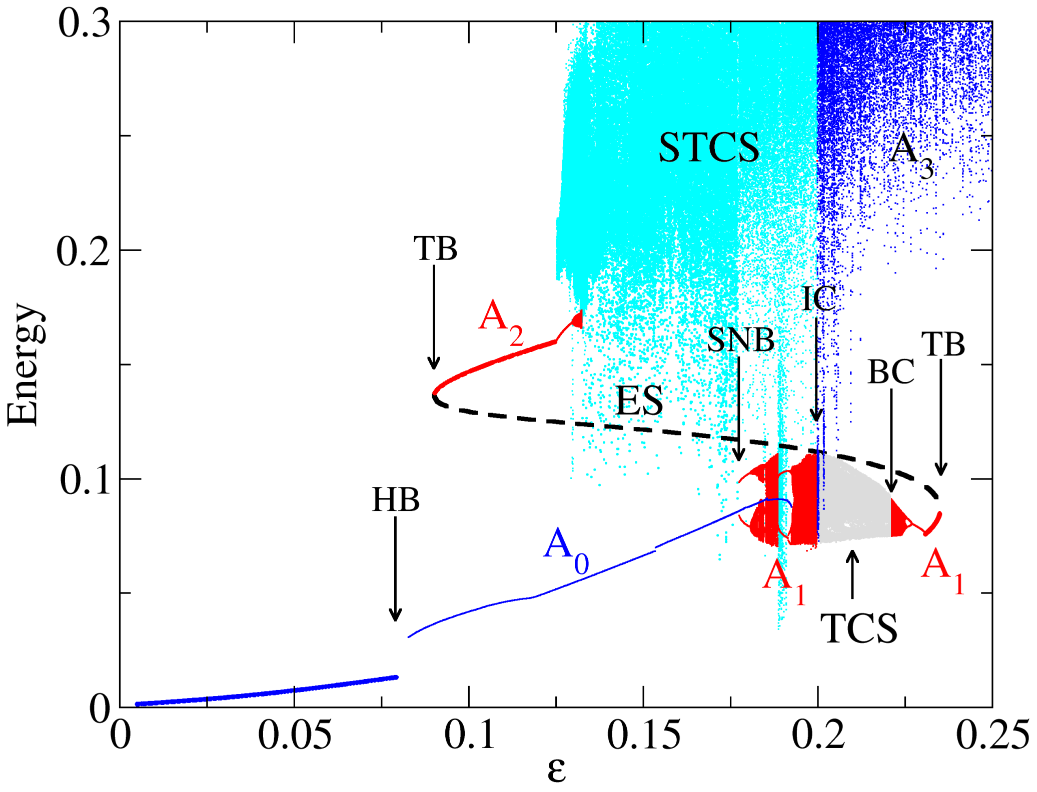

Figure 5.4 - Bifurcation diagram of all solutions of Eq. (5.1) in the interval $\epsilon \in [0, 0.25]$. Arrows indicate bifurcations and transitions suffered by different solutions as the parameter is varied.

and spatiotemporally chaotic attractors (HE, 2005; REMPEL; CHIAN, 2007).

We have identified a total of four different attractors in the interval $\epsilon \in [0, 0.25]$, each of which bifurcates independently as a function of ϵ. The bifurcation diagram for these four attractors is shown in Fig. 5.4. Points corresponding to the wave energy are plotted every time a particular solution crosses the Poincaré section described in section 5.2. The fixed point solutions, represented by thick lines, have not Poincaré map associated and we only plot the energy, which is constant for a given ϵ. In the following we describe in detail the four different attractors and their corresponding bifurcations.

Attractor A_0 is represented by a blue thick line at the left of Fig. 5.4, and arises as a fixed point when $\epsilon > 0$. This fixed point loses its stability at $\epsilon \approx 0.079$, when a Hopf bifurcation occurs, marked as HB in Fig. 5.4. At that point a period–1 periodic

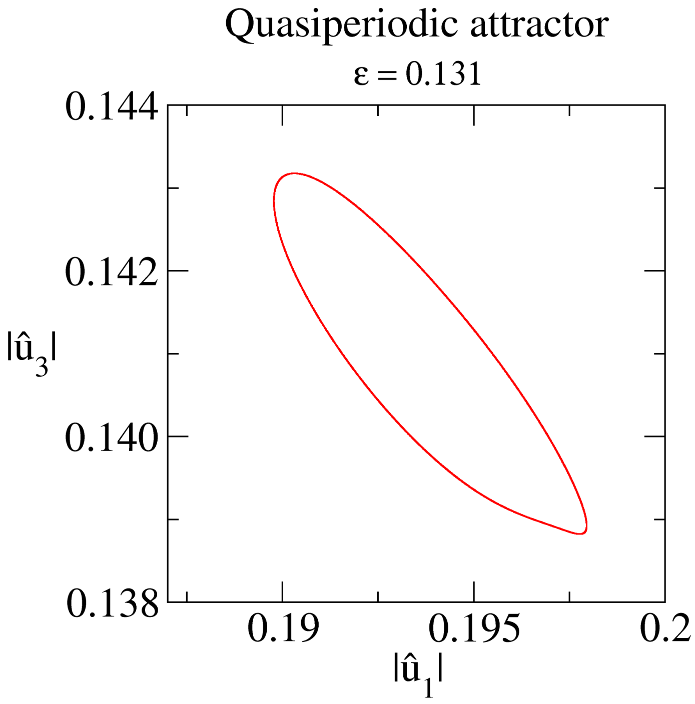

Figure 5.5 - Two–dimensional projection of the Poincaré map of quasioperiodic attractor A_2 at $\epsilon = 0.131$.

orbit is created, remaining until $\epsilon \approx 0.1925$, when the orbit in no longer observed in the phase space. Attractor A_0 only changes its energy as ϵ increases and does not suffer any other bifurcation.

Attractor A_2 arises in a tangent bifurcation TB at $\epsilon \approx 0.09$, when two fixed points, one stable (thick red line) and one unstable, labeled ES (black dashed line), are created. The important role of the unstable fixed point is the central topic of this chapter, and we devote an entire section to explain its nature, how to find it and its influence on the organization of the phase space of the entire system. Continuing with the bifurcation scenario of A_2, when $\epsilon \approx 0.125$ the attractor suffers a Hopf bifurcation and becomes a periodic orbit (thin red line). At $\epsilon \approx 0.1297$ a transition occurs, seen as the moment when Poincaré points densely fill the region around the single–point periodic attractor, which loses its stability in the transition. Figure 5.5 is a 2D projection of the Poincaré map at $\epsilon = 0.131$, after the transition, showing that points in the attractor form a closed curve, indicating that the limit cycle has bifurcated into a 2D torus, and A_2 has become a quasiperiodic attractor. This attractor loses its stability at $\epsilon \approx 0.13235$, ceasing to exist. Coexistence of attractors

A_0 and A_2 implies that each attractor possesses its own basin of attraction, a region of the phase space whose initial conditions converge to the specific attractor. The bifurcation analysis of the basin boundary is crucial to understand the origin of spatiotemporally chaotic transients and the transition to wave turbulence, as we will see in sections 5.5 and 5.6.

A saddle–node bifurcation SNB is observed at $\epsilon \approx 0.1774$. From this transition the period–2 periodic attractor A_1 arises, which is plotted as red points in Fig. 5.4. This attractor shows a number of different bifurcations as ϵ is increased, involving a transition to quasiperiodicity and a series of period doubling cascades to temporal chaos, with some periodic windows interspersed in the parameter space. Near $\epsilon \approx 0.1925$ the attractor becomes chaotic in time, and it remains chaotic until $\epsilon \approx 0.2$, when it suddenly loses its stability via an interior crises (IC), leading to the spatiotemporally chaotic attractor A_3, shown as a dense region of dark blue dots in Fig. 5.4. The origin of this attractor is a spatiotemporally chaotic saddle (STCS) which exist in the phase space for $\epsilon < 0.2$, plotted as light blue dots, and becomes attracting at the transition. The genesis of the STCS is studied in Section 5.5, while the details about the interior crisis transition to spatiotemporal chaos are discussed in Section 5.6. After the transition, a temporal chaotic saddle TCS (grey dots in Fig. 5.4) is created from the destabilized attractor A_1. The temporally chaotic saddle continues to exist until $\epsilon \approx 0.22105$, when a boundary crisis (BC) takes place and the TCS becomes a temporally chaotic attractor. This attractor is labelled A_1 because it shares a common origin with the chaotic attractor that loses its stability in the interior crisis IC. A more detailed explanation of this boundary crisis is given in Section 5.6. When ϵ is increased, attractor A_1 eventually becomes a period–1 orbit via an inverse period doubling cascade. This periodic attractor disappears when a Hopf bifurcation takes place at $\epsilon \approx 0.2308$, and a fixed point, represented by a red thick line, replaces it. Finally, the fixed point A_1 disappears in a tangent bifurcation (TB) at $\epsilon \approx 0.235$, jointly with the saddle fixed point ES previosuly created with A_2.

5.5 Genesis of the edge state and the STCS

In this section we will discuss the genesis of an important structure called *edge state* (ES), and how it is related to the origin of the spatiotemporally chaotic saddle STCS shown in Fig. 5.4. These two structures are fundamental to understand a variety of phenomena that have been reported in the past, such as spatiotemporally chaotic

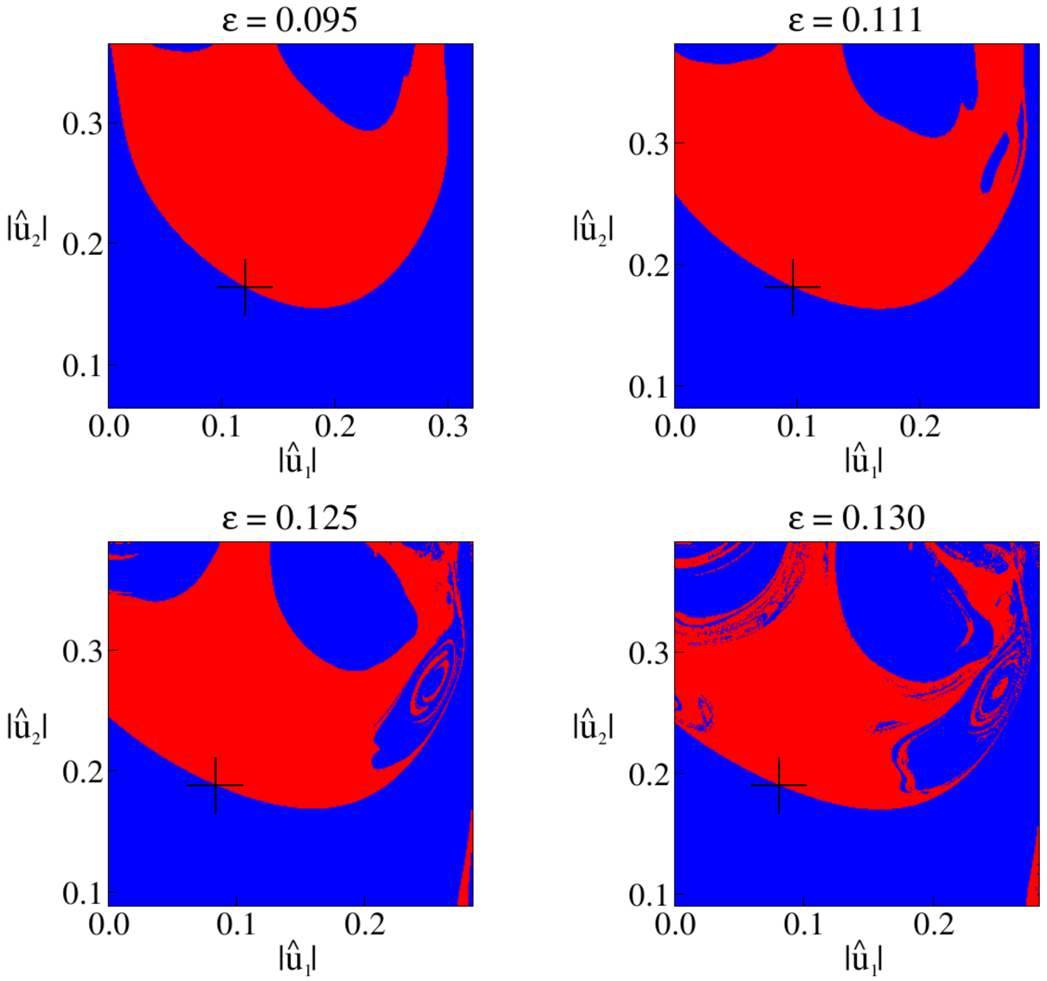

Figure 5.6 - Basins of attraction for attractors A_0 (blue) and A_2 (red), for $\epsilon = 0.095, 0.111, 0.125$ and 0.13. Black cross denotes the edge state ES in each case.

transients and the transition to a fully–developed spatiotemporally chaotic attractor STCA (REMPEL; CHIAN, 2007), spatiotemporal intermittency (REMPEL et al., 2009a) and amplitude–phase synchronization (HE; CHIAN, 2003; CHIAN et al., 2010). Spatiotemporally chaotic states in the Eq. (5.1) are equivalent to wave turbulence solutions, and therefore it is possible to do some analogies between the phenomenology found here and those related to more complicated problems, such as transition to turbulence in neutral fluids and plasmas.

As we mentioned in Section 5.4, when the attractor A_2 arises as a stable fixed point, an unstable fixed point is created at the same time. Attractor A_2 coexists with the periodic orbit A_0, and each one has its own basin of attraction, which corresponds to the set of initial conditions converging to the attractor. The basins of attraction are separated by boundaries. We define the edge state as the saddle structure that lies in the basin boundary. The bisection method, described in Chapter 4, has been adapted to this situation, considering the attractors A_0 and A_2 as the final states separated by the edge state. We found that the edge state ES is the unstable fixed point born in the tangent bifurcation TB, as show in Fig. 5.4. The edge state corresponds to a saddle steady wave moving with the driver speed Ω in the laboratory frame.

Figure 5.6 shows the basins of attraction of A_0 (blue region) and A_2 (red region) for $\epsilon = 0.095, 0.111, 0.125$ and 0.13, jointly with the ES, denoted by a white cross, in each case. As can be observed, the basin boundary changes from smooth to a more complicated shape as ϵ is increased. In other words, the basin boundary suffers a metamorphosis, and becomes fractal.

It is a well known fact that if a basin boundary is fractal, then there is a chaotic saddle in the boundary (LAI; TÉL, 2011). The typical mechanism by which a basin boundary becomes fractal is called homoclinic tangency, and is outlined in Fig. 5.7. Throughout the process, where ϵ is the bifurcation parameter, there is a saddle fixed point, denoted ES. The stable manifold of ES is the basin boundary between an attractor to its right (shown) and another attractor (not shown). For $\epsilon < \epsilon^*$, the basin boundary is smooth. When $\epsilon = \epsilon^*$, homoclinic tangencies between the stable and unstable manifolds of ES occurs. For $\epsilon > \epsilon^*$, a chaotic saddle is created as a consequence of the infinite homoclinic crossings, implying a Smale horseshoe–type dynamics (LAI; TÉL, 2011). The stable manifold of the chaotic saddle, and consequently the basin boundary, becomes fractal. This bifurcation is called smooth–to–fractal basin boudary metamorphosis (GREBOGI et al., 1987).

From Fig. 5.6 and the scenario described above, we conclude that somewhere in the interval $\epsilon \in [0.095, 0.125]$, a homoclinic tangency involving the stable and unstable manifolds of the edge state ES takes place. To quantify the metamorphosis of the basin boundary, we compute its fractal dimension for several values of ϵ. The fractal dimension of the basin boundary is obtained by calculating the probability f of two initial conditions separated by a distance δ to lie in different basins (GREBOGI et al., 1983a). In general, we have

$$f(\delta) \sim \delta^{\alpha}, \tag{5.24}$$

where the scaling exponent $\alpha = D - d$ is called the uncertainity exponent, D is the

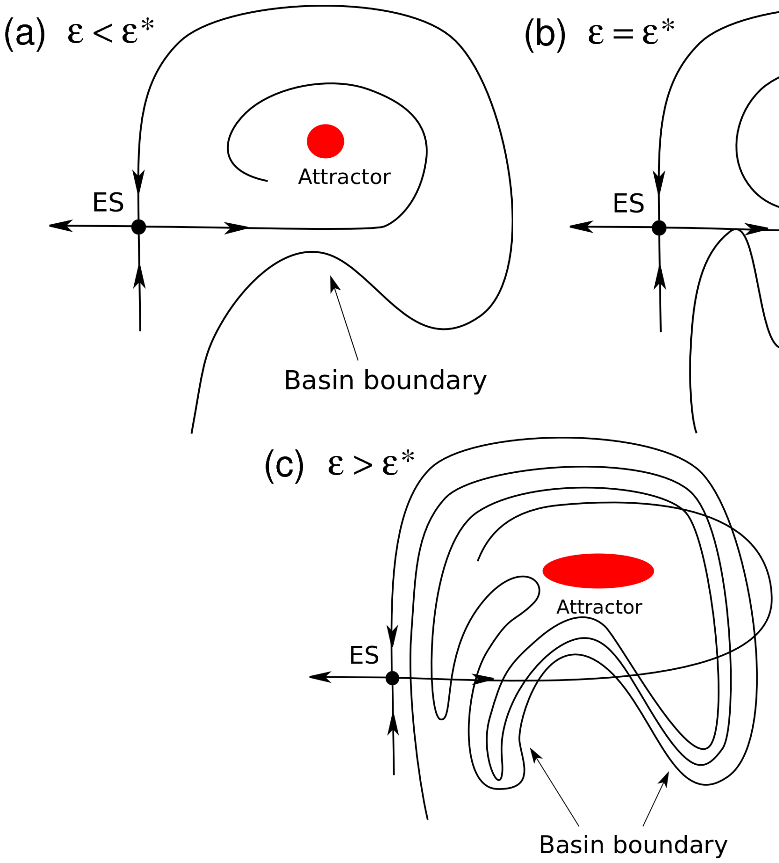

Figure 5.7 - Dynamical mechanism that creates fractal basin boundaries and a chaotic saddle within. (a) Smooth basin boundary for $\epsilon < \epsilon^*$. (b) Homoclinic tangencies for $\epsilon = \epsilon^*$. (c) Homoclinic crossings for $\epsilon > \epsilon^*$. The stable manifold, and consequently the basin boundary, becomes fractal. Adapted from Lai and Tél (2011).

total dimension of the phase space, and d is the dimension of the basin boundary. Figure 5.8 summarizes the results of this calculation over the interval $\epsilon \in [0.095, 0.132]$, where there is a coexistence of attractors. We use a two–dimensional phase space projection $(|\hat{u}_1|, |\hat{u}_2|)$ with $D = 2$. Figure 5.8(a) shows the bifurcation diagram of A_2 and ES, and 5.8(b) is the basin boundary fractal dimension as a function of ϵ. $d = 1$ corresponds to a smooth boundary, which seems to be the case until $\epsilon \approx 0.11$, when the fractal dimension becomes greater than one. From there onwards, the fractal dimension increases quickly with the parameter, in agreement with changes observed along the different panels of Fig. 5.6.

From the previous analysis, it can be concluded that a chaotic saddle STCS is created near $\epsilon \approx 0.11$. In order to determine the dynamical spatiotemporal properties of this

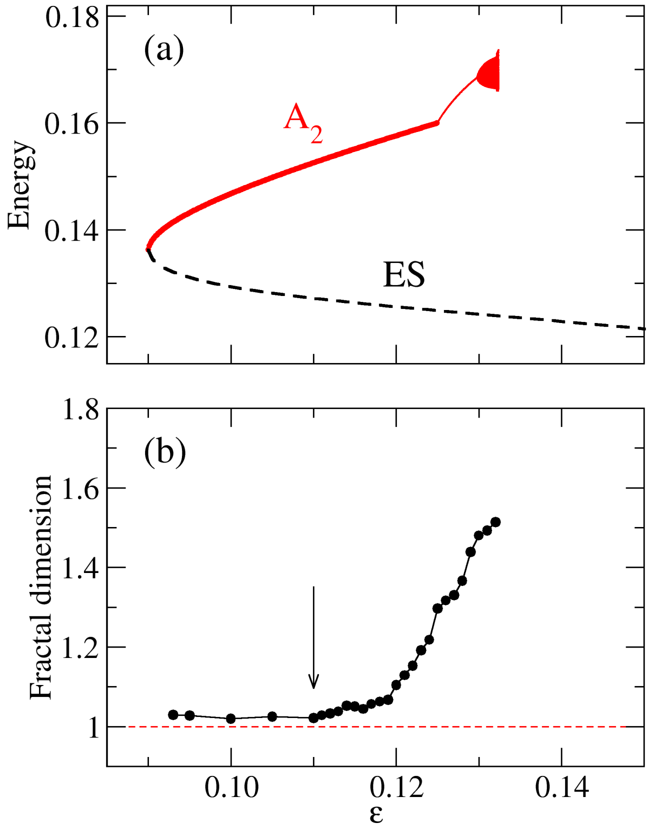

Figure 5.8 - (a) Enlargement of bifurcation diagram for attractor A_2 (red dots) and the edge state ES (dashed black line). (b) Fractal dimension of the basin boundary as a function of ϵ. For $\epsilon \gtrsim 0.11$ (indicated by the arrow) the boundary dimension begins to increase from the unity, meaning that basin boundary becomes fractal.

non–attracting chaotic set, we use the stagger–and–step method (SWEET et al., 2001) to construct arbitrarily long trajectories close to the chaotic saddle, for several values of ϵ.

First, we focus on the STCS at $\epsilon = 0.13$, soon after the smooth–to–fractal basin boundary metamorphosis. Properties of the temporal dynamics of the chaotic saddle are revealed by studying the Lyapunov exponents. The complete Lyapunov spectrum is computed from the solution obtained with the stagger–and–step, using the method by Wolf et al. (1985), described in Chapter 3. Figure 5.9 shows the temporal convergence of the positive Lyapunov exponents. We found 6 positive exponents, which means that this chaotic set is hyperchaotic. Such a large number of unstable

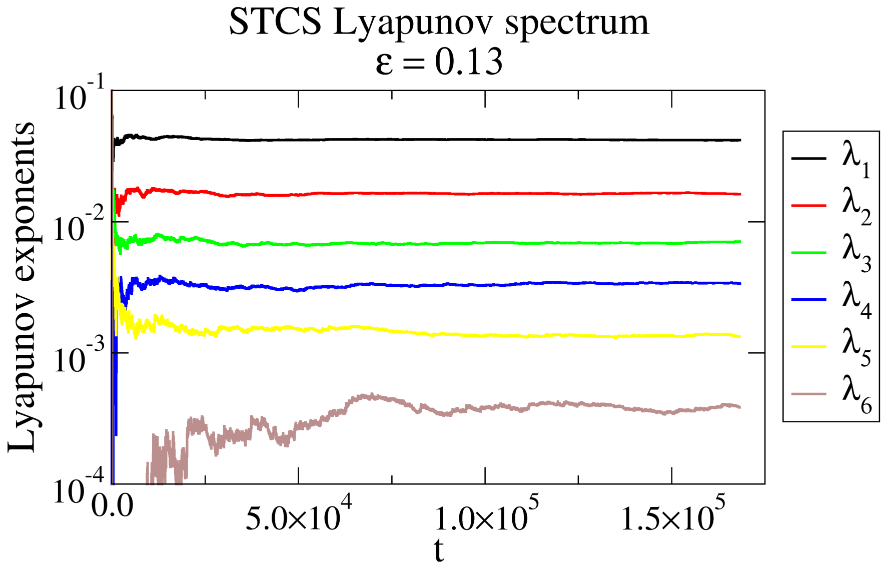

Figure 5.9 - Temporal convergence of the six positive Lyapunov exponents of the STCS chaotic saddle, for $\epsilon = 0.13$.

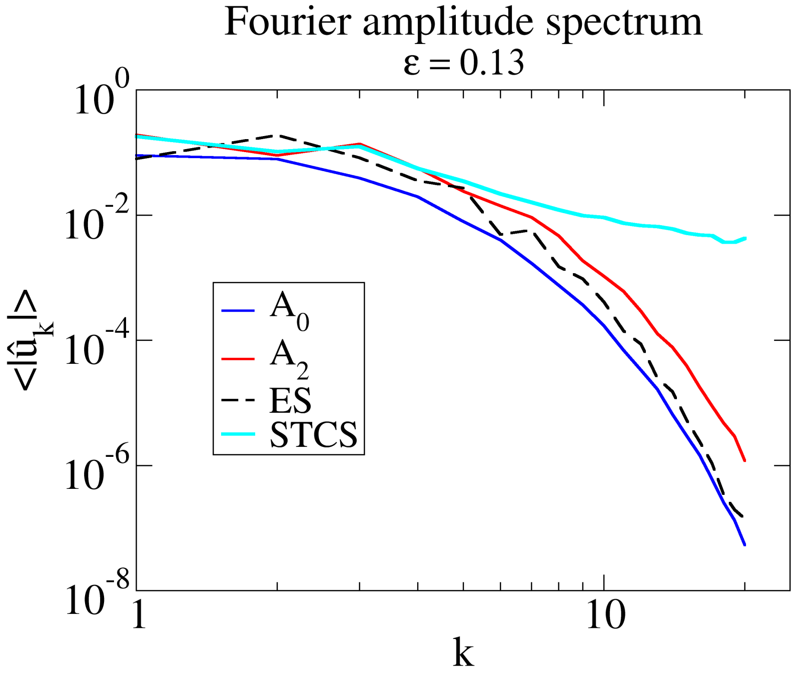

Figure 5.10 - Amplitude spectra of A_0 (blue line), A_2 (red line), ES (dashed black line) and the STCS (light blue line).

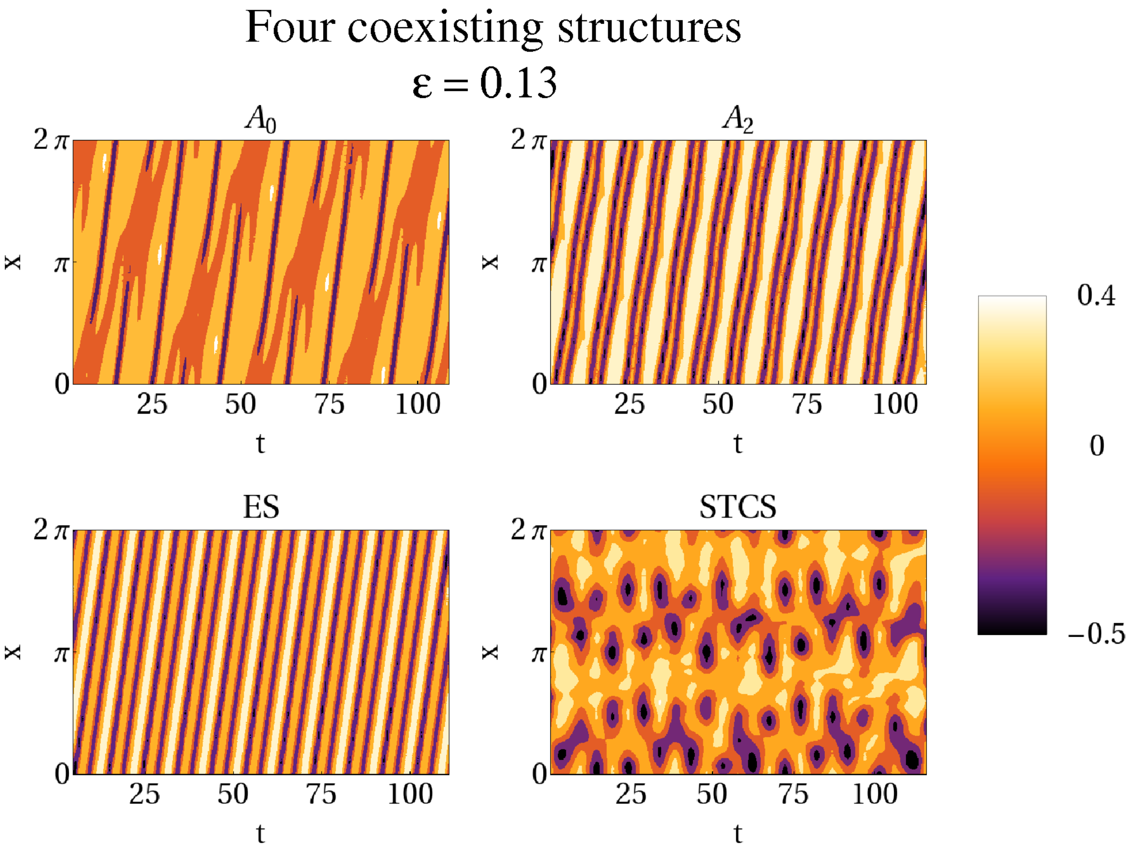

Figure 5.11 - Contourplot of the spatiotemporal evolution for the four coexisting structures at $\epsilon = 0.13$. While A_0, A_2 and ES are spatially regular, the STCS has a disordered spatiotemporal pattern.

dimensions near the homoclinic tangency is in accordance with the rapid growth of the fractal dimension of the basin boundary as a function of ϵ, as observed in Fig. 5.8(b).

The Fourier amplitude spectrum, which indicates the distribution of energy among spatial modes k, can be used to characterize the spatial properties of the chaotic saddle. Figure 5.10 shows the time–averaged amplitude spectrum of the chaotic saddle STCS (light blue line), and as a comparison, the spectra of A_0 (blue line), A_2 (red line) and ES (black dashed line). The chaotic saddle spectrum is broadband, containing much more energy in higher k modes than any other state. To illustrate the spatial disorder of the chaotic saddle, Fig. 5.11 shows spatiotemporal contourplots of the four coexisting states, obtained by the relation (5.4), in the laboratory frame. While A_0, A_2 and ES are spatially regular (SR), the chaotic saddle shows a clear spatial disorder. A quantification of spatial disorder is the Fourier power spectral

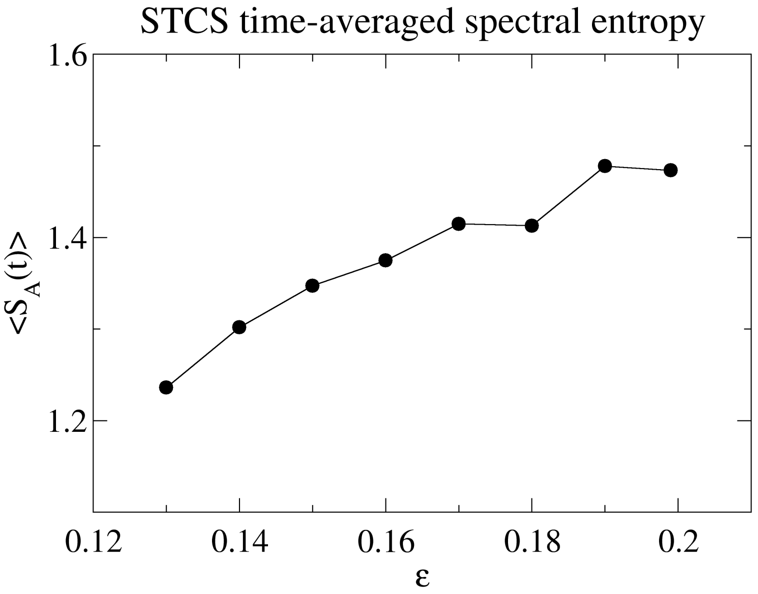

Figure 5.12 - Time–averaged spectral entropy of STCS as a function of ϵ.

entropy S_A (POWELL; PERCIVAL, 1979; XI; GUNTON, 1995), given by

$$S_A(t) = -\sum_{k=1}^{N} p_k(t) \ln p_k(t), \tag{5.25}$$

where $p_k(t)$ is the relative weight of a Fourier mode k at an instant t

$$p_k(t) = \frac{|\hat{u}_k(t)|^2}{\sum_{k=1}^{N} |\hat{u}_k(t)|^2}. \tag{5.26}$$

The spectral entropy is maximum for a random variable with uniform distribution, $p_k(t) = 1/N$ for all k. For $N = 20$, the entropy upper limit is $S_A^{\max} = \ln N \approx 3$. The index S_A has been applied to study Eq. (5.1), to characterize the transition to spatiotemporal chaos near $\epsilon \approx 0.2$ (REMPEL; CHIAN, 2007), and the level of amplitude synchronization between modes (CHIAN et al., 2010). At $\epsilon = 0.13$, the time–averaged spectral entropy of the chaotic saddle is $\langle S_A^{\mathrm{CS}}(t)\rangle = 1.233$, which represents the most disordered state if compared with spectral entropies of the two attractors, $\langle S_A^{A_0}(t)\rangle = 0.914$ and $\langle S_A^{A_2}(t)\rangle = 1.134$, and with the spectral entropy of the edge state $\langle S_A^{\mathrm{ES}}(t)\rangle = 0.937$. From all of the information exposed above, we conclude that the chaotic saddle has clear signatures of spatiotemporal chaos at $\epsilon = 0.13$.

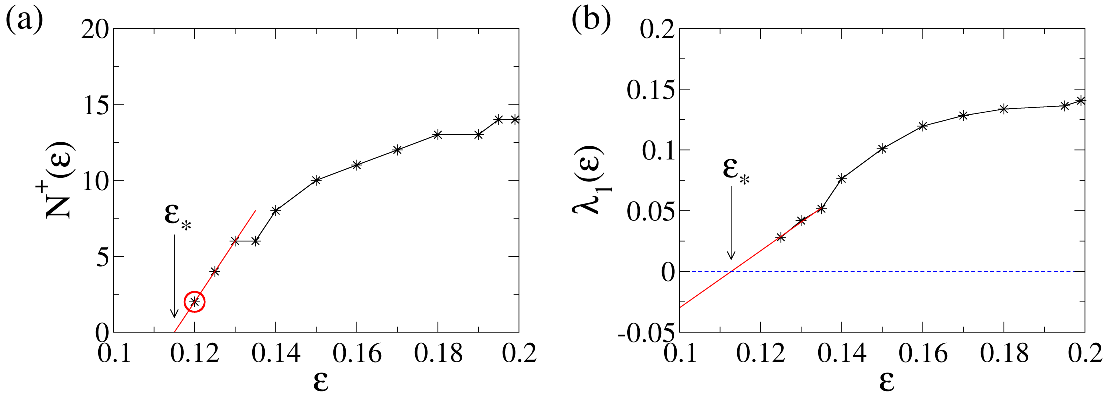

Figure 5.13 - (a) Number of positive Lyapunov exponents of STSC as a function of ϵ. (b) Maximum Lyapunov exponent of STSC as a function of ϵ.

Next, we study the dynamical evolution of STCS as the control parameter ϵ is varied. Figure 5.12 shows the variation of the time–averaged power spectral entropy $\langle S_A(t) \rangle$ for the chaotic saddle STCS as a function of ϵ. The degree of spatial disorder increses with ϵ, until it reaches the maximum value near $\epsilon \approx 0.19$. Spatial disorder and temporally chaotic dynamics have similar variations with the control parameter. Figure 5.13(a) shows the number of positive Lyapunov exponents N^+ as a function of ϵ. The number of positive Lyapunov exponents grows quickly with ϵ near the homoclinic tangency point ϵ^*, reaching its maximum value of $N^+ = 14$ at $\epsilon \approx 0.195$. The rate of growth of N^+ decreases with ϵ. Almost the same behavior is observed for the maximum Lyapunov exponent λ_1 as a function of ϵ, shown in Fig. 5.13(b). The spatiotemporal chaos associated with the STCS becomes more complex as the control parameter is increased.

We also use the information from the Lyapunov spectra to infer ϵ^*, near the moment of the genesis of STCS. For $\epsilon > 0.125$ we use the stagger–and–step method to compute the Lyapunov spectra. For $\epsilon \leq 0.125$ the transient lifetimes are too short to apply that technique. A way to estimate the number of positive Lyapunov exponents is to compute a large number of finite–time Lyapunov spectra and to take the average, as suggested by Ott (1993). The red circle in Fig. 5.13(a) marks a data point obtained this way, for $\epsilon = 0.125$. Doing a linear extrapolation with the first three data points of N^+, the genesis of STCS is estimated to occur at $\epsilon^* \approx 0.115$. A similar analysis using the maximum Lyapunov exponents λ_1 yields $\epsilon^* = 0.11274$. The information from fractal dimension of the basin boundary (Fig. 5.8(b)) and the

Lyapunov spectra are essentially in agreement.

5.6 Edge of chaos at the onset of laminar–turbulence transition

In the previous section we studied the origin of an edge state ES, given by a saddle steady wave of the RLWE, that emerges in a tangent bifurcation jointly with the attractor A_2. Also, we showed the role of the edge state ES and its stable manifold, the basin boundary, in the genesis of a spatiotemporally chaotic saddle STCS, apparently due to the tangency between the stable and unstable manifolds of the edge state. In this section we return to the edge of chaos problem, originally formulated by Skufca et al. (2006), and explored in Chapter 4 in the Pierce diode. The orginal idea of the edge of chaos was presented for the laminar–turbulence transition problem in shear flows, and it was tested using a low–dimensional Galerkin projection of the Navier–Stokes equation. The main ingredient to have an edge of chaos is the coexistence of a asymptotically laminar attracting solution with turbulent transients. These ingredients are present in the RLWE system from $\epsilon \approx 0.13235$ to $\epsilon \approx 0.2$, when one (or two) spatially regular laminar attractor (A_0 and/or A_1) coexists with a spatiotemporally chaotic saddle STCS, responsible for the turbulent transients. In this section we will show that the edge of chaos concept is helpful to understand important nonlinear phenomena such as amplitude–phase synchronization and laminar–turbulence transition, as well as to explain the two crises observed in the bifurcation diagram.

5.6.1 Edge of chaos before IC: $\epsilon = 0.199$

When attractor A_2 disappears at $\epsilon \approx 0.13235$, the necessary conditions for the existence of the edge of chaos are created: a spatially regular attractor A_0 coexists with the recently emerged spatiotemporally chaotic saddle STCS. This chaotic saddle evolves with the parameter ϵ, until it eventually exhibits, at $\epsilon = 0.199$, a maximum of fourteen positive Lyapunov exponents (see Fig. 5.13). The chaotic saddle STCS is responsible for long spatiotemporally chaotic transients. As in Chapter 4, and following main works in this area (ECKHARDT; MERSMANN, 1999; SKUFCA et al., 2006; SCHNEIDER et al., 2007), an approach to detect the edge of chaos is to compute the lifetime of initial conditions in some region of the phase space. The lifetime of an initial condition is defined as the time it takes to converge to the spatially regular attractor. Figure 5.14 shows the lifetime landscape in a two–dimensional cut of the phase space. The red region indicates short lifetime, and corresponds to initial

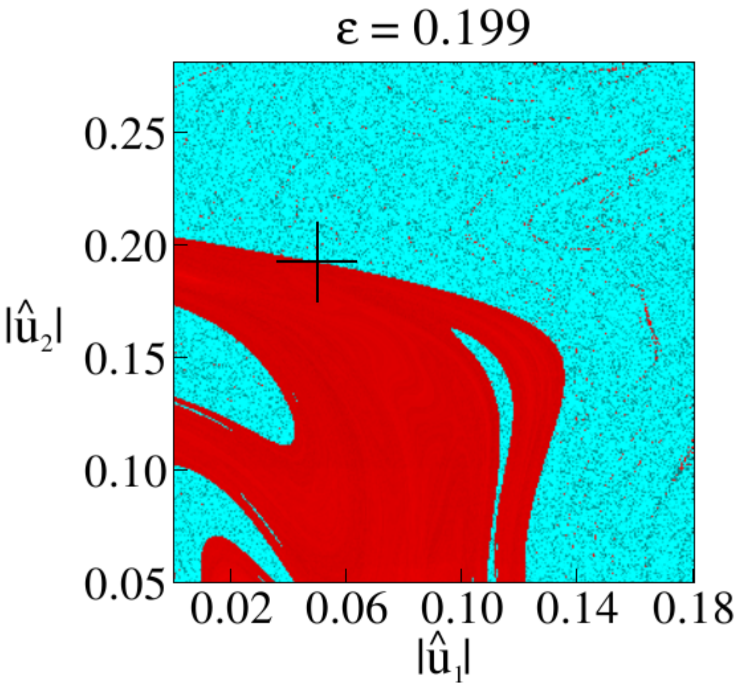

Figure 5.14 - A two–dimensional sample of phase space, showing the transient lifetime.

conditions whose trajectories do not present spatiotemporally chaotic transients, and converge to the temporally chaotic attractor A_1 quickly. On the other hand, light blue regions correspond to initial conditions whose temporal evolution presents long spatiotemporally chaotic transients before converging to A_1. A fractal boundary, the edge of chaos, separates the two regions or pseudo–basins, called laminar and turbulent pseudo–basins, respectively. As in the Pierce diode problem of Chapter 4, the stable manifold of the chaotic saddle is well approximated by the regions of longer lifetime.

The black cross in Fig. 5.14 gives the position of the edge state ES, which lies on the edge of chaos. The edge state ES is found by using the bisection method (SKUFCA et al., 2006). By integrating many different initial conditions it is possible to see that those trajectories that present chaotic transients have large energy peaks, in opposition to those that converge quickly to the attractor, with lower energy levels. Beginning with two initial conditions u_L and u_H, with short and long lifetime, respectively, we integrate the condition given by the middle point of the path that connects both conditions, $u_C = (u_L + u_H)/2$, until it converges to A_1. We use the energy level $E_0 = 0.2$ as a threshold to decide to which region the condition belongs.

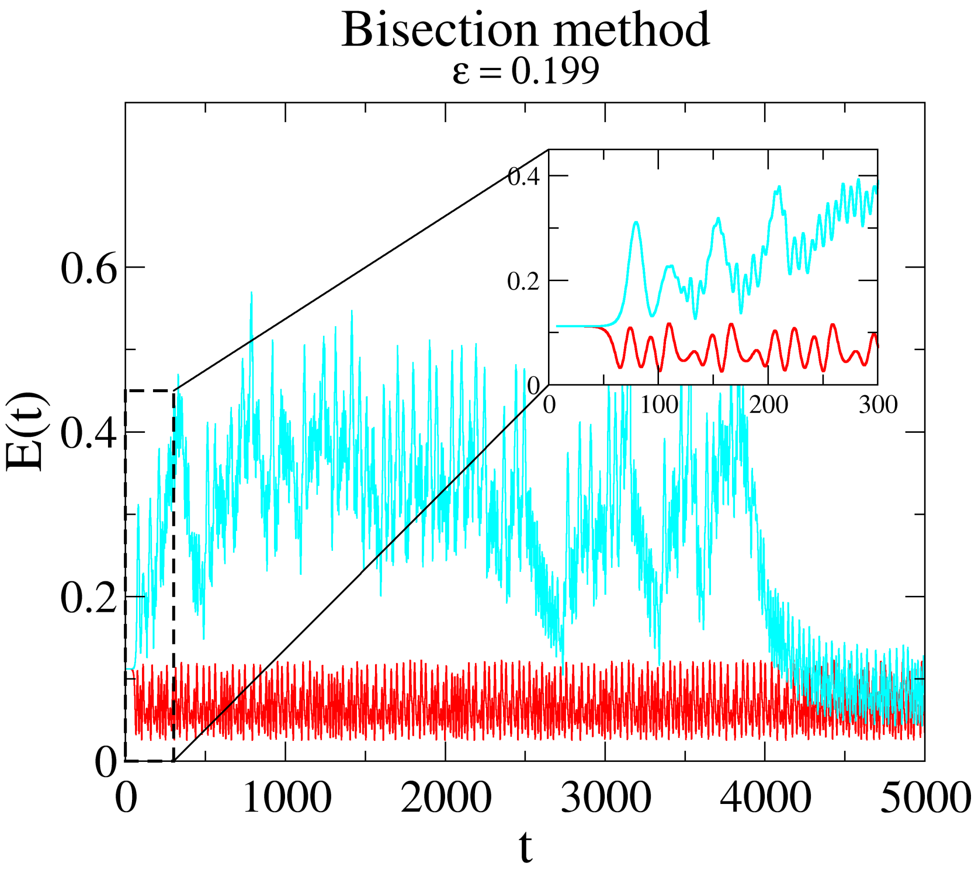

Figure 5.15 - Energy time series for two initial conditions found with the bisection method for $\epsilon = 0.199$. The initial distance is 10^{-12}. The laminar trajectory (red) converges quickly to the attractor A_1, and the turbulent trajectory (light blue) goes through the STCS regime before converging to A_1.

If the maximum energy along the trajectory of u_C is lower than E_0, the initial condition is in the laminar pseudo–basin. Otherwise, u_C belongs to the turbulent pseudo–basin. Repeating this procedure, we found pairs of conditions at both sides of the edge of chaos, arbitrarily close one to each other. Figure 5.15 is an example of two initial conditions found with the bisection method, with the distance between them $||u_L - u_H|| < 10^{-12}$. The red curve is the trajectory of laminar condition u_L, and the light blue curve is the trajectory of transient turbulent condition u_H. As the inset in Fig. 5.15 shows, both trajectories remain close to each other, with the energy being almost constant, until $t \approx 50$. That part of the solutions corresponds to trajectories passing near the edge state ES, which is a fixed point and has a constant energy. From $t \gtrsim 50$, the two trajectories separate quickly. The laminar trajectory converges immediately to the attractor, while the turbulent trajectory

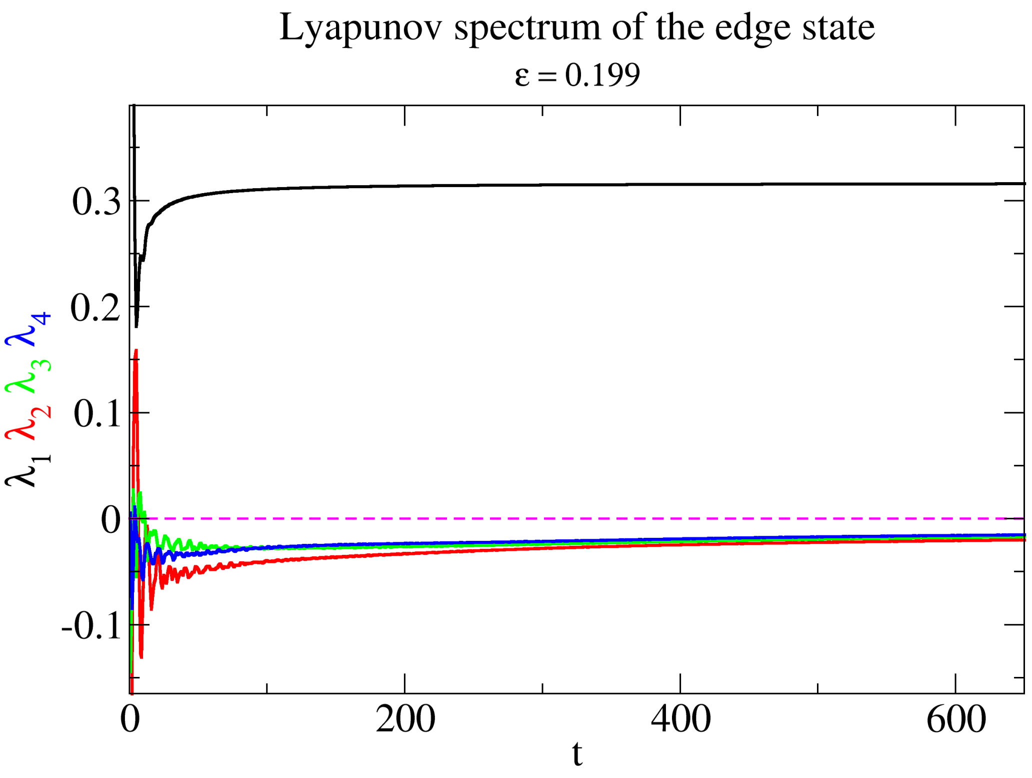

Figure 5.16 - Temporal convergence of the first four Lyapunov exponents of the edge state ES at $\epsilon = 0.199$. The edge state is a saddle fixed point, with one unstable direction and thirty–nine stable directions.

remains chaotic until it eventually converges to the attractor at $t \approx 4000$.

By systematically applying the bisection method it is possible to construct a long trajectory close to the edge state ES. This trajectory is used to compute the stability of ES. Figure 5.16 shows the temporal evolution of the first four Lyapunov exponents of the edge state. This result confirms that the edge state is a saddle structure, with one unstable direction, and thirty–nine (39) stable directions. The edge of chaos in Fig. 5.14 is a two–dimensional projection of this high–dimensional stable manifold.

5.6.2 Synchronization of A_1 and STCS with the edge state ES

As seen in Section 5.5, the turbulent state given by the STCS has little correlation in space. However, the broadband Fourier amplitude spectrum indicates strong interaction among different scales. In recent years, the concept of synchronization has been used to understand how such interactions are related to different phenomena observed in the RLWE. He and Chian (2003) studied the on–off collective imperfect phase synchronization within the fully developed spatiotemporally chaotic attractor A_3 at $\epsilon = 0.22$. They showed that bursts observed in the energy time series are highly correlated to phase synchronization events among scales. Phase synchronization due to nonlinear multi–scale interactions are responsible for the existence of coherent structures within the spatiotemporal attractor A_3. This fact has also been observed in the atmospheric turbulence at the canopy of Amazon forest (CHIAN et al., 2008) and the intermittent magnetic field turbulence of solar wind (KOGA et al., 2007; CHIAN; MIRANDA, 2009). Amplitude–phase synchronization across spatial scales was investigated by Chian et al. (2010) in order to explain the on–off intermittency between laminar and turbulent states at the onset of permanent spatiotemporally chaotic attractor A_3. They showed that the laminar (bursty) states in the on–off spatiotemporal intermittency correspond, respectively, to the nonattracting coherent structures (chaotic saddles) with higher (lower) degrees of amplitude–phase synchronization across spatial scales.

The abovementioned studies are based on the idea of self–synchronization: different scales of the same state synchronize among themselves, generating the observable effects. Here we explore the idea of synchronization between two different states: the edge state ES and some other solution of the system. Let $u(\xi, \tau)$ be the solution of Eq. (5.1) in the driver frame, for some initial condition $u(\xi, \tau_0) = u_0(\xi)$. As we have access to $N = 20$ Fourier modes, the amplitudes $\{b_k\} = \{|\hat{u}_k|\}$ and the phases $\{\phi_k\}$ in the driver frame, for $k = 1, \dots, 20$, are known for $\tau > \tau_0$. In terms of amplitudes and phases the solution can be written as

$$u(\xi, \tau) = \sum_{k=1}^{N} b_k(\tau) \cos[k\xi + \phi_k(\tau)]. \tag{5.27}$$

We are interested in measuring the level of synchronization between the solution of $u(\xi, \tau)$ and the edge state $u_E(\xi)$, previously found by the bisection method. For this purpose we introduce the distance Δ between the solution $u(\xi, \tau)$ and the edge state $u_E(x)$

$$\Delta^2(t) = \int_0^{2\pi} |u(x,t) - u_E(x)|^2 \, dx. \tag{5.28}$$

The edge state has Fourier amplitudes $\{\tilde{b}_k\}$ and phases $\{\tilde{\phi}_k\}$, with an expression in the real space similar to (5.27), then we can rewrite (5.28) as

$$\Delta^2(t) = \int_0^{2\pi} \left(\sum_{k=1}^{N} b_k \cos[kx + \phi_k] - \tilde{b}_k \cos[kx + \tilde{\phi}_k] \right)^2 dx. \tag{5.29}$$

After some algebra, and evaluating the integrals, the distance between $u(\xi, \tau)$ and $u_E(\tau)$ is given in terms of their amplitude and phase spectra,

$$\Delta^2(t) = \pi \sum_{k=1}^{N} b_k^2 + \tilde{b}_k^2 - 2 b_k \tilde{b}_k \cos[\phi_k - \tilde{\phi}_k], \tag{5.30}$$

recalling that $\tau = t$. In this case $\Delta(t)$ is a measure of both amplitude and phase synchronization between the solution $u(\xi, \tau)$ and the edge state $u_E(\xi)$. Indeed, when the amplitude and phase spectra of the solution approach to edge state spectra, Δ decreases.

He and Chian (2003) introduced a collective correlation function to measure the level of phase synchronization among scales for a spatiotemporally chaotic state in the RLWE. We want to measure phase synchronization between two states, thus we use a variation of this index, taking into account that a total phase synchronization is achieved when the argument of the cosine function in (5.30) is zero for all scales k. Using this fact, a mutual collective correlation function between two states can be defined as

$$C^{M}_{\Delta\phi}(t) = |\Pi^{M}_{k=1} \cos(\phi_k - \tilde{\phi}_k)|. \tag{5.31}$$

Perfect phase synchronization is achieved when all phases of the edge state and the solution are exactly equal, and a mutual collective correlation function is equal to one.

Figure 5.17 shows the time series of the wave energy $E(t)$, amplitude spectral entropy $S_A(t)$, distance $\Delta(t)$ and index $C^5_{\Delta\phi}(t)$ of a solution $u(\xi, \tau)$ for $\epsilon = 0.199$ and an initial condition in the turbulent pseudo–basin. The solution has a long chaotic transient, caused by the STCS, characterized by higher energy levels and rapid fluctuations. At $t \approx 3500$ the solution converges to the temporally chaotic attractor A_1, represented by lower energy levels and a bounded behavior. The amplitude spectral entropy S_A characterizes the level of self–synchronization among Fourier modes of $u(\xi, \tau)$. The red line is a running average, to facilitate visualization, also plotted for the $C_{\Delta\phi}$ time series. It is evident that the STCS regime is characterized by a lower

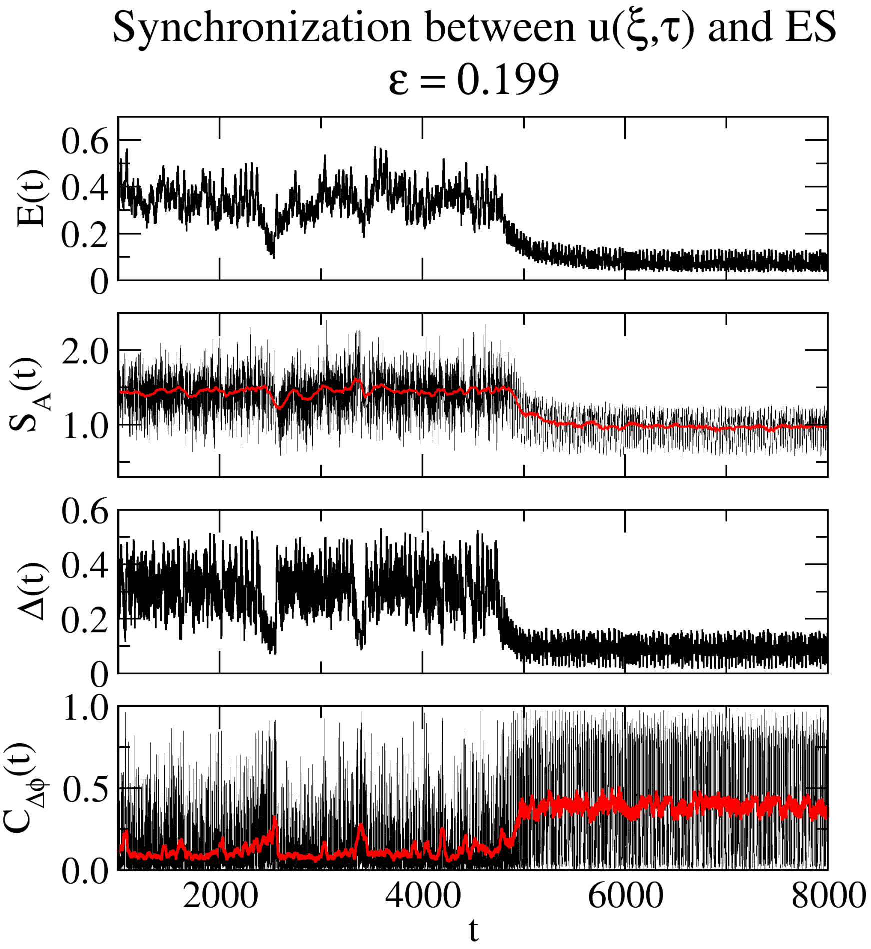

Figure 5.17 - Time series of energy $E(t)$, spectral entropy $S_A(t)$, the distance to the edge state $\Delta(t)$ and mutual collective correlation function $C_{\Delta\phi}(t)$ for an initial condition in the vicinity of STCS, showing a long chaotic transient before converging to attractor A_1. Lower and higher levels of synchronization with the edge state ES coincide with higher and lower levels of spatial disorder.

self–synchronization level (high entropy values) than the attractor A_1. This is in accordance with previous results by Chian et al. (2010). The surprising fact is that both Δ and $C_{\Delta\phi}$ show essentilly the same behavior, but this time with respect to the edge state ES. On average, STCS is more distant to ES than A_1, meaning that the chaotic attractor is more synchronized with ES in amplitude and phase than the STCS. Also, the phase synchronization between A_1 and ES is higher on average. From these results, we conclude that the dynamical evolution of solution $u(\xi, \tau)$ is, in part, controlled by its interaction with the edge state ES.

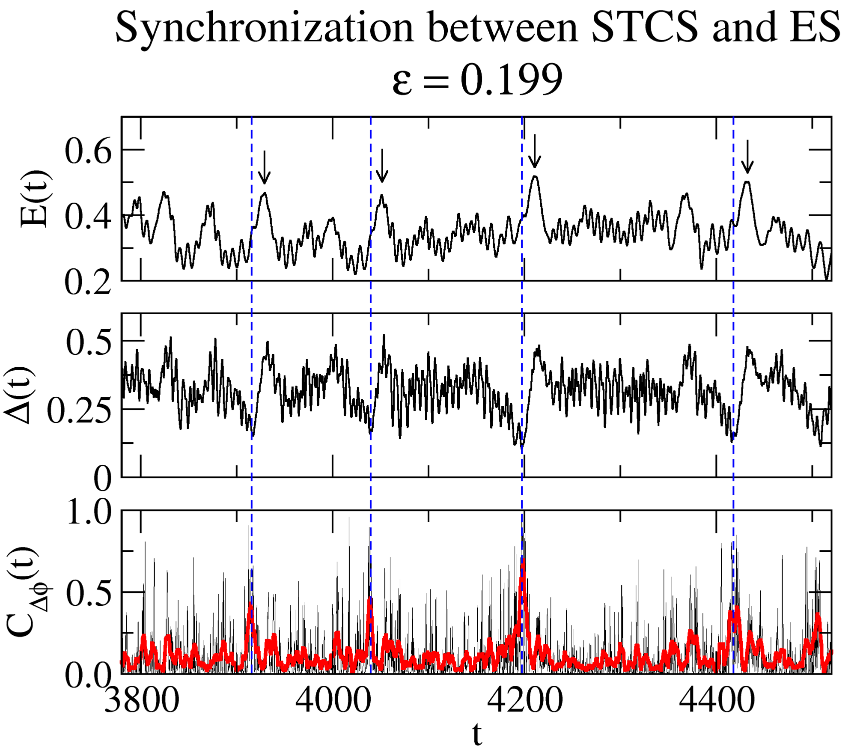

Figure 5.18 - Synchronization between ES and STCS. A solution during the transient turbulent regime synchronize with the edge state (vertical dashed blue lines) prior to the bursty release of energy (vertical arrows).

Previous analysis deals with average levels of synchronization between ES and the two stages of solution of $u(\xi, \tau)$. But by examining the STCS region of $C_{\Delta\phi}$ in Fig. 5.17, we see a local phase synchronization with ES, given by the peaks in the time series. Figure 5.18 shows an enlargement of the STCS showing some of these peaks. Vertical dashed blue lines denote four instants of high local amplitude and phase synchronization with ES. Each case is characterized by a local minimum of Δ and a pronounced peak in $C_{\Delta\phi}$ at the same time, indicating a good correlation between the events of local synchronization and the subsequent energy bursts indicated by arrows. He and Chian (2003) showed that the energy bursts within the spatiotemporally chaotic trajectory are related to higher degree of phase self–synchronization, probably associated with solitary waves (see Fig. 4 of He and Chian (2003)). We conclude that synchronization between ES and $u(\xi, \tau)$ in the STCS regime triggers the self–synchronization process, leading to an energy burst.

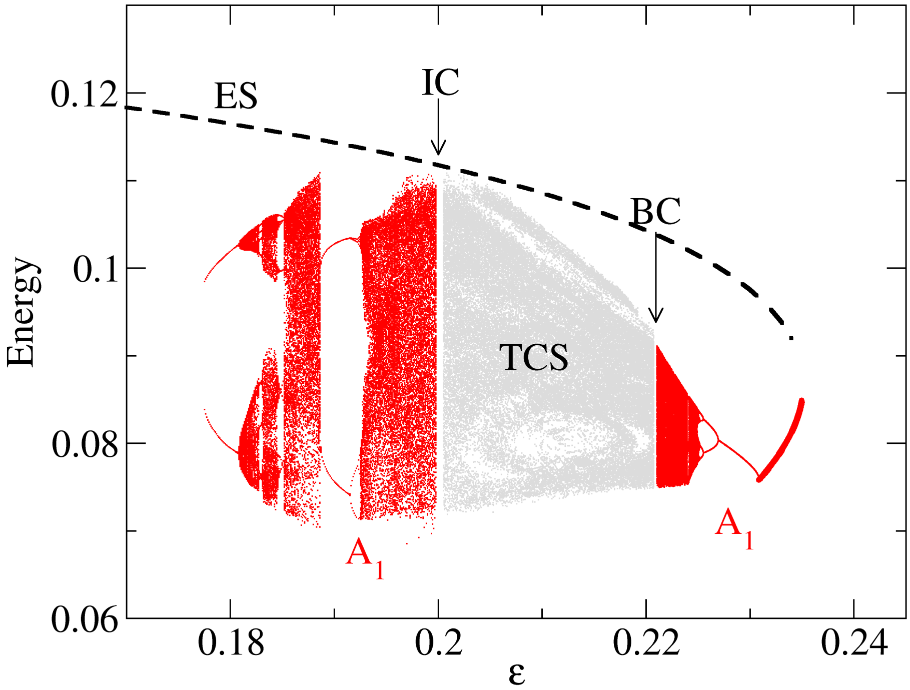

Figure 5.19 - Enlargement of the bifuraction diagram for the attractor A_1 (red), the temporally chaotic saddle TCS (grey) and the edge state ES (dashed black). Interior crisis IC and boundary crisis are indicated. Attractor A_1 is considered to be a single structure divided in the parameter space by the chaotic saddle TCS. Due to the specific Poincaré cut, it is posible to appreciate the collision between A_1 and ES that triggers the interior crisis and the transition to spatiotemporal chaos.

5.6.3 Interior and boundary crises

The bifurcation diagram of Fig. 5.4 shows two sudden transitions involving the chaotic attractor A_1: an interior crisis IC and a boundary crisis BC. In this subsection the role of the edge state in these crises is exposed. Figure 5.19 is an enlargement of the bifurcation diagram over the interval $\epsilon \in [0.17, 0.245]$, showing the bifurcations of attractor A_1 (red), including the crisis IC at $\epsilon \approx 0.1996$ and BC at $\epsilon \approx 0.22105$, the edge state ES (dashed line) and the temporally chaotic saddle TCS. In this interval the spatiotemporally chaotic saddle STCS and the spatiotemporally chaotic attractor A_3 also exist, but are not shown in Fig. 5.19.

A crisis is a parametric transition involving at least two chaotic sets and a mediating saddle point or unstable periodic orbit (UPO), and is characterized by a sudden size

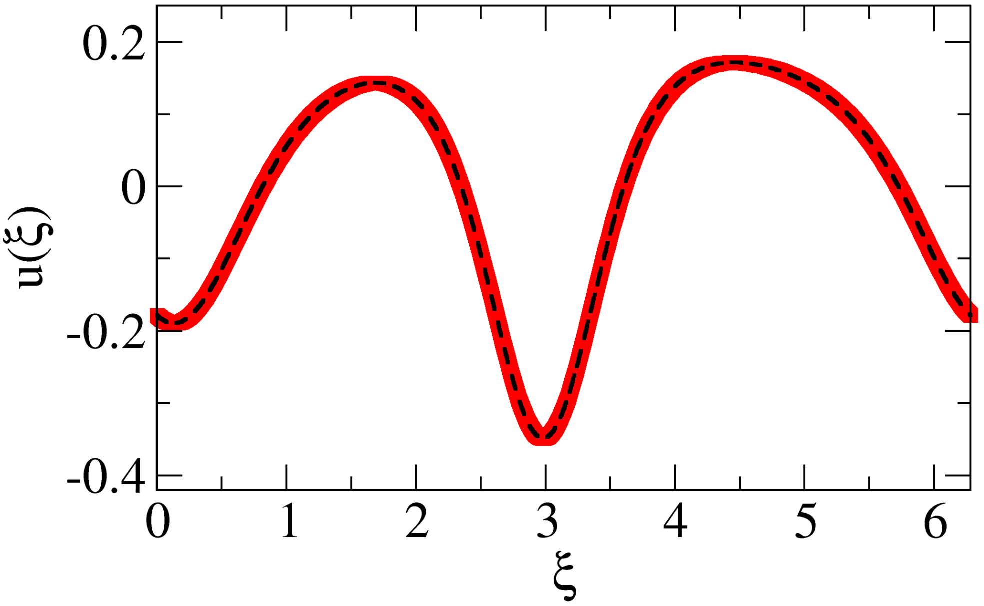

Figure 5.20 - Saddle steady wave found by He and Chian (2003) (thick red line) and edge state ES (dashed black line) plotted in the real space. Both structures are the same.

increase or a sudden disappearance of a chaotic attractor as a system parameter is varied. Crises are caused by the multiple collision between the chaotic attractor, the chaotic saddle, the saddle point and its stable manifold. In Chapters 3 and 4, we studied in detail the interior crisis involving a mediating UPO. In those cases, the chaotic saddles involved are low–dimensional in the sense of having only one positive Lyapunov exponent, representing one expanding direction. This implies that the chaotic saddles in both cases have a local planar shape in the phase space defined by the Poincaré map (see e.g. Fig. 4.6). From this fact, we could project the collision in suitable grids of initial conditions, allowing us to show direct evidence of the multiple collision, even for a spatially extended system such as the Pierce diode. For the case of the RLWE, the chaotic saddle has characteristics of spatiotemporal chaos, with fourteen expanding directions at the moment of the interior crisis. Hence, it is extremely difficult to obtain a graphical representation of the collision between the attractor and the chaotic saddle. On the other hand, it is easier to show the collision between the attractor and the mediating saddle point. As it was firt noted by He and Chian (2004), the mediating saddle structure which collides with the attractor is a saddle steady wave $u_{\mathrm{SW}}(\xi)$ in the laboratory frame, which corresponds to a

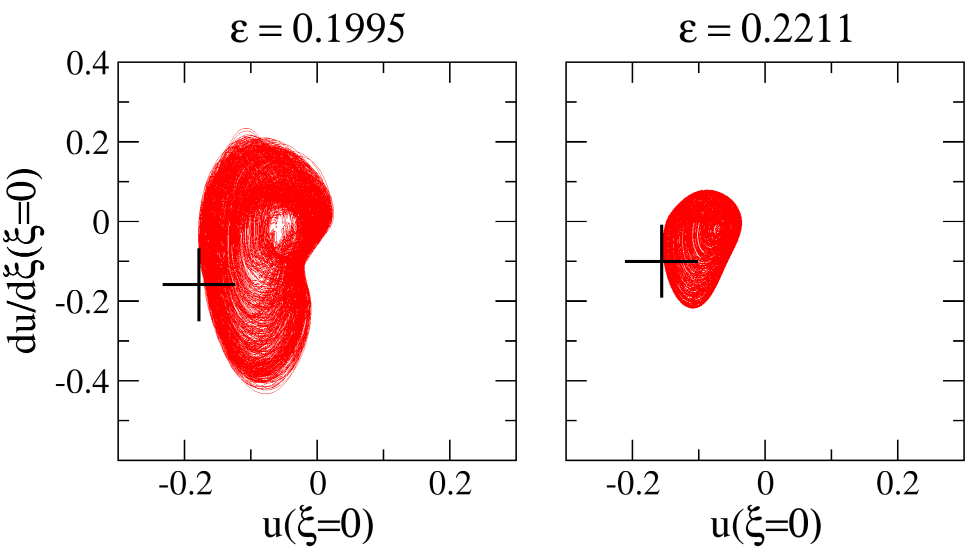

Figure 5.21 - Collisions between the attractor A_1 and ES that trigger interior and boundary crises. (a) Temporally chaotic attractor A_1 (red) and edge state ES (black cross) colliding with each other, just before the interior crisis IC preceding the transition from temporal chaos to spatiotemporal chaos. (b) Attractor A_1 and ES colliding with each other before the boundary crisis BC.

saddle fixed point in the driver frame. Imposing the condition $\partial u_{\mathrm{SW}}(\xi)/\partial\tau = 0$ and expanding the wave in the Fourier space, He and Chian (2004) found the saddle fixed point responsible for the collision. Figure 5.20 is a comparison between $u_{\mathrm{SW}}(\xi)$ (thick red line) and the edge state ES (dashed black line) found using the bisection method at $\epsilon = 0.199$. It is evident that both waves are the same structure. Consequently, the edge state ES is the saddle fixed point responsible for the interior crisis IC.

In Fig. 5.21 we plot the attractor A_1 in the real phase space $u(\xi = 0, \tau)$ vs. $\partial u(\xi = 0, \tau)/\partial\xi$ for two values of ϵ, and the edge state, denoted by a black cross. The left panel shows for $\epsilon = 0.1995$, how chaotic attractor A_1 approaches the edge state ES, just before the interior crisis IC. Due to the collision, A_1 loses its stability and becomes a temporally chaotic saddle TCS. This chaotic saddle, jointly with STCS, form the global spatiotemporally chaotic attractor A_3. These two chaotic saddles are responsible for the on–off intermittency observed after the transition (REMPEL; CHIAN, 2007; REMPEL et al., 2009a; CHIAN et al., 2010). The chaotic saddle TCS evolves as ϵ is varied, as shown in Fig. 5.19. At $\epsilon \approx 0.22105$ TCS becomes stable via a boundary crisis, reappearing as the temporally chaotic attractor A_1. This crisis is produced by a new collision involving the edge state ES. In this case, the

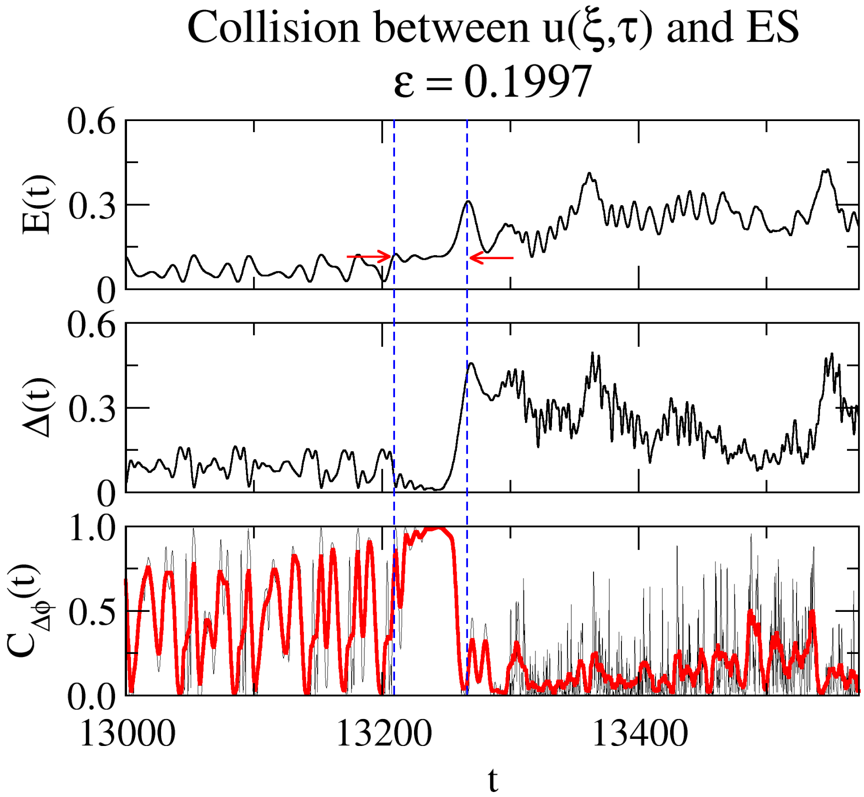

Figure 5.22 - Temporal evolution of energy $E(t)$, the distance to the edge state $\Delta(t)$ and the mutual colllective correlation function $C_{\Delta\phi}(t)$ showing the laminar–turbulence transition after the interior crisis IC. Vertical dashed blue lines denote the time interval when the collision between the solution and the edge state ES occurs. Red arrows indicate the energy level of ES.

right branch of attractor A_1 in the bifurcation diagram collides with ES when the parameter ϵ decreases. The right panel of Fig. 5.21 shows the attractor A_1 right before the collision, at $\epsilon = 0.2211$.

The collision between the edge state ES and the attractor A_1 can be analyzed in terms of synchronization between the two states. Right after the crisis, at $\epsilon = 0.1997$, an initial condition in the TCS, the region previously occupied by A_1, is integrated. After IC, the global attractor is a mixture of two chaotic saddles, TCS and STCS. Because the initial condition chosen is in the TCS, eventually the trajectory "jumps" to the STCS. Figure 5.22 shows the temporal evolution of the wave energy $E(t)$, the distance to ES $\Delta(t)$ and the mutual collective correlation $C_{\Delta\phi}$ at the moment of laminar–turbulence dynamical transition. Vertical dashed blue lines denote the interval of maximum synchronization between the solution $u(\xi, \tau)$ and the edge state ES. In this interval, energy remains almost constant, corresponding to the energy level of ES, denoted by two red arrows. Within the synchronization interval, the distance Δ reaches its minimum value and $C_{\Delta\phi}$ its maximum value, both at the same time. Right after this moment of quasi–perfect mutual synchronization, the solution is pushed out towards the spatiotemporally chaotic stage. This process explains how the edge state, in addition to mediate the laminar–turbulent transiton, is responsible for the coupling of two chaotic saddles TCS and STCS, forming the spatiotemporally chaotic attractor A_3.

6 CONCLUSION

In Chapter 2, we studied the relation between current sheets, turbulence and magnetic reconnections at the leading edge of an interplanetary coronal mass ejection. Current sheets and magnetic reconnections play a fundamental role in many regions of the heliosphere (KAMIDE; CHIAN, 2007; PASCHMANN, 2008). A statistical analysis of boundary layers of a large number of magnetic clouds indicated that magnetic cloud boundary layers (MCBL) are formed by the interaction between magnetic clouds and the ambient solar wind, which may be linked to the outer loops of an ICME and often display the properties of magnetic reconnection (WEI et al., 2003b), as confirmed by numerical simulations (SCHMIDT; CARGILL, 2003) and models (DASSO et al., 2006) of the magnetic-cloud–solar-wind interaction. In fact, magnetic reconnection exhausts have been observed at the front and rear edges of a number of ICMEs (GOSLING et al., 2005; GOSLING et al., 2007). Hence, our study of the relation between currents sheets, turbulence and magnetic reconnection in the neighborhood of a front MCBL is key to understand the dynamics and structure of ICME boundary layers, and can aid in forecasting the onset of a geomagnetic storm caused by an ICME (DU et al., 2008; ZUO et al., 2010).

We characterized for the first time the multifractal nature of a Kolmogorov magnetic turbulence at the leading edge of an ICME where two bifurcated current sheets with signatures of magnetic reconnections are found. These edge structures play a fundamental role in the dynamical processs of plasma turbulence, removing magnetic energy and accelerating particles in the sheath–cloud transition region. Our methodology can be readily applied to other turbulent boundary layers of astrophysical plasmas, such as termination and bow shocks of the heliosphere and astrospheres (STONE et al., 2008; SAHAI; CHRONOPOULOS, 2010). Further studies of the magnetic-cloud–solar-wind coupling will improve our understanding of the dynamics of star–planet relation and search for exoplanets (KIVELSON, 2007; CHIAN et al., 2010).

The basic concepts of nonlinear dynamical systems were presented in Chapter 3, and tested using a low–dimensional mean–field solar dynamo model, where the interior crisis at the end of a periodic window was characterized. The crisis–induced intermittency typically observed after the chaotic transition is explained by the collision of the a banded chaotic attractor (BCA), a surrounding chaotic saddle (SCS) and a mediating unstable periodic orbit (UPO) and its stable manifold (Fig. 3.4). When additive noise was introduced into the system, we observed noise–induced intermittency, generated by the stochastic coupling between the noisy attractor and the SCS. The maximum Lyapunov exponent follows a power law as a function of the noise level, in agreement with the theory of Lai et al. (2003). Even though rather simple, this kind of stochastic nonlinear low–dimensional models could be useful to understand the underlying mechanism governing the Maunder–type minima observed in the solar magnetic activity.

In Chapter 4, we adapted the concept of edge of chaos, a structure that separates the transient behavior from the attracting one, to analyze a low–dimensional interior crisis in the Pierce diode, a classical model for confined plasma devices. We showed that in a periodic window of that system, the edge state is the p–3 UPO that emerges from a saddle–node bifurcation at the start of the periodic window. In addition, we obtained direct evidence for the crucial role of this edge state in the interior crisis, as shown in Fig. 4.7. Also, we found a p–14 copling UPO created after the transition, via an event called explosion (ROBERT et al., 2000), linking the two chaotic saddles BCS and SCS. The observed crisis–induced intermittency is a direct consequence of the coupling between the chaotic saddles. This is the first time that a complete characterization of the interior crisis is performed in the Pierce diode.

The fundamental role played by the edge state in a number of phenomena in the regularized long wave equation (RLWE) was investigated in Chapter 2. Through the bifurcation diagram of Fig. 5.4 we see the rich variety of nonlinear dynamics of the RLWE, including steady travelling waves (SW), periodic, quasiperiodic, temporally chaotic and spatiotemporally chaotic attractors, as the driver amplitude ϵ is varied (HE, 2005; REMPEL; CHIAN, 2007).

For the interval $\epsilon \in [0.090.13235]$ two attractors A_0 and A_2 coexist. The edge state ES is a saddle steady wave with one unstable direction created at a tangent bifurcation jointly with attractor A_2. The ES and its stable manifold separate the phase space in two regions, the corresponding basins of attractions of A_0 and A_2. The stable manifold of ES coincides with basin boundary. In this scenario, the first important dynamic transition involving the ES and its stable manifold is a smooth–to–fractal basin boundary metamorphoses (Figs. 5.6 and 5.8) when $\epsilon \approx 0.11$, probably due to a homoclinic tangency between the stable and unstable manifolds of ES. From this transition a fundamental structure arises: the spatiotemporally chaotic saddle STCS, responsible for the turbulent transients. The genesis of the STCS is a key to understand the origin of the laminar–turbulence transition, since this spatiotemporal unstable coherent structure becomes stable at the transition, generating the asymptotically attracting turbulence. In Section 5.6 we address the problem of the edge of chaos at $\epsilon = 0.199$, just before the transition to turbulence. The phase space is divided in the laminar and the turbulent regions (Fig. 5.14). The boundary between these regions is the edge of chaos, which is the stable manifold of the ES. The initial conditions in the turbulent region traverse the vicinity of the STCS before decaying into the laminar attractor. We observe that even though the STCS stage is less self–synchronized, on average, than the laminar attractor (Fig. 5.17), there exists a well–defined correlation between local synchronization between the ES and the STCS, and the moments prior to a bursty release of energy (Fig. 5.18). It was shown by He and Chian (2003) that energy peaks in the STCS stage are related to higher phase self–synchronization events within the turbulent set. The explanation for this cause–effect relation could be associated to the fact that the ES has only one unstable direction. Every time the turbulent trajectory aproximates the ES (maximum mutual synchronization moment), the solution goes away along the unstable direction of the ES, which is an invariant set. At $\epsilon = 0.199$, the STCS is highly spatially uncorrelated, with fourteen positive Lyapunov exponents. But, if locally the trajectoty passes through a region of the phase space with only one positive Lyapunov exponent, the lack of correlation should decrease, increasing the level of local self–synchronization, corresponding to the energy peaks.

The collision between the temporally chaotic attractor and ES is responsible for the laminar–turbulence transition at $\epsilon \approx 0.1996$. As a consequence of this high–dimensional interior crisis, the laminar temporally chaotic attractor loses its stability and becomes a temporally chaotic saddle (TCS), which coexists with the STCS after the transition. The spatiotemporally chaotic attractor STCA created in the collision results from the coupling of the two chaotic saddles TCS and STCS. The edge state ES is responsible for this coupling.

The edge structures, such as the reconnecting current sheets observed in the fully developed turbulent leading edge of an ICME, or the saddle solutions in the Pierce diode and the RLWE, are fundamental pieces in dynamical processes associated to the transition–like phenomena. From the evidence in low–dimensional systems (Chapters 3 and 4) and a spatiotemporally chaotic system (Chapter 5), it is expected that the dynamical properties of chaotic transitions and laminar–turbulence transition are defined by the edge of chaos and the edge state. This is a significant finding since it can be used to understand more complex transitions in the space and astrophysics context, such as transitions in nonlinear dynamos (REMPEL et al., 2009b) and magnetized acretion disks (REMPEL et al., 2010).

REFERENCES

AVILA, M.; WILLIS, A. P.; HOF, B. On the transient nature of localized pipe flow turbulence. **Journal of Fluid Mechanics**, v. 646, p. 127–+, mar. 2010. 3

BARROSO, J. J.; TERRA, M. O.; MACAU, E. E. N. Bifurcation and chaos in the second oscillatory window of the classical Pierce diode. **International Journal Bifurcations and Chaos**, v. 11, p. 2579–2586, oct. 2001. 45

BENETTIN, G.; GALGANI, L.; GIORGILLI, A.; STRELCYN, J.-M. Lyapunov characteristic exponents for smooth dynamical systems and for Hamiltonian systems - a method for computing all of them. **Meccanica**, v. 15, p. 9–30, mar. 1980. 27, 47

BENZI, R.; CILIBERTO, S.; TRIPICCIONE, R.; BAUDET, C.; MASSAIOLI, F.; SUCCI, S. Extended self-similarity in turbulent flows. **Physocal Review E**, v. 48, p. 29, jul. 1993. 15

BISKAMP, D. **Magnetohydrodynamic turbulence**. Cambridge (UK): Cambridge University Press, 2003. 1

BISKAMP, D.; SCHWARZ, E.; ZEILER, A.; CELANI, A.; DRAKE, J. F. Electron magnetohydrodynamic turbulence. **Physics of Plasmas**, v. 6, p. 751–758, mar. 1999. 14

BOROVSKY, J. E. Contribution of strong discontinuities to the power spectrum of the solar wind. **Physical Review Letters**, v. 105, n. 11, p. 111102, sep. 2010. 1, 8

BOUGERET, J.-L.; PICK, M. Solar radio emissions. In: _____. **Handbook of the solar-terrestrial environment**. Berlin: Springer, 2007. p. 134. 2

BRANDENBURG, A.; NORDLUND, A. Astrophysical turbulence modeling. **Reports on Progress in Physics**, v. 74, n. 4, p. 046901, apr. 2011. 1

BRANDENBURG, A.; SUBRAMANIAN, K. Astrophysical magnetic fields and nonlinear dynamo theory. **Physics Reports**, v. 417, p. 1, oct. 2005. 29

BRUNO, R.; CARBONE, V. The solar wind as a turbulence laboratory. **Living Reviews in Solar Physics**, v. 2, p. 4, sep. 2005. 1, 8

CARGILL, P. J.; HARRA, L. K. Coronal mass ejection. In: _____. **Handbook of the solar-terrestrial environment**. Berlin: Springer, 2007. p. 118. 2, 5

CASSAK, P. A.; DRAKE, J. F.; SHAY, M. A.; ECKHARDT, B. Onset of fast magnetic reconnection. **Physical Review Letters**, v. 98, n. 21, p. 215001, may 2007. 3, 43

CHIAN, A. C.-L.; HAN, M.; MIRANDA, R. A.; SHU, C.; VALDIVIA, J. A. The planetary-exoplanetary environment: a nonlinear perspective. **Advances in Space Research**, v. 46, p. 472–484, aug. 2010. 89

CHIAN, A. C.-L.; MIRANDA, R. A. Cluster and ACE observations of phase synchronization in intermittent magnetic field turbulence: a comparative study of shocked and unshocked solar wind. **Annales Geophysicae**, v. 27, p. 1789, apr. 2009. 5, 16, 79

CHIAN, A. C.-L.; MIRANDA, R. A.; KOGA, D.; BOLZAN, M. J. A.; RAMOS, F. M.; REMPEL, E. L. Analysis of phase coherence in fully developed atmospheric turbulence: Amazon forest canopy. **Nonlinear Processes in Geophysics**, v. 15, p. 567–573, jul. 2008. 79

CHIAN, A. C.-L.; MIRANDA, R. A.; REMPEL, E. L.; SAIKI, Y.; YAMADA, M. Amplitude-phase synchronization at the onset of permanent spatiotemporal chaos. **Physical Review Letters**, v. 104, n. 25, p. 254102, jun. 2010. 16, 27, 58, 67, 73, 79, 81, 85

CHIAN, A. C. L.; MUÑOZ, P. R. Detection of current sheets and magnetic reconnections at the turbulent leading edge of an interplanetary coronal mass ejection. **Astropysical Journal Letters**, v. 733, p. L34, 2011. 1, 2, 13, 14, 17, 20, 21, 22

CHIAN, A. C.-L.; SANTANA, W. M.; REMPEL, E. L.; BOROTTO, F. A.; HADA, T.; KAMIDE, Y. Chaos in driven Alfvén systems: unstable periodic orbits and chaotic saddles. **Nonlinear Proc. Geophys.**, v. 14, p. 17–29, jan. 2007. 52

COVAS, E.; TAVAKOL, R. Crisis-induced intermittency in truncated mean field dynamos. **Physical Review E**, v. 55, p. 6641–6645, jun. 1997. 25, 31, 38

DASSO, S.; MANDRINI, C. H.; DÉMOULIN, P.; LUONI, M. L. A new model-independent method to compute magnetic helicity in magnetic clouds. **Astronomy and Astrophysics**, v. 455, p. 349–359, aug. 2006. 89

DATTA, S. K.; KUMAR, L.; BASU, B. Pierce-type one-dimensional Eulerian hydrodynamic analysis of a plasma-filled helix traveling-wave tube. **IEEE Transactions on Electron Devices**, v. 58, p. 882–890, mar. 2011. 45

DU, A. M.; TSURUTANI, B. T.; SUN, W. Anomalous geomagnetic storm of 21-22 January 2005: a storm main phase during northward IMFs. **Journal of Geophysical Research (Space Physics)**, v. 113, p. A10214, oct. 2008. 5, 89

DUNLOP, M. W.; BALOGH, A.; MEIER, K.-H. G.; ROBERT, P. Four-point Cluster application of magnetic field analysis tools: the curlometer. **Journal of Geophysical Research**, v. 107, p. 1384, nov. 2002. xiv, 19, 20

ECKHARDT, B. Open problem: turbulence transition in pipe flow: some open questions. **Nonlinearity**, v. 21, p. 1, jan. 2008. 2

ECKHARDT, B.; MERSMANN, A. Transition to turbulence in a shear flow. **Physical Review E**, v. 60, p. 509, jul. 1999. 75

FEIGENBAUM, M. J. The universal metric properties of nonlinear transformations. **Journal of Statistical Physics**, v. 21, p. 669–706, dec. 1979. 32

FOULLON, C.; OWEN, C. J.; DASSO, S.; GREEN, L. M.; DANDOURAS, I.; ELLIOTT, H. A.; FAZAKERLEY, A. N.; BOGDANOVA, Y. V.; CROOKER, N. U. Multi-spacecraft study of the 21 January 2005 ICME. Evidence of current sheet substructure near the periphery of a strongly expanding, fast magnetic cloud. **Solar Physics**, v. 244, p. 139–165, aug. 2007. 5, 6

FRISCH, U. **Turbulence**: the legacy of A. N. Kolmogorov. Cambridge (UK): Cambridge University Press, 1995. 1

GOLDREICH, P.; SRIDHAR, S. Toward a theory of interstellar turbulence. 2: strong alfvenic turbulence. **Astrophysical Journal**, v. 438, p. 763–775, jan. 1995. 18

GOSLING, J. T.; ERIKSSON, S.; MCCOMAS, D. J.; PHAN, T. D.; SKOUG, R. M. Multiple magnetic reconnection sites associated with a coronal mass ejection in the solar wind. **Journal of Geophysical Research**, v. 112, p. A08106, aug. 2007. 1, 2, 8, 21, 22, 89

GOSLING, J. T.; SKOUG, R. M.; MCCOMAS, D. J.; SMITH, C. W. Direct evidence for magnetic reconnection in the solar wind near 1 AU. **Journal of**

Geophysical Research, v. 110, p. A01107, jan. 2005. xiv, 1, 2, 8, 18, 19, 21, 22, 89

GREBOGI, C.; MCDONALD, S. W.; OTT, E.; YORKE, J. A. Final state sensitivity: an obstruction to predictability. **Physics Letters A**, v. 99, p. 415, dec. 1983. 68

GREBOGI, C.; OTT, E.; YORKE, J. A. Crises, sudden changes in chaotic attractors, and transient chaos. **Physica D**, v. 7, p. 181–200, may 1983. 35, 52

_____. Basin boundary metamorphoses: changes in accessible boundary orbits. **Physica D Nonlinear Phenomena**, v. 24, p. 243, jan. 1987. 68

HE, K. Riddling of the orbit in a high dimensional torus and intermittent energy bursts in a nonlinear wave system. **Physical Review Letters**, v. 94, n. 3, p. 034101, jan. 2005. 58, 59, 64, 90

HE, K.; CHIAN, A. C.-L. On-off collective imperfect phase synchronization and bursts in wave energy in a turbulent state. **Physical Review Letters**, v. 91, n. 3, p. 034102, jul. 2003. xix, 58, 67, 79, 80, 82, 84, 91

_____. Critical dynamic events at the crisis of transition to spatiotemporal chaos. **Physical Review E**, v. 69, n. 2, p. 026207, feb. 2004. 84, 85

HE, K.; SALAT, A. Hysteresis and onset of chaos in periodically driven nonlinear drift waves. **Plasma Physics and Controlled Fusion**, v. 31, p. 123, jan. 1989. 58

HOF, B.; LOZAR, A. de; KUIK, D. J.; WESTERWEEL, J. Repeller or attractor? Selecting the dynamical model for the onset of turbulence in pipe flow. **Physical Review Letters**, v. 101, n. 21, p. 214501, nov. 2008. 3

HOSHINO, M.; NISHIDA, A.; MUKAI, T.; SAITO, Y.; YAMAMOTO, T.; KOKUBUN, S. Structure of plasma sheet in magnetotail: double-peaked electric current sheet. **Journal of Geophysical Research**, v. 1012, p. 24775–24786, nov. 1996. 23

HOYT, D. V.; SCHATTEN, K. H. **The role of the sun in climate change**. New York: Oxford University Press, 1997. 32

HRAMOV, A. E.; KORONOVSKII, A. A.; REMPEN, I. S. Controlling chaos in spatially extended beam-plasma system by the continuous delayed feedback. **Chaos**, v. 16, n. 1, p. 013123, mar. 2006. 45

HSU, G.-H.; OTT, E.; GREBOGI, C. Strange saddles and the dimensions of their invariant manifolds. **Physics Letters A**, v. 127, p. 199–204, feb. 1988. 28, 52

HUDSON, P. D. Discontinuities in an anisotropic plasma and their identification in the solar wind. **Planetary and Space Science**, v. 18, p. 1611–1622, nov. 1970. 19

KAMIDE, Y.; CHIAN, A. C.-L. **Handbook of the solar-terrestrial environment**. Berlin: Springer, 2007. 89

KANTZ, H.; GRASSBERGER, P. Repellers, semi-attractors, and long-lived chaotic transients. **Physica D**, v. 17, p. 75–86, aug. 1985. 28

KIVELSON, M. G. Planetary magnetospheres. In: _____. **Handbook of the solar-terrestrial environment**. Berlin: Springer, 2007. p. 470. 89

KLOEDEN, P. E.; PLATEN, E. **Numerical solution of stochastic differential equations**. Berlin, Germany: Springer-Verlag, 1992. 38

KOGA, D.; CHIAN, A. C.-L.; MIRANDA, R. A.; REMPEL, E. L. Intermittent nature of solar wind turbulence near the Earth's bow shock: phase coherence and non-Gaussianity. **Physical Review E**, v. 75, n. 4, p. 046401, apr. 2007. 16, 79

KOLMOGOROV, A. The local structure of turbulence in incompressible viscous fluid for very large reynolds numbers. **Akademiia Nauk SSSR Doklady**, v. 30, p. 301, 1941. 1

LAI, Y.; TÉL, T. **Transient Chaos: complex dynamics on finite-time scales**. [S.l.]: Springer, 2011. (APPLIED MATHEMATICAL SCIENCES). ISBN 9781441969866. xviii, 68, 69

LAI, Y.-C.; LIU, Z.; BILLINGS, L.; SCHWARTZ, I. B. Noise-induced unstable dimension variability and transition to chaos in random dynamical systems. **Physical Review E**, v. 67, n. 2, p. 026210, feb. 2003. 25, 38, 41, 90

LANG, K. R. **The Sun from space**. Berlin: Springer-Verlag, 2009. 6

LATHROP, D. P.; KOSTELICH, E. J. Characterization of an experimental strange attractor by periodic orbits. **Physical Review A**, v. 40, p. 4028–4031, oct. 1989. 55

LAWSON, W. S. The Pierce diode with an external circuit. I. Oscillations about nonuniform equilibria. **Physics of Fluids**, v. 1, p. 1483–1492, jul. 1989. 44, 45, 47

LEAMON, R. J.; SMITH, C. W.; NESS, N. F. Characteristics of magnetic fluctuations within coronal mass ejections: The January 1997 event. **Geophysical Research Letters**, v. 25, p. 2505–2508, 1998. 5

LI, G. Identifying current-sheet-like structures in the solar wind. **Astrophysical Journal Letters**, v. 672, p. L65–L68, jan. 2008. xiii, 1, 2, 8, 9

LIU, R.; LEE, J.; WANG, T.; STENBORG, G.; LIU, C.; WANG, H. A reconnecting current sheet imaged in a solar flare. **Astrophysical Journal Letters**, v. 723, p. L28–L33, nov. 2010. 2, 8

LIU, Y.; RICHARDSON, J. D.; BELCHER, J. W.; KASPER, J. C.; ELLIOTT, H. A. Thermodynamic structure of collision-dominated expanding plasma: heating of interplanetary coronal mass ejections. **Journal of Geophysical Research**, v. 111, p. A01102, jan. 2006. 5

LORENZ, E. N. Deterministic nonperiodic flow. **Journal of Atmospheric Sciences**, v. 20, p. 130–148, mar. 1963. 2, 31

MATSUMOTO, H.; YOKOYAMA, H.; SUMMERS, D. Computer simulations of the chaotic dynamics of the Pierce beam-plasma system. **Physics of Plasmas**, v. 3, p. 177–191, jan. 1996. 46, 47

MININNI, P. D.; GOMEZ, D. O.; MINDLIN, G. B. Simple model of a stochastically excited solar dynamo. **Solar Physics**, v. 201, p. 203–223, 2001. 25

MIRANDA, R. A.; CHIAN, A. C.-L.; DASSO, S.; ECHER, E.; NOZ, P. R. M.; TRIVEDI, N. B.; TSURUTANI, B. T.; YAMADA, M. Observation of non-Gaussianity and phase synchronization in intermittent magnetic field turbulence in the solar-terrestrial environment. In: A. G. Kosovichev, A. H. Andrei, & J.-P. Roelot (Ed.). **IAU Symposium**. [S.l.: s.n.], 2010. (IAU Symposium, v. 264), p. 363–368. 5

MOZER, F. S.; ANGELOPOULOS, V.; BONNELL, J.; GLASSMEIER, K. H.; MCFADDEN, J. P. THEMIS observations of modified Hall fields in asymmetric magnetic field reconnection. **Geophysical Research Letters**, v. 351, p. L17S04, apr. 2008. 22

MÜLLER, W.-C.; BISKAMP, D. Scaling properties of three-dimensional magnetohydrodynamic turbulence. **Physical Review Letters**, v. 84, p. 475–478, jan. 2000. 17

MÜLLER, W.-C.; BISKAMP, D.; GRAPPIN, R. Statistical anisotropy of magnetohydrodynamic turbulence. **Physical Review E**, v. 67, n. 6, p. 066302, jun. 2003. 17

MUÑOZ, P. R.; CHIAN, A. C.-L.; MIRANDA, R. A.; YAMADA, M. Observation of magnetic reconnection and current sheets in the solar wind. In: A. G. Kosovichev, A. H. Andrei, & J.-P. Roelot (Ed.). **IAU Symposium**. [S.l.: s.n.], 2010. (IAU Symposium, v. 264), p. 369–372. 5, 6

NISHIDA, A. Magnetic reconnection. In: _____. **Handbook of the solar-terrestrial environment**. Berlin: Springer, 2007. p. 280. 2, 18

OTT, E. **Chaos in dynamical systems**. [S.l.: s.n.], 1993. 74

PASCHMANN, G. Recent in-situ observations of magnetic reconnection in near-Earth space. **Geophysical Research Letters**, v. 351, p. L19109, oct. 2008. 89

PHAN, T. D.; GOSLING, J. T.; DAVIS, M. S.; SKOUG R. M. ANDØIEROSET, M.; LIN, R. P.; LEPPING, R. P.; MCCOMAS, D. J.; SMITH, C. W.; REME, H.; BALOGH, A. A magnetic reconnection X-line extending more than 390 Earth radii in the solar wind. **Nature**, v. 439, p. 175–178, jan. 2006. 1, 2, 8, 21, 22

PIERCE, J. R. Limiting stable current in electron beams in the presence of ions. **Journal of Applied Physics**, v. 15, p. 721, oct. 1944. 45, 46

POLITANO, H.; POUQUET, A. Model of intermittency in magnetohydrodynamic turbulence. **Physical Review E**, v. 52, p. 636–641, jul. 1995. 15, 17

POWELL, G. E.; PERCIVAL, I. C. A spectral entropy method for distinguishing regular and irregular motion of Hamiltonian systems. **Journal of Physics A Mathematical General**, v. 12, p. 2053, nov. 1979. 73

PRIEST, E. R. Solar atmosphere. In: _____. **Handbook of the solar-terrestrial environment**. Berlin: Springer, 2007. p. 56–. 2, 18

REMPEL, E. L.; CHIAN, A. C.-L. Origin of transient and intermittent dynamics in spatiotemporal chaotic systems. **Physical Review Letters**, v. 98, n. 1, p. 014101, jan. 2007. 27, 43, 58, 64, 67, 73, 85, 90

REMPEL, E. L.; CHIAN, A. C.-L.; KOGA, D.; MIRANDA, R. A.; SANTANA, W. M. Alfvén complexity. **International Journal of Bifurcation and Chaos**, v. 8, n. 16, p. 1697–1703, 2008. 25

REMPEL, E. L.; CHIAN, A. C.-L.; MACAU, E. E. N.; ROSA, R. R. Analysis of chaotic saddles in high-dimensional dynamical systems: The Kuramoto-Sivashinsky equation. **Chaos**, v. 14, p. 545–556, sep. 2004. 27, 43, 53

_____. Analysis of chaotic saddles in low-dimensional dynamical systems: the derivative nonlinear Schrödinger equation. **Physica D**, v. 199, p. 407–424, dec. 2004. 27, 35

REMPEL, E. L.; LESUR, G.; PROCTOR, M. R. E. Supertransient magnetohydrodynamic turbulence in Keplerian shear flows. **Physical Review Letters**, v. 105, n. 4, p. 044501, jul. 2010. 3, 43, 92

REMPEL, E. L.; MIRANDA, R. A.; CHIAN, A. C.-L. Spatiotemporal intermittency and chaotic saddles in the regularized long-wave equation. **Physics of Fluids**, v. 21, n. 7, p. 074105, jul. 2009. 57, 67, 85

REMPEL, E. L.; PROCTOR, M. R. E.; CHIAN, A. C.-L. A novel type of intermittency in a non-linear dynamo in a compressible flow. **Monthly Notices of the Royal Astronomical Society**, v. 400, p. 509, nov. 2009. 92

REMPEL, E. L.; SANTANA, W. M.; CHIAN, A. C.-L. Alfvén multistability: transient and intermittent dynamics induced by noise. **Physics of Plasmas**, v. 13, n. 3, p. 032308, mar. 2006. 25

RETINÒ, A.; SUNDKVIST, D.; VAIVADS, A.; MOZER, F.; ANDRÉ, M.; OWEN, C. J. In situ evidence of magnetic reconnection in turbulent plasma. **Nature Physics**, v. 3, p. 236–238, apr. 2007. 23

ROBERT, C.; ALLIGOOD, K. T.; OTT, E.; YORKE, J. A. Explosions of chaotic sets. **Physica D**, v. 144, p. 44–61, sep. 2000. 37, 55, 90

SAHAI, R.; CHRONOPOULOS, C. K. The astrosphere of the asymptotic giant branch star IRC+10216. **Astrophysical Journal Letters**, v. 711, p. L53–L56, mar. 2010. 89

SCHMALZ, S.; STIX, M. An α-Ω dynamo with order and chaos. **Astronomy and Astrophysics**, v. 245, p. 654–661, may 1991. 25, 29, 31

SCHMIDT, J. M.; CARGILL, P. J. Magnetic reconnection between a magnetic cloud and the solar wind magnetic field. **Journal of Geophysical Research**, v. 108, p. 1023, jan. 2003. 89

SCHMIEGEL, A.; ECKHARDT, B. Fractal stability border in plane couette flow. **Physical Review Letters**, v. 79, n. 26, p. 5250, Dec 1997. 3

SCHNEIDER, T. M.; ECKHARDT, B.; YORKE, J. A. Turbulence transition and the edge of chaos in pipe flow. **Physical Review Letters**, v. 99, n. 3, p. 034502, jul. 2007. 3, 43, 75

SHE, Z.-S.; LEVEQUE, E. Universal scaling laws in fully developed turbulence. **Physical Review Letters**, v. 72, p. 336–339, jan. 1994. 16, 17

SKUFCA, J. D.; YORKE, J. A.; ECKHARDT, B. Edge of chaos in a parallel shear flow. **Physical Review Letters**, v. 96, n. 17, p. 174101, may 2006. 3, 43, 50, 53, 75, 76

SOLANKI, S. K.; INHESTER, B.; SCHÜSSLER, M. The solar magnetic field. **Reports on Progress in Physics**, v. 69, p. 563–668, mar. 2006. 29

SONNERUP, B. U. O.; CAHILL JR., L. J. Magnetopause structure and attitude from Explorer 12 observations. **Journal of Geophysical Research**, v. 72, p. 171, jan. 1967. 20

SONNERUP, B. U. O.; PASCHMANN, G.; PAPAMASTORAKIS, I.; SCKOPKE, N.; HAERENDEL, G.; BAME, S. J.; ASBRIDGE, J. R.; GOSLING, J. T.; RUSSELL, C. T. Evidence for magnetic field reconnection at the Earth's magnetopause. **Journal Geophysical Research**, v. 861, p. 10049–10067, nov. 1981. xiv, 19, 20, 21

SOON, W. H.; BALIUNAS, S. L.; ZHANG, Q. An interpretation of cycle periods of stellar chromospheric activity. **Astrophysical Journal**, v. 414, p. L33–L36, 1993. 32

STONE, E. C.; CUMMINGS, A. C.; MCDONALD, F. B.; HEIKKILA, B. C.; LAL, N.; WEBBER, W. R. An asymmetric solar wind termination shock. **Nature**, v. 454, p. 71–74, jul. 2008. 89

SWEET, D.; NUSSE, H. E.; YORKE, J. A. Stagger-and-step method: detecting and computing chaotic saddles in higher dimensions. **Physical Review Letters**, v. 86, p. 2261, mar. 2001. 28, 70

SZABÓ, K. G.; LAI, Y.-C.; TÉL, T.; GREBOGI, C. Topological scaling and gap filling at crisis. **Physical Review E**, v. 61, p. 5019–5032, may 2000. 37, 55

TÉL, T.; LAI, Y.-C. Chaotic transients in spatially extended systems. **Physics Reports**, v. 460, p. 245–275, may 2008. 3

TERRA, M. O. Biparametric equilibria bifurcations of the Pierce diode: a one-dimensional plasma-filled device. **Physics of Plasmas**, v. 18, n. 3, p. 033105, mar. 2011. 45

TOBIAS, S. M. The solar dynamo. **Royal Society of London Philosophical Transactions Series A**, v. 360, p. 2741–2756, 2002. 32

TREUMANN, R. A.; BAUMJOHANN, W. **Advanced space plasma physics**. London: Imperial College Press, 1997. 45

TRUBETSKOV, D. I.; MCHEDLOVA, E. S.; ANFINOGENTOV, V. G.; PONOMARENKO, V. I.; RYSKIN, N. M. Nonlinear waves, chaos and patterns in microwave electronic devices. **Chaos**, v. 6, p. 358–367, sep. 1996. 44

VELTRI, P. MHD turbulence in the solar wind: self-similarity, intermittency and coherent structures. **Plasma Physics and Controlled Fusion**, v. 41, p. A787–A795, mar. 1999. 1, 8

VOLLMER, J.; SCHNEIDER, T. M.; ECKHARDT, B. Basin boundary, edge of chaos and edge state in a two-dimensional model. **New J. Phys.**, v. 11, n. 1, p. 013040, jan. 2009. 43

VÖRÖS, Z.; LEUBNER, M. P.; BAUMJOHANN, W. Cross-scale coupling-induced intermittency near interplanetary shocks. **Journal of Geophysical Research**, v. 111, p. A02102, feb. 2006. 2

WEI, F.; HU, Q.; FENG, X.; FAN, Q. Magnetic reconnection phenomena in interplanetary space. **Space Sciences Review**, v. 107, p. 107–110, apr. 2003. 2

WEI, F.; LIU, R.; FAN, Q.; FENG, X. Identification of the magnetic cloud boundary layers. **Journal of Geophysical Research**, v. 108, p. 1263, jun. 2003. 2, 89

WEISS, N. O.; CATTANEO, F.; JONES, C. A. Periodic and aperiodic dynamo waves. **Geophysical and Astrophysical Fluid Dynamics**, v. 30, p. 305–341, 1984. 25

WELCH, P. D. The use of fast Fourier transform for the estimation of power spectra: a method based on time averaging over short, modified periodograms. **IEEE Transactions on Audio & Electroacoustics**, v. 15, p. 70–73, 1967. 13

WILLIS, A. P.; KERSWELL, R. R. Critical behavior in the relaminarization of localized turbulence in pipe flow. **Physical Review Letters**, v. 98, n. 1, p. 014501, jan. 2007. 3

WOLF, A.; SWIFT, J. B.; SWINNEY, H. L.; VASTANO, J. A. Determining Lyapunov exponents from a time series. **Physica D**, v. 16, p. 285–317, jul. 1985. 27, 70

XI, H.; GUNTON, J. D. Spatiotemporal chaos in a model of Rayleigh-Bénard convection. **Physical Review E**, v. 52, p. 4963, nov. 1995. 73

ZHOU, Y.; MATTHAEUS, W. H.; DMITRUK, P. Colloquium: magnetohydrodynamic turbulence and time scales in astrophysical and space plasmas. **Reviews of Modern Physics**, v. 76, p. 1015–1035, dec. 2004. 1, 8

ZUO, P. B.; WEI, F. S.; FENG, X. S.; XU, X. J.; SONG, W. B. Magnetic cloud boundary layer of 9 November 2004 and its associated space weather effects. **Journal of Geophysical Research (Space Physics)**, v. 115, p. A10102, oct. 2010. 5, 89

APENDIX A - DERIVATION OF THE LINEAR DISPERSION RELATION FOR THE PIERCE DIODE

The electron flow in the Pierce diode can be described by the cold fluid equations, namely, continuity, momentum and the Poisson's equations

$$\frac{\partial\rho}{\partial t}+\frac{\partial(\rho v)}{\partial x}=0, \tag{A.1}$$

$$\frac{\partial v}{\partial t}+v\frac{\partial v}{\partial x}=\frac{\partial\phi}{\partial x}, \tag{A.2}$$

$$\frac{\partial^2\phi}{\partial x^2}=\alpha^2(\rho-\rho_0), \tag{A.3}$$

where ρ is the mass density, v is the electron flow velocity and ϕ is the electric potential. The boundary conditons we adopted are $\rho(0,t)=\rho_0$, $v(0,t)=v_0$ and $\phi(0,t)=\phi(1,t)=0$. A linear approximation analysis can be performed on the assumption of solutions of the form $\rho(x,t)=\rho_0+\rho_1(x,t)$ and $v(x,t)=v_0+v_1(x,t)$, with the temporal dependence being $\exp(-i\omega t)$:

$$\rho=\rho_0+\rho_1(x)e^{-i\omega t}, \tag{A.4}$$

$$v=v_0+v_1(x)e^{-i\omega t}. \tag{A.5}$$

Inserting A.4 and A.5 into Eqs. (A.1)–(A.3), and taking just the first order terms, we obtain

$$-i\omega\rho_1+v_0\frac{\partial\rho_1}{\partial x}+\rho_0\frac{\partial v_1}{\partial x}=0, \tag{A.6}$$

$$-i\omega v_1+v_0\frac{\partial v_1}{\partial x}=\frac{\partial\phi}{\partial x}. \tag{A.7}$$

First, we look for the solution of Eq. (A.3) when $\rho_1=0$. In that case $\rho=\rho_0$ and the equation for the electric potential is

$$\frac{\partial^2 \phi}{\partial x^2} = 0, \tag{A.8}$$

which has a linear solution

$$\phi = Ax + D. \tag{A.9}$$

If $\rho_1 = 0$, from Eqs. (A.1) and (A.2) we have

$$\frac{\partial v_1}{\partial x} = 0 \qquad \Rightarrow \qquad -i\omega v_1 = \frac{\partial \phi}{\partial x} = A. \tag{A.10}$$

Now, for the case $\rho_1 \neq 0$, let us suppose a sinusoidal spatial dependence for the perturbations $\rho_1(x) = \tilde{\rho}_1 e^{ikx}$ and $v_1(x) = \tilde{v}_1 e^{ikx}$, and for the electric potential $\phi \sim e^{ikx}$. Substituting into Eqs. (A.4), (A.5) and (A.3) we have

$$-i\omega\tilde{\rho}_1 + ikv_0\tilde{\rho}_1 + ik\rho_0\tilde{v}_1 = 0, \tag{A.11}$$

$$-i\omega\tilde{v}_1 + ikv_0\tilde{v}_1 = ik\phi, \tag{A.12}$$

$$-k^2\phi = \alpha^2\tilde{\rho}_1. \tag{A.13}$$

From Eqs. (A.11) and (A.12) we have

$$(kv_0 - \omega)\tilde{\rho}_1 = -k\rho_0\tilde{v}_1, \tag{A.14}$$

$$\tilde{v}_1 = \frac{k\phi}{kv_0 - \omega}. \tag{A.15}$$

Inserting (A.15) into (A.14)

$$(kv_0 - \omega)\tilde{\rho}_1 = \frac{-k^2\phi\rho_0}{kv_0 - \omega}, \tag{A.16}$$

and using (A.13), finally we obtain

$$(kv_0 - \omega)^2 = \alpha^2\rho_0. \tag{A.17}$$

Recalling that $\rho_0 = 1$ and $v_0 = 1$, the solutions for the wavenumber k are

$$k_1 = \omega + \alpha \qquad k_2 = \omega - \alpha. \tag{A.18}$$

Hence, velocity, density and electric potential have the form

$$v(x,t) = v_0 + (a + be^{ik_1x} + ce^{ik_2x})e^{-i\omega t}, \tag{A.19}$$

$$\rho(x,t) = \rho_0 + (f + ge^{ik_1x} + he^{ik_2x})e^{-i\omega t}, \tag{A.20}$$

$$\phi(x) = Ax + D + Be^{ik_1x} + Ce^{ik_2x} \tag{A.21}$$

Inserting (A.19) into (A.7) we have

$$-i\omega(a+be^{ik_1x}+ce^{ik_2x})+v_0(ik_1be^{ik_1x}+ik_2ce^{ik_2x}) = Ax+ik_1Be^{ik_1x}+ik_2Ce^{ik_2x}. \tag{A.22}$$

Grouping terms, we obtain

$$a = \frac{iA\alpha}{\omega}, \qquad b = \frac{k_1B}{\alpha}, \qquad c = -\frac{k_2C}{\alpha}. \tag{A.23}$$

Imposing the boundary condition $v_1(0) = 0$,

$$iA\alpha + \omega(k_1B - k_2C) = 0. \tag{A.24}$$

In a similar way, replacing (A.20) into (A.6) and gruping terms, we obtain

$$f = 0, \qquad g = -\frac{\rho_0k_1b}{\alpha}, \qquad h = \frac{\rho_0k_2c}{\alpha}. \tag{A.25}$$

Imposing the boundary condition $\rho_1(0) = 0$ and using previously obtained constants, we have

$$C = -\frac{k_1^2}{k_2^2}B. \tag{A.26}$$

Boundary condition $\phi(0) = 0$ implies

$$D = -(B + C). \tag{A.27}$$

Replacing (A.26) in (A.24) gives

$$B = \frac{i\alpha(\omega - \alpha)}{2\omega^2(\omega + \alpha)} A, \tag{A.28}$$

and using this in (A.26) we have

$$C = -\frac{i\alpha(\omega + \alpha)}{2\omega^2(\omega - \alpha)} A, \tag{A.29}$$

Using Eqs. (A.27)–(A.29),

$$D = \frac{i\alpha}{2\omega^2(\omega^2 + \alpha^2)}[(\omega + \alpha)^2 - (\omega - \alpha)^2]A. \tag{A.30}$$

Applying the boundary condition $\phi(1) = 0$, finally we obtain the linear dispersion relation for the Pierce diode

$$2\omega^2(\omega^2 - \alpha^2) + i\alpha\{(\omega + \alpha)^2[e^{i(\omega-\alpha)} - 1] - (\omega - \alpha)^2[e^{i(\omega+\alpha)} - 1]\} = 0. \tag{A.31}$$

PUBLICAÇÕES TÉCNICO-CIENTÍFICAS EDITADAS PELO INPE

Teses e Dissertações (TDI)

Teses e Dissertações apresentadas nos Cursos de Pós-Graduação do INPE.

Notas Técnico-Científicas (NTC)

Incluem resultados preliminares de pesquisa, descrição de equipamentos, descrição e ou documentação de programas de computador, descrição de sistemas e experimentos, apresentação de testes, dados, atlas, e documentação de projetos de engenharia.

Propostas e Relatórios de Projetos (PRP)

São propostas de projetos técnico-científicos e relatórios de acompanhamento de projetos, atividades e convênios.

Publicações Seriadas

São os seriados técnico-científicos: boletins, periódicos, anuários e anais de eventos (simpósios e congressos). Constam destas publicações o Internacional Standard Serial Number (ISSN), que é um código único e definitivo para identificação de títulos de seriados.

Pré-publicações (PRE)

Todos os artigos publicados em periódicos, anais e como capítulos de livros.

Manuais Técnicos (MAN)

São publicações de caráter técnico que incluem normas, procedimentos, instruções e orientações.

Relatórios de Pesquisa (RPQ)

Reportam resultados ou progressos de pesquisas tanto de natureza técnica quanto científica, cujo nível seja compatível com o de uma publicação em periódico nacional ou internacional.

Publicações Didáticas (PUD)

Incluem apostilas, notas de aula e manuais didáticos.

Programas de Computador (PDC)

São a seqüência de instruções ou códigos, expressos em uma linguagem de programação compilada ou interpretada, a ser executada por um computador para alcançar um determinado objetivo. Aceitam-se tanto programas fonte quanto os executáveis.